Performance of Space-Time MIMO Systems Employing Uniform Circular Array Using Realistic Channel Models

by

Zahra Mahdi Abdulla

A Thesis Submitted in Partial Fulfillment of the
Requirements for the Degree of

Master of Science
in
Electronics Engineering

Department of Electrical and Electronics Engineering
University of Bahrain
Bahrain

Supervised by

Dr. Mohab A. Mangoud

Department of Electrical and Electronics Engineering
University of Bahrain
Bahrain

2012

DECLARATION

I declare that this work is the result of my own investigation and that it has not already been accepted in substance of any degree, nor is it being currently submitted for any degree.

Signed:.....Zahra..... Date: 06/11/2012

The thesis defense committee considers the Thesis titled:

"Performance of Space-Time MIMO Systems Employing Uniform Circular Array Using Realistic Channel Models"

Submitted by Zahra Mahdi Abdulla to the Department of Electrical and Electronics Engineering satisfactory and acceptable for the Master of Science degree in Electronics Engineering.

Thesis Defense Committee:

Prof. Salam Adel Zummo

Dr. Sana Al-Mansoori

Dr. Mohab Mangoud

Acknowledgements

I would like to express my thanks to Allah Subhana Wa Ta'ala for providing me the means to complete this thesis. Next, I would like to thank my advisor Dr. Mohab Mangoud for his guidance, encouragement and support through my master's research. In addition, I am grateful to Dr. Sameer Al Ghadban for his assist in providing V-BLAST program that is partially used in Chapter 4. I also would like to thank all the faculty and staff members in the Electrical and Electronics department for their encouragement and valuable advice. I am also very grateful to my family for their love, patience, moral support and continuous encouragement.

Performance of Space-Time MIMO Systems Employing Uniform Circular Array Using Realistic Channel Models

Zahra Mahdi

(ABSTRACT)

Recently, Multiple Input Multiple Output (MIMO) technology has been widely used to improve the transmission signal quality, coverage and channel capacity for modern wireless communications systems. The performance of MIMO systems that utilize multiple transmit and multiple receive antennas, is directly dependent on the correlation properties of the radio propagation channel. The correlation properties depend on the antenna configuration, Doppler spread and the distribution of scattering objects between the transmitter and receiver. Therefore, the main scope of this thesis is to develop and analyze a realistic channel model that includes accurate signal fading correlation properties. The capacity and system performance of wireless LAN systems are investigated under the developed realistic channel model. Also, the objective is to study the performance of the latest Wi-Fi IEEE 802.11*n* emerging standard and recommend the best environment for applying this technology.

The Thesis starts with a thorough survey on the different existing MIMO channel models. Physical, analytical and standard model classifications are presented. Comparisons that highlight the theoretical differences and limitations for each model are provided. In this Thesis, a stochastic spatial clustered (SSC) channel model is presented. This is followed by a more realistic spatial and temporal clustered (STC) channel model. This realistic model involves treating reflection paths as clusters of rays. Each cluster has a power at different delays that is related to different tap coefficients in discrete time. The model accounts for six various real propagation scenarios that represent a variety of indoor environments.

The STC channel model is developed to modify the existing IEEE 802.11*n* standard model to consider uniform circular array (UCA) for MIMO systems. The impact of channel model selection on link performance of systems is investigated for uniform linear array (ULA) and UCA configurations. The study includes also the effect of varying the elements spacing of

array geometries and their orientations at both ends. The information-theoretic channel capacity of correlated channels is studied when channel state information (CSI) is known at the transmitter. The effect of line of sight (LOS) existence is also demonstrated.

Also, the performance analysis of Vertical Bell Laboratories Space-Time (V-BLAST) system is investigated including the effect of fading correlation. Simulations of MIMO systems are developed employing the SSC channel model for both ULA and UCA geometries at the receiver. Different receiver detection techniques are implemented that include linear zero forcing (ZF), linear minimum mean square error (MMSE), successive interference cancellation (SIC), parallel interference cancellation (PIC) and maximum likelihood (ML). Spatial fading correlation effects on the system performance are investigated utilizing the SSC channel model for various signal to noise ratio (SNR), angle of arrival (AOA), angular spread (AS), inter-element spacing distance between array elements. Moreover, the impact of different channel conditions to the detection performance is presented using the developed STC channel model.

Finally, to fully analyze the MIMO system performance, precise channel state information is required at the receiver. A number of training-based channel estimation methods are studied including least squares (LS), scaled least squares (SLS), linear minimum mean square error (LMMSE), and relaxed minimum mean square error (RMMSE). The optimal training sequences are driven numerically and are utilized in the numerical simulations. In this Thesis, the different channel estimation methods are implemented in the MIMO system simulation that utilizes the SSC channel model. The impact of channel spatial correlation on the channel estimation error is evaluated for both ULA and UCA antenna. It is confirmed that the presence of spatial correlation can help to achieve a better quality CSI at low SNR. The performances of channel estimators are investigated when applying optimum and orthogonal training sequences. Also, channel estimation errors and capacity for ULA and UCA MIMO systems are compared under various AOA and AS values.

Table of Contents

Notation ..... **xii**

1. Introduction **1**

1.1 MIMO Wireless Communications Technology 1

1.2 Overview of Research 2

1.3 Contributions of This Work 4

1.4 Outline of Thesis 4

2. Survey of Channel Models and Capacity Investigations for Wireless MIMO Systems. 6

2.1 The Basic Multipath Propagation Mechanisms 7

2.2 Types of MIMO Channel 9

2.2.1 Narrowband MIMO Channel 10

2.2.2 Wideband MIMO Channel 10

2.3 MIMO Channel Model Classification 11

2.3.1 Physical Models 12

2.3.1.1 Deterministic Physical Models 12

2.3.1.2 Geometry-Based Stochastic Physical Channel Model 12

i. One-Ring Model 12

ii. Two-Ring Model 13

iii. Von Mises Angular Distribution 14

2.3.1.3 Non-Geometrical Stochastic Physical Channel Models 15

i. Extended Saleh-Valenzuela Model 15

ii. Zwick Model 18

2.3.2 Analytical Models 18

2.3.2.1 Correlation-Based Analytical Models 18

i. i.i.d. Rayleigh Channel Model 19

ii. Kronecker Model 20

iii. Weichselberger Model 21

iv. Structured Model 22

2.3.2.2 Propagation-based analytical models 22
i. Finite Scatterers Model 22
ii. Maximum Entropy Model 23
iii. Virtual Channel Representation 24
iv. Distributed Scatterers Model 25
2.3.3 Standardized Models 26
i. 3GPP Spatial Channel Model 26
ii. IEEE 802.11*n* Channel Model 26
iii. METRA 27
iv. COST 259/273 Channel Models 27
v. SUI Models and IEEE 802.16 28
2.4 Stochastic Spatial Clustered Channel Model 30
2.4.1 Numerical Results 36
2.5 MIMO Channel Capacity 41
2.5.1 Uniform Power Allocation Scheme 42
2.5.2 Water-Pouring Power Allocation Scheme 43
2.5.3 Ergodic Capacity 47
2.6 Conclusion 51

3. Spatial-Temporal Realistic Clustered Channel Model for Circular Array Based WLAN MIMO Systems 52

3.1 IEEE 802.11*n* TG*n* Channel Models 53
3.2 Spatial-Temporal Clustered Channel Model 54
3.2.1 Rice Steering Matrix 56
3.2.2 Antenna Correlation Modelling 57
3.2.3 Temporal Doppler Component 58
3.3 Numerical Results and Analysis 60
3.4 Conclusion 71

4. Effects of Fading Correlation on the Performance of Spatial Multiplexing MIMO Systems 72

4.1 V-BLAST Architecture 73
4.2 MIMO Detection Techniques 74
4.2.1 Linear Signal Detection 74

4.2.1.1 Zero Forcing Signal Detection 74
4.2.1.2 Minimum Mean Square Error Signal Detection 75
4.2.2 Successive Interference Cancellation Signal Detection 76
4.2.3 Parallel Interference Cancellation Signal Detection 78
4.2.4 Maximum Likelihood Signal Detection 79
4.3 Numerical Results 80
4.4 Conclusion 89

5. Effects of Spatial Correlation on the MIMO Channel Estimation Error 90

5.1 Training-Based Channel Estimation Methods 91
5.1.1 Least Squares Channel Estimator 91
5.1.2 Scaled Least Squares Channel Estimator 93
5.1.3 Linear Minimum Mean-Square Error Channel Estimator 94
5.1.4 Relaxed Minimum Mean-Square Error Channel Estimator 96
5.2 Numerical Results 98
5.3 Conclusion 107

6. Conclusion and Future Work 108

6.1 Conclusions 108
6.2 Future Work 112
6.3 Publication List 113

A. IEEE 802.11*n* Channel Models 115

B. Numerical Examples of Ordered SIC and PIC Detection Techniques 123

8.1 Ordered SIC 123
8.2 PIC 126

Bibliography 128

List of Figures

2.1 Wireless propagation in an indoor environment 7
2.2 Illustration of a MIMO system. 9
2.3 Classification of MIMO channel and propagation models 11
2.4 Illustration of the one-ring model. 13
2.5 Illustration of the two-ring model 14
2.6 Illustration of the one-ring model using Mises angular distribution. 14
2.7 Cluster Structure in the Saleh-Valenzuela model. 16
2.8 Concept of the finite scatterers channel model, illustrating (a) typical single scattererd path, (b) reflected path, and (c) split component. 23
2.9 Illustration of the distributed scattering model. 25
2.10 Wireless communication system employing ULA array 30
2.11 Wireless communication system employing UCA array. 31
2.12 Comparisons for the three PAS distributions ($\theta = 0^{o}$, $\sigma = 20^{o}$). 33
2.13 MIMO communication system employing ULA/UCA configurations. 37
2.14 Spatial correlation (Rs) versus antenna spacing for ULA configuration at $\theta_r = 45^{o}$ and $\sigma = 20^{o}$ 39
2.15 Spatial correlation (Rs) versus antenna spacing for UCA configuration at $\theta_r = 45^{o}$ and $\sigma = 20^{o}$ 39
2.16 Spatial correlation of ULA and UCA configurations vs. AS (σ) for different AOA, $\theta_r = \{0^{o}, 45^{o}, 90^{o}\}$, $D_r = 0.5\lambda$, and $R_r = 0.75\lambda$. 40
2.17 Spatial correlation of ULA and UCA configurations vs. AOA (θ_r) for different AS, $\sigma = \{3^{o}, 7^{o}, 20^{o}\}$, $D_r = 0.5\lambda$, and $R_r = 0.75\lambda$. 40
2.18 Schematic of model decomposition of **H** when the channel is known to the transmitter and receiver 43
2.19 The r virtual SISO channels obtained from the model decomposition 44
2.20 Schematic of water-pouring power allocation algorithm. 46
2.21 CDF information rate for $\mathbf{H}_{iid}$ MIMO channel with $M_t = M_r = 2$ and SNR= 10dB. 47
2.22 Ergodic capacity for different antenna elements versus SNR. 48

2.23 Comparison of ergodic capacity of $M_t = M_r = 4$ MIMO channel with uniform and water-pouring power allocation schemes. 50
2.24 Comparison of ergodic capacity for different number of transmit M_t and receive M_r antennas with uniform and water-pouring power allocation schemes at SNR = 10 dB.. 50
3.1 MIMO communication system employing $(M_r \times M_t)$ ULA/UCA configurations. 55
3.2 An overview of TD-FWGN model. 59
3.3 "Bell" shape Doppler power spectrum at f_c =2.4 GHz. 60
3.4 PDF of the AOA for the taps of model 'F'. 62
3.5 Rs(21,11) for various taps of model 'F' versus UCA radius in the receiver. 62
3.6 Doppler Spectrum in the bell-shape at f_c =5.25 GHz. 63
3.7 Capacity versus radius for the TG*n* channel models for 4x4 UCA-MIMO and SNR=10 dB. 63
3.8 Channel singular values CDFs of models 'A', 'B' and 'F' for 4x4 UCA-MIMO. 65
3.9 Capacity versus azimuth orientation angle at the receiver side for ULA and UCA configurations and SNR=10 dB. 65
3.10 Capacity versus radius of models 'A', 'B' and 'F' for $M_t = 4$ and $M_r = 2,4,8$. 66
3.11 CDFs of capacity for models 'A', 'B' and 'F' for 4x4 UCA-MIMO with LOS and NLOS conditions at SNR= 10 dB. 68
3.12 Ergodic capacities of channels 'A', 'B', and 'F' versus SNR, for 4x4 UCA based system with uniform and water-pouring power allocation schemes. 68
3.13 Comparisons of channel capacity for four antenna configurations, for models 'A', 'B' and 'C'. 69
3.14 Comparisons of channel capacity for four antenna configurations, for models 'D', 'E' and 'F'. 70
4.1 Block diagram of V-BLAST architecture. 73
4.2 Ordered SIC signal detection diagram. 78
4.3 PIC signal detection diagram. 79
4.4 BER performance of SIC detector versus SNR with uncorrelated channel. 82
4.5 BER performance of PIC detector versus SNR with uncorrelated channel. 82
4.6 Comparison between the performance of SIC and PIC detectors with uncorrelated channel. 83
4.7 Performance of OSIC-MMSE with uncorrelated channel for $M_t = 2$ and $M_r = \{2,3,4\}$ 83

4.8 BER performance of OSIC-MMSE detector for ULA and UCA receiver as a function of central AOA (θ_r) at various SNR, SNR= {0, 10, 20} dB, and σ =20°. 85

4.9 BER performance of OSIC-MMSE detector for ULA and UCA receiver as a function of central AOA (θ_r) at various AS, σ = {1°, 5°, 20°}, and SNR= 20 dB. 85

4.10 BER performance of OSIC-MMSE detector for ULA and UCA receiver versus angular spread (σ) at different AOA, θ_r = {0°, 45°, 90°}, and SNR= 20dB. 86

4.11 BER performance of OSIC-MMSE detector for ULA and UCA receiver versus receiver antenna spacing for different AOA, θ_r = {0°, 45°, 90°}, σ =20°, and SNR= 20dB. 88

4.12 BER performance of OSIC-MMSE detector for models 'A', 'C' and 'F' at various receiver radii (R_r=0.5λ and R_r=0.75λ). 88

5.1 Channel estimation MSEs of LS, LS-SLS, and SLS versus SNR in uncorrelated environment for M_r = 4 and M_t = 2,4. 98

5.2 Channel estimation MSEs of LMMSE estimator in uncorrelated environment versus SNR with orthogonal and optimal sequences for M_r = 4 and M_t = 2,4. 100

5.3 Channel estimation MSEs of the LS, SLS, LMMSE, and RMMSE estimators in uncorrelated environment versus SNR with orthogonal training sequence. 100

5.4 Channel estimation MSEs of the LMMS as a function of AOA at various SNR, for orthogonal training sequence at σ = 20°. 102

5.5 Channel estimation MSEs of the SLS as a function of AOA at various SNR, for orthogonal training sequence at σ = 20°. 102

5.6 Normalized MSE of LMMSE channel estimator versus AOA vs. AS at SNR =10 dB, in case of ULA-MIMO receiver. 103

5.7 Normalized MSE of LMMSE channel estimator versus AOA vs. AS at SNR =10dB, in case of UCA-MIMO receiver. 103

5.8 Normalized MSE of the LMMSE channel estimator with optimal training for ULA-MIMO receiver at θ_r = 90°, SNR=10 dB and σ = 20°. 105

5.9 Normalized MSE of the LMMSE channel estimator with optimal training for UCA-MIMO receiver at θ_r = 90°, SNR=10 dB and σ = 20°. 105

5.10 Capacity of UCA-MIMO channel with LMMSE estimator versus SNR at θ_r=90° and different AS. 106

5.11 Normalized MSE of LMMSE estimator versus SNR for UCA-MIMO receiver at θ_r=90° and different AS. 106

Notation

Abbreviations and mathematical operators used in this thesis are listed below.

Abbreviations

3GPP	3th Generation Partnership Project
AOA	Angle of Arrival
AOD	Angle of Departure
AP	Access Point
AS	Angular Spread
BER	Bit Error Rate
BLAST	Bell-Labs Layered Space Time
BPSK	Binary Phase Shift Keying
BS	Base Station
CDF	Cumulative Density Function
CSI	Channel State Information
D-BLAST	Diagonal-BLAST
DFT	Discrete Fourier Transform
EVD	Eigen Value Decomposition
GSCM	Geometry-Based Stochastic Channel Model
LMMSE	Linear Minimum Mean Square Error
LOS	Line of Sight
LS	Least Squares
LST	Layered Space-Time
MIMO	Multiple-Input Multiple-Output
ML	Maximum Likelihood
MISO	Multiple-Input Single-Output
MMSE	Minimum Mean Square Error

MS	Mobile Station
MSE	Mean Square Error
MT	Mobile Terminal
NLOS	Non Line of Sight
PAS	Power Azimuth Spectrum
PDF	Probability Density Function
PDP	Power Delay Profile
PIC	Parallel Interference Cancellation
QPSK	Qadrature Phase Shift Keying
RMMSE	Relaxed MMSE
SIC	Successive Interference Cancellation
SIMO	Single-Input Multiple-Output
SISO	Single-Input Single-Output
SLS	Scaled Least Squares
SSC	Stochastic Spatial Clustered
STA	Wireless station
STBC	Space-Time Block Codes
STC	Spatial-Temporal Clustered
STTC	Space-Time Trellis Code
SVD	Singular Value Decomposition
TD-FWGN	Time-Domain Filtered White Gaussian Noise
TGn	Task Group n
UCA	Uniform Circular Array
ULA	Uniform Linear Array
V-BLAST	Vertical-BLAST
WLAN	Wireless Local Area Network
ZF	Zero Forcing
ZMCSCG	Zero-Mean Circular Symmetric Complex Gaussian

Mathematical Operators

$\dagger$	Moore-Penrose Pseudo-inverse operation
$[\cdot]^H$	Hermitian transpose operation
$[\cdot]^*$	Complex conjugate operation
$[\cdot]^T$	Matrix/vector transpose
$\|\|\cdot\|\|_F^2$	Frobenuis matrix norm
$\mathrm{Tr}\{\cdot\}$	Trace of a matrix
$E[\cdot]$	Expectation operator
$I_o[\cdot]$	Zero order Bessel function of the first kind
$\odot$	Hadamard multiplication
$\otimes$	Kronecker product
$\det(\cdot)$	Determinant Operation

Chapter 1

Introduction

Wireless communications system designers are faced with a number of challenges. These include the limited availability of the radio frequency spectrum and the complex time-varying wireless environment, the latter leads to attenuation in the signal amplitude due to multipath fading. In addition, meeting the increasing demand for high data rate and better quality of service, driven by cellular mobile, Internet and multimedia services is an incentive for the designers to seek innovative techniques that improve the spectral efficiency and link reliability. As a solution to these challenges, diversity techniques are widely used [1] [2] [3]. There are three types of diversity schemes in wireless communications, namely: *temporal*, *frequency*, and *spatial.* These techniques provide multiple replicas of the transmitted signal over *time*, *frequency*, or *space*, respectively at the receiver, all carrying the same information but with a small fading correlation.

1.1 MIMO Wireless Communications Technology

Multiple-input multiple output (MIMO) antenna systems are forms of space and time diversity. These systems are realized using multiple antennas at both the transmitter and receiver to improve communication performance. The MIMO systems can be implemented in a number of different ways to obtain either a diversity gain to combat signal fading or to obtain capacity improvement. In the literature, there are three categories of MIMO techniques. The first one aims to improve the power efficiency that maximizes the spatial diversity by sending and receiving *redundant* streams of information in parallel along the different spatial paths between transmit and receive antennas. Such techniques include space-

time block codes (STBC) [4] and space-time trellis code (STTC) [5]. The second type uses spatial multiplexing, where *independent* data streams are simultaneously transmitted over different antennas to increase the data rate. The layered space-time (LST) architecture that was proposed by Foschini in [6] is an example of this technique. The third type utilizes knowledge of channel at the transmitter, known as beamforming. It exploits the information to build the beamforming matrices as pre-and post filters at the transmitter and receiver to achieve capacity gain.

1.2 Overview of Research

For wireless communication systems, the wireless channel is the key factor that determines system performance. Channel effects, such as path loss and multipath fading, result in the attenuation of the signal amplitude at the receiver. Spatial diversity and spatial multiplexing can significantly improve performance and overcome the undesired effects of multipath but only when the channels between each transmit-receive antenna pair fade independently (uncorrelated channel). As an example, in [7] it has been shown that in the condition of ideal propagation (uncorrelated channel), the MIMO channel has the potential to provide capacity of n times that of a single-input single-output (SISO) system without increase in the transmit power and bandwidth (n represents the minimum of the number of receive or transmit antenna elements). The capacity is expressed by the maximum achievable data rate for an arbitrarily low probability of error. However, in real propagation environments, this assumption is not accurate due to the physical limitation of antenna configuration, i.e., the insufficient spacing between antenna elements. In [8] it has been shown that in case of a correlated channel, the channel capacity can be significantly lower than that of an uncorrelated channel. The correlation depends on the antenna configuration, Doppler spread, the distance between the transmitter and receiver, and distribution of scattering objects that are present in the path between the transmitter and receiver. Therefore, developing accurate and realistic correlated channels model is essential and of crucial importance to evaluate the proper performance of real MIMO systems. The channel modelling is one of the most significant challenges in designing wireless communications system because of the time-varying nature of the channel. In addition, it is important to characterize and model the MIMO channel for different propagation conditions so as to predict and design high performance communications system. Therefore, the main objective of this research is to develop a realistic propagation channel

model that can fully characterize the correlation properties. In addition, the aim is to analytically investigate the effects of fading correlation on MIMO systems.

In this thesis, two channel models are utilized. The first channel model is the stochastic spatial clustered (SSC) channel model. This model is based on the mathematical spatial model developed in [9] [10]. In this model, the groups of scatterers are modelled as multi-clusters located around the antenna arrays. The spatial fading correlation can be determined from the physical parameters of the model, which include antenna spacing, antenna arrangement, angular spread (AS), Power Azimuth Spectrum (PAS), and the central angle of incidence of the waves. Three different PAS were assumed with uniform, truncated Gaussian and truncated Laplacian. This model is realized for both uniform linear array (ULA) and uniform circular array (UCA) antennas. The spatial correlation properties of a MIMO system is modelled as the Kronecker product of the spatial correlation matrices defined independently at the transmitter and at the receiver. The second model is a more realistic spatial and temporal clustered (STC) channel model that is based on the WLAN IEEE 802.11*n* standard [11]. This realistic model involves treating reflection paths as clusters of rays. Each cluster has a power at different delays that is related to different tap coefficients in discrete time. The model accounts for six various real propagation scenarios that represent a variety of indoor environments. The existing IEEE 802.11*n* employs ULA antennas. In this research, the STC channel model has been developed to include the UCA antennas in order to investigate the channel capacity performance of IEEE 802.11*n* in different propagation conditions.

Also, the performance analysis of spatial multiplexing MIMO system is investigated including the effect of fading correlation. Simulations of MIMO systems are developed employing the SSC channel model for both ULA and UCA antennas. Different receiver detection techniques are implemented that include linear zero forcing (ZF), linear minimum mean square error (MMSE), successive interference cancellation (SIC), parallel interference cancellation (PIC) and maximum likelihood (ML).

Most MIMO systems are based on perfect channel knowledge being available at the receiver. However, perfect channel knowledge is never known a *priori*. In practice, the channel has to be estimated. Therefore, accurate channel state information (CSI) is required at the receiver. The availability of accuracy CSI is needed to decode the received signal and to practically reach the MIMO capacity. Obtaining accurate CSI can be accomplished using suitable

channel estimation methods. The most popular techniques are based on training sequences, known as training-based channel estimation methods. The channel can be estimated based on the received data and the knowledge of training symbols. In [12], several training-based methods including the least squares (LS), scaled LS (SLS), linear minimum mean square error (LMMSE), and relaxed MMSE (RMMSE) have been investigated. In this Thesis, the training-based methods are implemented in the MIMO system simulation utilizing the SSC channel model. The impact of channel spatial correlation on the channel estimation error is investigated for both ULA and UCA antennas in different propagation conditions. In addition, the MIMO channel capacity is evaluated considering the channel estimation error.

1.3 Contributions of This Work

The main contributions of this thesis are as follows:

- The existing IEEE 802.11*n* standard channel model is modified to consider the UCA antennas. The channel capacity of WLAN is investigated for ULA and UCA antennas in different propagation environments.
- The impact of spatial correlation on the performance analysis of spatial multiplexing MIMO systems is investigated utilizing the SSC channel model for both ULA and UCA antennas.
- The correlation effects on the accuracy of LMMSE and SLS channel estimators are investigated utilizing the SSC channel model for both ULA and UCA antennas.

1.4 Outline of Thesis

This thesis is organized as follows:

In **Chapter 1**, introduction, objectives and contributions of the thesis are presented.

In **Chapter 2**, firstly, the characterization of the wireless propagation environment is presented. Secondly, a survey on the most important developments in the area of MIMO channel modelling is provided along with comparisons that highlight the differences and limitations for each model. The MIMO channel models are classified into *physical* and *analytical models*. In addition, MIMO models developed within wireless standard are also presented. Then, the stochastic spatial clustered (SSC) channel model is presented. An analytical expression for the spatial fading correlation function for MIMO channels is

introduced for both ULA and UCA antennas. The spatial fading correlation function is a function of angular spread, angle of incidence, PAS distribution and distance between elements that are dependent on the array geometry. Comparative results on the spatial fading correlation for both the ULA and UCA are presented. Finally, the information-theoretic channel capacity is demonstrated with two different power allocation techniques, *uniform* and *water-pouring* according to the availability of the CSI to the transmitter. Numerical results are carried out to evaluate the MIMO channel capacity.

In **Chapter 3**, a realistic spatial and temporal clustered (STC) channel model is developed to be applied in the simulation of UCA-MIMO WLAN system applying IEEE 802.11*n* standard. The proposed model accounts for six (A-F) different real propagation environments that are applied in IEEE 802.11*n* TG*n* channel model. Firstly, the TG*n* channel models are presented. Secondly, the modifications to the existing IEEE 802.11*n* channel models to employ UCA configuration are addressed. Finally, numerical results are presented to investigate the channel capacity under various realistic scenarios for both the ULA and UCA.

In **Chapter 4**, the signal detection techniques for spatial multiplexing MIMO systems including linear signal detection, successive interference cancellation (SIC), parallel interference cancellation (PIC) and maximum likelihood (ML) are presented. In addition, the effects of spatial fading correlation on the performance analysis applying the SSC channel mode are investigated under different channel propagation conditions for both the ULA and UCA geometries.

In **Chapter 5**, a number of training-based MIMO channel estimation methods are studied including the LS, SLS, LMMSE and RMMSE. The optimal choices of training matrices for the LS, SLS and LMMSE are presented. The performance of these channel estimators is investigated and compared. Furthermore, the influences of the spatial fading correlation on the accuracy of the SLS and LMMSE under various channel propagation conditions are investigated for the ULA and UCA. Moreover, the channel capacity is evaluated with considering the channel estimation error for the above training-based techniques.

Finally in **Chapter 6**, a summary of the results is presented and some suggestions and recommendations for future work are provided. In addition, the publications of this thesis are presented.

Chapter 2

Survey of Channel Models and Capacity Investigations for Wireless MIMO Systems

The increasing demand for high data rates and the limited available bandwidth motivates the investigation of wireless systems that efficiently utilize the spatial domain. As reported in [13], the capacity of a MIMO system can be significantly increased under the assumption that individual paths in the MIMO channel are *independent.* However, over many experimental studies [14], it was found that, in many practical cases, this assumption was not accurate. Experimental data have shown that, depending on the environment, the capacity of a measured channel often falls short of the limit given by Foschini [7]. Given that, the propagation conditions determine the channel capacity, it is of great interest to characterize and model the MIMO channel for different conditions in order to predict, and design high performance communications system. This chapter provides a survey of the most important developments in the area of MIMO channel modelling. The MIMO channel capacity is demonstrated and the spatial fading correlation function is introduced for MIMO channels. This chapter is organized as follows: Section 2.1 presents the basic multipath propagation mechanisms. Section 2.2 demonstrates the types of MIMO channels. Section 2.3 provides an overview of MIMO channel models classification. Section 2.4 presents the stochastic spatial clustered (SSC) channel model for different antenna geometries. Also, in this section the comparative results on the fading correlation for both the ULA and UCA geometries are presented. Section 2.5 demonstrates the information-theoretic channel capacity of the MIMO

channel exploiting the uniform and water-pouring power allocation schemes. Finally, Section 2.6 concludes the chapter and summarizes the key findings.

2.1 The Basic Multipath Propagation Mechanisms

The performance of wireless communication systems is mainly governed by the wireless channel environment. Unlike wired channels that are stationary and predictable, radio channels are extremely random. Radio waves propagate through a physical medium interacting with physical objects and structures such as buildings, hills, trees, etc. This process can result in a single line-of-sight (LOS) propagation path, non-LOS (NLOS) reflected propagation paths, or a combination of LOS and NLOS propagation paths (multipath environment). The multipath propagation is mainly affected by three different modes of physical phenomenon: reflection, diffraction, and scattering [15]. As an example, an illustration of wireless propagation in an indoor environment is shown in Fig. 2.1.

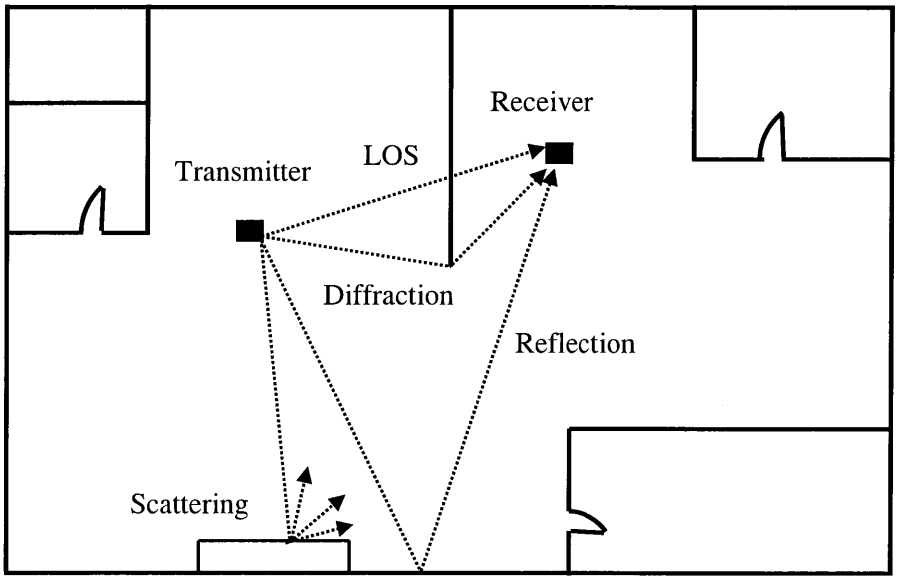


Fig. 2.1 Wireless propagation in an indoor environment.

Reflection: is the physical phenomenon that occurs when a propagation electromagnetic wave impinges upon an object with very large dimensions compared to the wavelength, e.g., surface of the earth and buildings.

Diffraction: is the physical phenomenon that occurs when the radio path between the transmitter and receiver is obstructed by a surface with sharp irregularities or small openings.

Scattering: is the physical phenomenon that forces radiation of an electromagnetic wave to deviate from a straight path by one or more local obstacles, with small dimensions compared to the wavelength, such as foliage, street signs, and lamp posts.

A unique characteristic in a wireless channel is a phenomenon called 'fading,' the variation of the signal amplitude over time and frequency. The fading phenomenon can be classified into two different types: *large-scale fading* and *small-scale fading*. Large-scale fading represents the average power attenuation or the path loss due to motion over large areas. This phenomenon is affected by prominent terrain contours (e.g. hills, forests, billboards, clumps of buildings, etc) between the transmitter and receiver. Small-scale fading refers to the dramatic changes in signal amplitude and phase as a result of small changes (as small as half wave length) in the spatial positioning between a receiver and transmitter. Depending on the relative extent of a multipath, frequency selectivity of a channel is characterized (e.g., by frequency-selective or frequency flat). Meanwhile, depending on the time variation in a channel due to mobile speed (characterized by the Doppler spread), short-term fading can be classified as either fast fading or slow fading [16]**.** Small-scale fading is known as Rayleigh fading when there are multiple reflective paths and no LOS component otherwise it is called Ricean. In case of Rayleigh fading the probability density function (PDF) of the signal's envelope r is given by [15]

$$p(r) = \frac{r}{\sigma^2} e^{-\frac{r^2}{2\sigma^2}}, \quad r \geq 0 \tag{2.1}$$

where $E[r^2] = 2\sigma^2$ is the distance- average power of the received signal and the notation $E[\cdot]$ denotes the expectation operation. While, in case of Ricean fading the PDF according to [15] is given by

$$p(r) = \frac{r}{\sigma^2} e^{-\frac{r^2+A^2}{2\sigma^2}} I_0\left(\frac{Ar}{\sigma^2}\right), \quad r \geq 0, A \geq 0 \tag{2.2}$$

with A being the peak amplitude of the LOS signal and $I_0(\cdot)$ is the modified Bessel function of first kind and zero order. The Ricean K-factor controls the ratio of powers of the free space signal and the scattered waves, i.e. $K = \frac{A^2}{2\sigma^2}$; when $K = 0$ the Ricean fading degenerates to Rayleigh fading and when K extends to infinity ($K \to \infty$) it degenerates to Gaussian fading.

2.2 Types of MIMO Channel

Fig. 2.2 shows a MIMO system with M_t transmit antennas and M_r receive antennas.

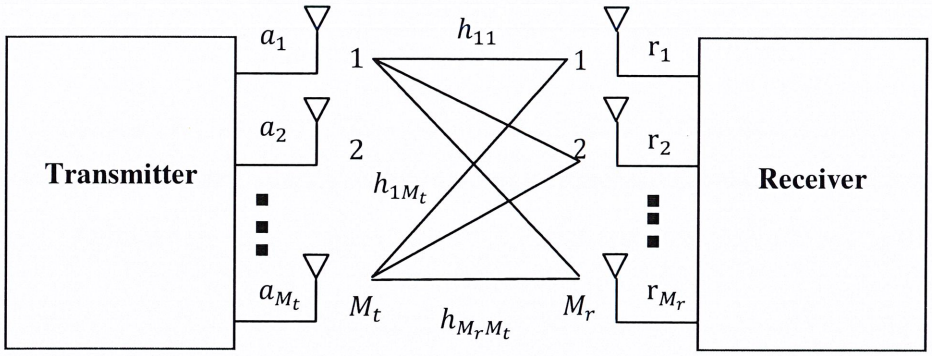


Fig. 2.2 Illustration of a MIMO system.

The baseband input-output relationship over a symbol period can be expressed as [1]

$$\mathbf{r}(t) = \sqrt{\frac{E_a}{M_t}} \int_{\tau} \mathbf{H}(t,\tau)\, \boldsymbol{a}(t-\tau)\mathrm{d}\tau + \mathbf{n}(t) \tag{2.3}$$

where E_a is the total average energy available at the transmitter over a symbol period, $\boldsymbol{a}(t) \in \mathbb{C}^{M_t \times 1}$ is the transmitted signal vector, $\mathbf{r}(t) \in \mathbb{C}^{M_r \times 1}$ is the received signal vector, $\mathbf{n}(t) \in \mathbb{C}^{M_r \times 1}$ is additive white Gaussian noise (AWGN) and $\mathbf{H}(t,\tau) \in \mathbb{C}^{M_r \times M_t}$ is the linear time-variant MIMO channel matrix which can be represented as

$$\mathbf{H}(t,\tau) = \begin{bmatrix} h_{11}(t,\tau) & h_{12}(t,\tau) & \cdots & h_{1M_t}(t,\tau) \\ h_{21}(t,\tau) & h_{22}(t,\tau) & \cdots & h_{2M_t}(t,\tau) \\ \vdots & \vdots & \ddots & \vdots \\ h_{M_r1}(t,\tau) & h_{M_r1}(t,\tau) & \cdots & h_{M_rM_t}(t,\tau) \end{bmatrix} \tag{2.4}$$

where $h_{ij}(t,\tau)$ denotes the time-variant impulse response between the *j*th transmit antenna and the *i*th receive antenna. If the channel is time-invariant, the dependence of the channel matrix on t vanishes ($\mathbf{H}(t,\tau) = \mathbf{H}(\tau)$) and can be further classified into *narrowband* and *wideband* channel [17].

2.2.1 Narrowband MIMO Channel

In the narrowband channel the wireless channel bandwidth is wider than that of the signal bandwidth, so that the channel can be treated as approximately constant over frequency (frequency flat channel). The corresponding input-output relationship simplifies to

$$\mathbf{r}(t) = \sqrt{\frac{E_a}{M_t}}\mathbf{H}\boldsymbol{a}(t) + \mathbf{n}(t) \tag{2.5}$$

where **H** is the narrowband MIMO channel matrix that given as

$$\mathbf{H} = \begin{bmatrix} h_{11} & h_{12} & \cdots & h_{1M_t} \\ h_{21} & h_{22} & \cdots & h_{2M_t} \\ \vdots & \vdots & \ddots & \vdots \\ h_{M_r1} & h_{M_r1} & \cdots & h_{M_rM_t} \end{bmatrix} \tag{2.6}$$

2.2.2 Wideband MIMO Channel

In the wideband channel the channel bandwidth is narrower than that of the signal bandwidth such that the transmit signal may be filtered out by the finite channel bandwidth (frequency selective channel). The input-output relationship can be written as [1]

$$\mathbf{r}[i] = \sqrt{\frac{E_a}{M_t}}\sum_{\tau=1}^{L}\mathbf{H}[\tau]\boldsymbol{a}\,[i-(\tau-1)] + \mathbf{n}[i] \tag{2.7}$$

In this case, the MIMO channel is expressed using discrete rather than continuous variables as

$$\mathbf{H}[\tau] = \begin{bmatrix} h_{11}[\tau] & h_{12}[\tau] & \cdots & h_{1M_t}[\tau] \\ h_{21}[\tau] & h_{22}[\tau] & \cdots & h_{2M_t}[\tau] \\ \vdots & \vdots & \ddots & \vdots \\ h_{M_r1}[\tau] & h_{M_r1}[\tau] & \cdots & h_{M_rM_t}[\tau] \end{bmatrix} \tag{2.8}$$

where $h_{ij}[\tau]$ describes the complex gain between the *j*th transmit antenna and the *i*th receive antenna, at delay τ.

2.3 MIMO Channel Model Classification

The MIMO channel models are classified into *physical* and *analytical* models. An overview of this classification is shown in Fig. 2.3, which is a modified version of the classification presented in [18].

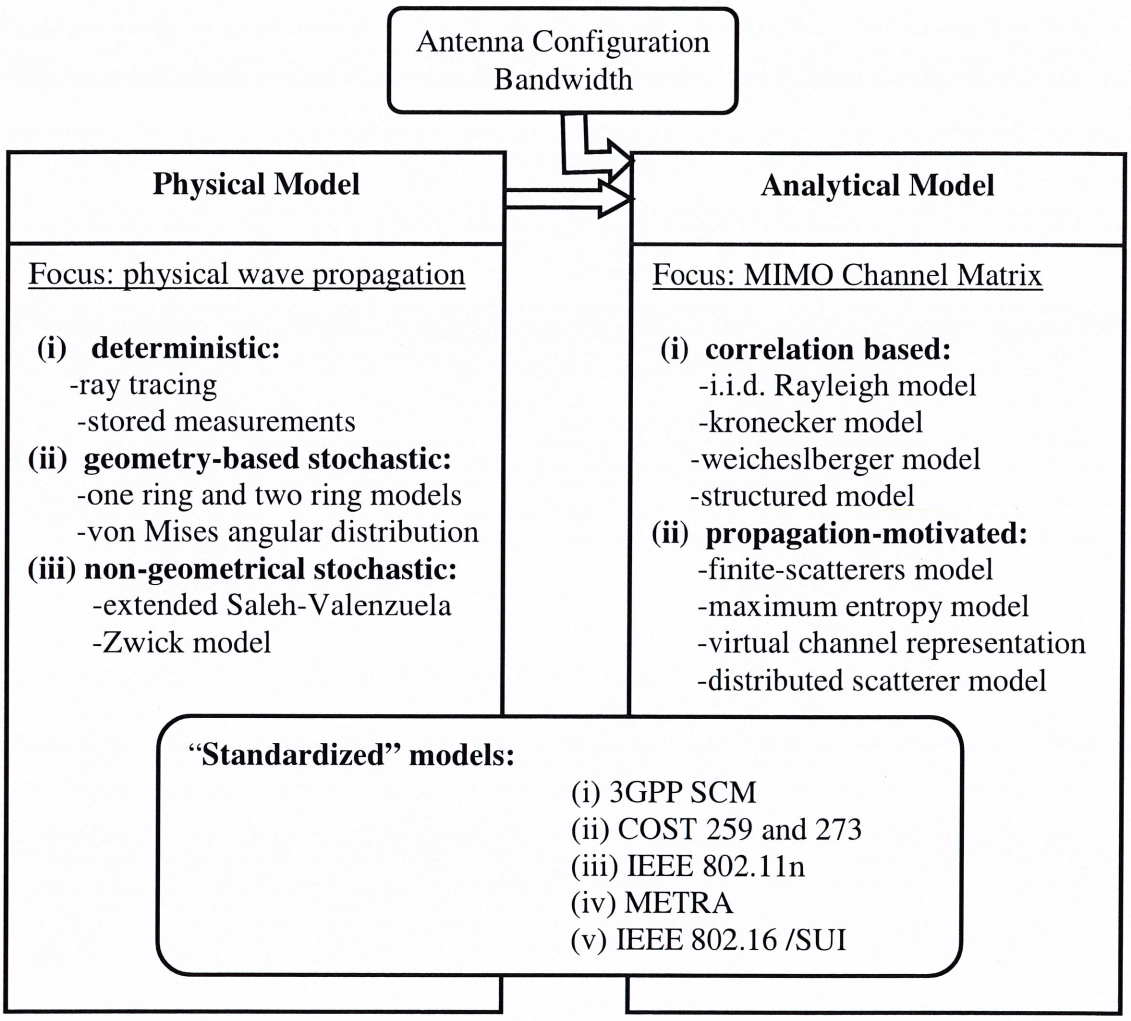


Fig. 2.3 Classification of MIMO channel and propagation models.

The Physical channel models characterize an environment on the basis of electromagnetic wave propagation by describing the double-directional multipath propagation between the location of the transmit (Tx) array and the location of the receive (Rx) array. In general, these models select some vital physical parameters to describe the MIMO propagation channels like the complex amplitude, Angle of Departure (AOD), Angle of Arrival (AOA), and Time of Arrival (TOA). In addition, physical models are independent of antenna configurations

(antenna pattern, number of antennas, array geometry, polarization, mutual coupling) and system bandwidth. On the other hand, analytical channel models characterize the channel impulse response between individual transmit and receive antennas in a mathematical/analytical way without accounting for wave propagation. Analytical models are very popular for synthesizing MIMO matrices in the context of system and algorithm development and verification [18] [19].

2.3.1 Physical Models

2.3.1.1 Deterministic Physical Models

In deterministic models, the environment (position of Tx, Rx, and scatterers) is characterized in a deterministic manner and thereafter the fundamental Maxwell's equations are solved using one of the widely known methods of electromagnetism (*Method of Moments* (MOM), *Finite Difference Time Domain* (FDTD) method, and *Finite Element* (FE) method) [20]. These models are often the most accurate but are by far the most complex. The most known deterministic model is the *ray tracing* (RT) model [21] that is based on electromagnetic propagation mechanisms. It requires a complete description of every object in the channel, including doors, walls, and desks. This includes each object's geometry, location, and scattering properties.

2.3.1.2 Geometry-Based Stochastic Physical Channel Model

In geometry-based stochastic channel models (GSCMs), the location of scatterers is chosen stochastically (randomly) according to a certain probability density function (PDF) and the model is derived from the position of the scatterers by applying the fundamental laws of propagation mechanisms. The well-known GSCMs are *one-ring model*, *two-ring model*, and *von Mises angular distribution model.*

i. One-Ring Model

In the narrowband 'one-ring' model [8], the base station (BS) is assumed to be elevated and therefore not obstructed by local scattering while the mobile station (MS) is surrounded by scatterers. No LOS is assumed between the BS and MS. Fig. 2.4 illustrates this scenario, where T_p and T_q are the pth and qth antenna element at the BS, respectively, R_n and R_m are the nth and mth antenna element at the MS, respectively, D is the distance between the BS and MS, R is the radius of the ring of scatterers, θ_r is the AOA at the BS, and σ is angle

spread. The effective scatterer on the ring is denoted by $S(\theta)$ and θ is the angle between the scatterer and the array at the MS. $S(\theta)$, is *uniformly distributed* in θ with a phase shift, $\varphi(\theta)$.

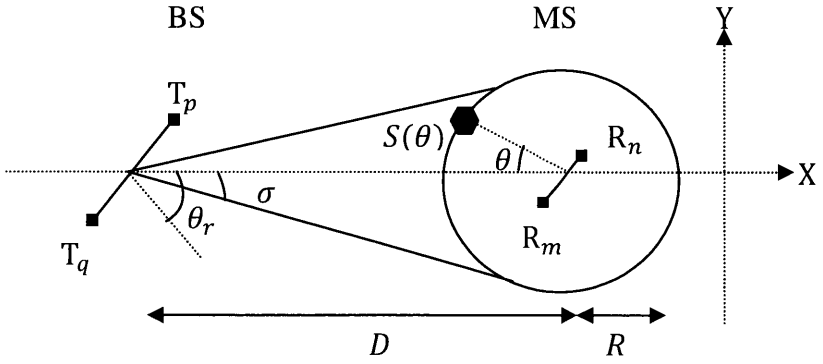


Fig. 2.4 Illustration of the one-ring model.

The complex channel coefficient between the pth element at the BS and nth element at the MS can be expressed as

$$H_{p,n} = \frac{1}{\sqrt{L}} \sum_{i=1}^{L} e^{\left\{-j\frac{2\pi}{\lambda}\left(D_{T_p \to S(\theta_i)} + D_{S(\theta_i) \to R_n}\right) + j\varphi(\theta_i)\right\}} \tag{2.9}$$

where $D_{X \to Y}$ denotes the distance between X and Y, λ is the wavelength, and L is the number of effective scatterers distributed on the ring.

ii. Two-Ring Model

The narrowband 'two-ring' model [22] assumes that both the BS and MS are surrounded by scatterers. This can be the case for indoor wireless communications. An illustration of the two-ring model is shown in Fig. 2.5. Notice that in this model, each ray is reflected twice and the channel coefficient for the two-ring model is

$$H_{p,n} = \frac{1}{\sqrt{K_1 K_2}} \sum_{k=1}^{K_1} \sum_{l=1}^{K_2} e^{\left\{-j\frac{2\pi}{\lambda}\left(D_{T_p \to S_1(\alpha_k)} + D_{S_1(\alpha_k) \to S_2(\beta_l)} + D_{S_2(\beta_l) \to R_n}\right) + j\varphi(\alpha_k) + j\varphi(\beta_l)\right\}} \tag{2.10}$$

where K_1 and K_2 are the numbers of scatterers distributed on the two rings.

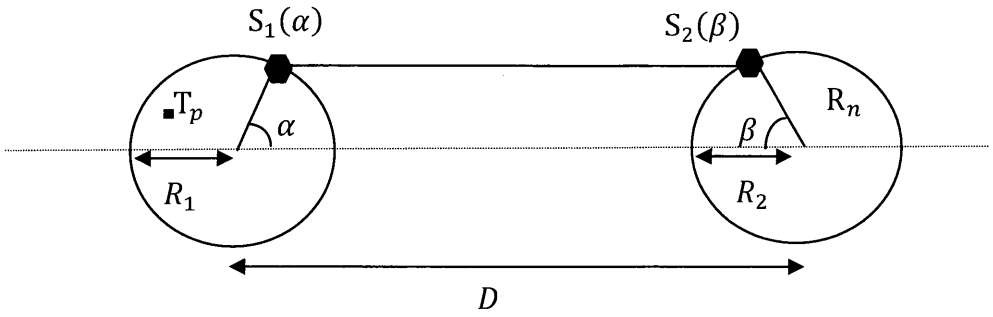


Fig. 2.5 Illustration of the two-ring model.

iii. Von Mises Angular Distribution

Similar to the one-ring model, a narrowband model was presented in [23] that uses the Von Mises angular PDF as the angular PDF at the mobile side and takes the Doppler spread into account. Fig. 2.6 illustrates this model.

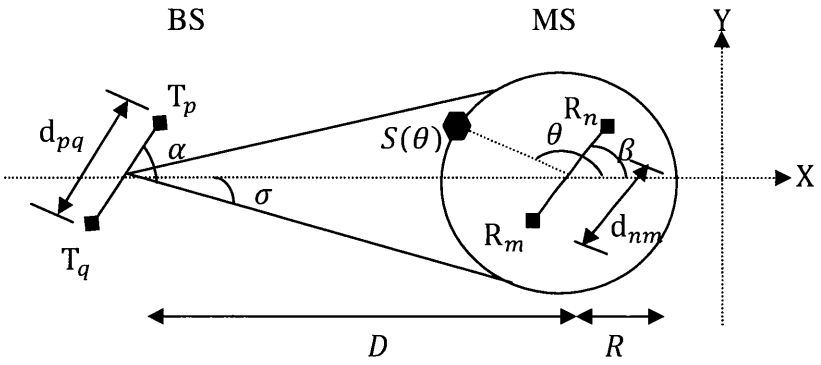


Fig. 2.6 Illustration of the one-ring model using Mises angular distribution.

The cross-correlation between two normalized channel coefficients can be approximated as follows:

$$E\left[\mathrm{H}_{p,n}(t)\mathrm{H}_{q,m}^{H}(t+\tau)\right] = \mathrm{e}^{\left(\frac{j2\pi \mathrm{d}_{pq}\cos\alpha}{\lambda}\right)} \int_{0}^{2\pi} \mathrm{e}^{\left(\frac{j2\pi}{\lambda}[\mathrm{d}_{pq}\sigma\sin(\alpha)\sin(\theta)+\mathrm{d}_{nm}\cos(\theta-\beta)]-j2\pi f_D[\cos(\theta-\varphi)]\tau\right)} p(\theta)d\theta \quad (2.11)$$

where $[.]^H$ denotes the Hermitian transpose, $f_D = {}^{v}/_{\lambda}$ is the Doppler shift, v is the speed of the MS, φ is the moving direction of the MS, τ is the relative time difference between the two links $\mathrm{H}_{p,n}$ and $\mathrm{H}_{q,m}$, and $p(\theta)$ is the Von Mises PDF which is defined by

$$p(\theta) = \frac{e^{[\kappa \cos(\theta - \theta_r)]}}{2\pi I_0(\kappa)} \tag{2.12}$$

The parameter κ can be chosen between 0 (isotropic scattering) and ∞ (extreme non-isotropic scattering). One important advantage of using the Von Mises angular distribution is that it gives a closed-form expression [23] and therefore, can be used to study the channel correlation analytically.

2.3.1.3 Non-Geometrical Stochastic Physical Channel Models

The non-geometrical stochastic models describe paths from transmitter to receiver by statistical parameters only, without reference to the geometry of the physical environment. There are two classes of stochastic non-geometrical models, namely: *extended Saleh-Valenzuela model* and *Zwick model*. The first one uses clusters of *multipath components* (MPCs), whereas, the second one treats MPCs individually.

i. Extended Saleh-Valenzuela Model

The first comprehensive statistical channel model, specifically for an indoor multipath environment, was proposed by Saleh and Valenzuela (SV) in [24]. They showed that the energy in a wideband channel arrived in clusters and that each cluster consisted of several MPCs. The clusters are defined as an accumulation of MPCs with similar temporal and angular characteristics. The arrival times of clusters and MPCs within the cluster were modeled as independent Poisson processes, each with a different rate. Furthermore, both the power of MPCs within a cluster as well as the average cluster power follows an exponential decay over time, as shown in Fig. 2.7.

The arrival time of each cluster is defined as the arrival of the first multipath associated with that cluster. The *cluster arrival time* τ_c is a Poisson process with rate λ_c, whose conditional distribution is given by

$$p(\tau_c|\tau_{c-1}) = \lambda_c e^{-\lambda_c(\tau_c - \tau_{c-1})} \quad \text{for } c > 0 \tag{2.13}$$

where $\tau_0 = 0$. Let $\tau_{c,l}$ be the *arrival time* of the lth MPC in cluster c. The MPC arrival time is also a Poisson process, with rate $\lambda_{c,l}$, and is independent of τ_c. The conditional distribution is given by

$$p(\tau_{c,l}|\tau_{c,l-1}) = \lambda_{c,l} e^{-\lambda_{c,l}(\tau_{c,l}-\tau_{c,l-1})} \quad \text{for } l > 0 \tag{2.14}$$

where the delay of the first multipath in each cluster is assumed to be zero (i.e., $\tau_{c,0} = 0$).

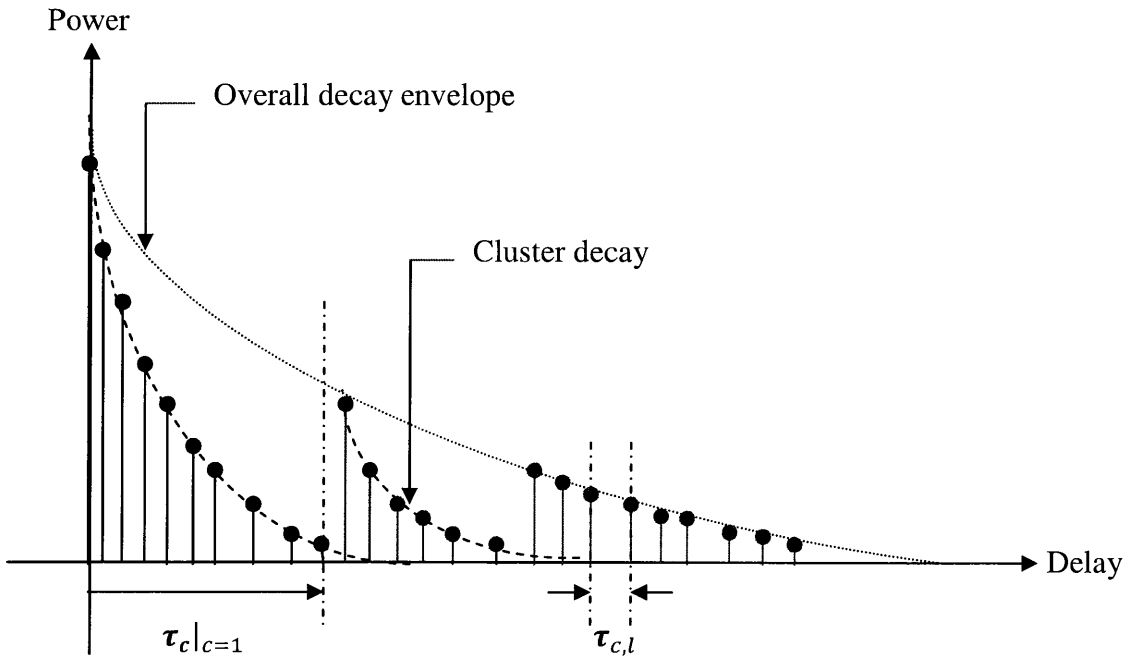


Fig. 2.7 Cluster Structure in the Saleh-Valenzuela model.

The time-invariant channel impulse response $h(\tau)$ is computed as the sum contribution of all MPCs in all clusters,

$$h(\tau) = \sum_{c=0}^{\infty} \sum_{l=0}^{\infty} a_{c,l}\, e^{j\varphi_{c,l}} \delta(\tau - \tau_c - \tau_{c,l}) \tag{2.15}$$

where $\delta(.)$ is the delta Dirac function, $a_{c,l}$ and $\varphi_{c,l}$ are the *gain* and the *phase* of the *l*th MPC in cluster *c*, respectively. $\varphi_{c,l}$ is assumed to be uniformly distributed on $[0,2\pi)$. The gain term $a_{c,l}$ is real and governs the power of each cluster, as well as the slope of the overall decay envelope. Its mean squared value $\overline{a_{c,l}^2}$ can be approximated as a function of two decaying exponential, as shown by

$$\overline{a_{c,l}^2} = \overline{a_{0,0}^2} e^{-\tau_c/\Gamma} e^{-\tau_{c,l}/\gamma} \tag{2(2.16)}$$

where $\overline{a_{0,0}^2}$ is the average power of the first multipath component in the cluster, and Γ, γ are the overall decay rate and cluster decay rate, respectively. The gains themselves are Rayleigh-distributed random variables, with PDF

$$p(a_{c,l}) = \frac{2a_{c,l}}{\overline{a_{c,l}^2}} e^{a_{c,l}^2/\overline{a_{c,l}^2}} \tag{2.17}$$

The SV model excludes any AOA, AOD characterization. Therefore, numerous publications since then have extended the model to include the azimuth and elevation domains, such as, the enhancements proposed by Spencer *et al.* [25] and Wallace and Jensen [26], these where published for the *single input multiple output / multiple input single output* (SIMO/MISO) and narrowband MIMO, respectively. The spatial enhancements proposed deal with the AOA in [25], and both the AOA and AOD in [26]. From measurements carried out in indoor environments [25], it was found that MPC clusters are not spread out in delay but also in AOA. Thus, the original SV model was extended to include angles of arrival, θ_r, as indicated by the equation

$$h(\tau, \theta_r) = \sum_{c=0}^{\infty} \sum_{l=0}^{\infty} a_{c,l}\, e^{j\varphi_{c,l}} \delta(\tau - \tau_c - \tau_{c,l}) \delta(\theta_r - \Theta_c^r - \theta_{c,l}^r) \tag{2.18}$$

where Θ_c^r is the mean AOA for cluster c, while $\theta_{c,l}^r$ is the relative AOA of the lth MPC in the cth cluster. An extension to [25] was proposed in [26] for the narrowband case, which includes both AOAs and AODs. The new expression is

$$h(\tau, \theta_t, \theta_r) = \sum_{c=0}^{\infty} \sum_{l=0}^{\infty} a_{c,l}\, e^{j\varphi_{c,l}} \delta(\tau - \tau_c - \tau_{c,l}) \delta(\theta_t - \Theta_c^t - \theta_{c,l}^t) \delta(\theta_r - \Theta_c^r - \theta_{c,l}^r) \tag{2.19}$$

where Θ_c^t is the mean AOD for cluster c, while $\theta_{c,l}^t$ is the relative AOD of the lth MPC in the cth cluster. The mean AOD and AOA (cluster centers) are uniformly distributed over $[0,2\pi)$, while a zero-mean *Laplacian* PDF with standard deviation σ is assigned to the MPCs within each cluster at both ends

$$p(\theta_{c,l}) = \frac{1}{\sigma\sqrt{2}} e^{-|\sqrt{2}\theta_{c,l}/\sigma|} \tag{2.20}$$

Over the years, the SV model has been shown to be quite accurate. Elements of the model can be seen in many channel models published since then, including the 3GPP *spatial channel model* (SCM) [27], COST 259 [28] and 802.11 TG*n* standard [11] models.

ii. Zwick Model

In [29] it is shown that for indoor channels clustering and multipaths fading do not occur when the sampling rate is sufficiently high. As a result, in the Zwick model, MPCs are generated independently (no clustering) and without amplitude fading. The time-variant frequency dependant channel model can be written as

$$\mathbf{H}(t,f,\theta_t,\theta_r) = \sum_{l=1}^{\mathrm{L}(t)} \Gamma_l(t) e^{-j2\pi f \tau_l(t)} \delta(\theta_t - \theta_{t,l}(t)) \delta(\theta_r - \theta_{r,l}(t)) \tag{2.21}$$

where $\Gamma_l(t)$ is the full polarimetric matrix whose entries contain the losses and depolarization of all scattering processes (reflections, diffractions, etc.) of the lth MPC. τ_l, $\theta_{t,l}$, $\theta_{r,l}$ are the TOA, AOD, AOA of the lth MPC, respectively. The main model's advantage is that it enables the transition between LOS and NLOS configurations in an easy manner by modelling the LOS component separately from all other MPCs. This allows using the same basic procedure for both LOS and NLOS environments. However, the relatively large number of frequency-dependant site-specific parameters that need to be defined and the fact that the time-dispersion of individual MPC is neglected are the main drawbacks of this model.

2.3.2 Analytical Models

The analytical models are very popular for developing the MIMO algorithm, since they are able to capture the channel matrix from a mathematical viewpoint.

2.3.2.1 Correlation-Based Analytical Models

Various narrowband analytical models are based on a *multivariate complex Gaussian distribution* [18] of the MIMO channel coefficients. The zero-mean multivariate complex Gaussian distribution of $\mathbf{h} = \mathrm{vec}\{\mathbf{H}\}$ is given by

$$p(\mathbf{h}) = \frac{1}{\pi^{M_t M_r} \det\{\mathbf{R}_H\}} e^{-\mathbf{h}^H \mathbf{R}_H^{-1} \mathbf{h}} \tag{2.22}$$

where vec{.} stacks the columns of a matrix into a vector and $\mathbf{R}_H$ is the *full spatial correlation matrix* describing the spatial behavior of the MIMO channel since it contains the mutual correlation complex values between all channel matrix elements, and can be represented as

$$\mathbf{R}_H = E\{\mathbf{h}\mathbf{h}^H\} \in \mathbb{C}^{M_t M_r \times M_t M_r} \tag{2.23}$$

A direct physical interpretation of the elements of $\mathbf{R}_H$ is not possible though and thus different approximations of $\mathbf{R}_H$ have been proposed that rely on a separability assumption between the transmit/receive correlation matrices or on a decomposition in the eigen/beam-space. Realizations of MIMO channels with distribution (2.22) can be obtained by

$$\mathbf{H} = \text{unvec}\{\mathbf{h}\} \quad \text{with } \mathbf{h} = {\mathbf{R}_H}^{1/2}\mathbf{h}_{iid} \tag{2.24}$$

where unvec{.} is the inverse operator of vec{.}, ${\mathbf{R}_H}^{1/2}$ denotes an arbitrary matrix square root (i.e., any matrix satisfying ${\mathbf{R}_H}^{1/2}{\mathbf{R}_H}^{H/2} = \mathbf{R}_H$), and $\mathbf{h}_{iid} \in \mathbb{C}^{M_t M_r \times 1}$ is a complex-Gaussian *independent and identically distributed* (i.i.d.) vector. The elements of $\mathbf{h}_{iid}$ are i.i.d. circularly symmetric complex Gaussian with zero mean and unit variance.

i. i.i.d. Rayleigh Channel Model

The simplest analytical MIMO model is the i.i.d. Rayleigh model, it was the initial scheme for assessing the performance of MIMO channels and the most analytical tool for the design of space-time codes. The entries of the MIMO channel matrix $\mathbf{H}$ are assumed to be i.i.d. zero-mean complex Gaussian variables, that is, all elements of $\mathbf{H}$ are uncorrelated (and hence statistically independent). Physically, this corresponds to a spatially white MIMO channel which occurs when the antenna spacing and/or the angular spread are high enough to induce independent fading (zero spatial correlation) and a large number of independent MPCs uniformly distributed impinge on the Rx from all directions, then the correlation matrix becomes proportional to the identity matrix ($\mathbf{R}_H \propto \mathbf{I}$). In practice the spatial sub-channels are rarely uncorrelated due to the limited angular spreads and array sizes.

In the same way, the presence of a strong LOS component may disobey the assumption of Rayleigh fading causing the channel statistics to be Ricean distributed.Therefore, the channel matrix will consist of a spatially deterministic component $\mathbf{H}_d$, which contains the free-space

responses between all antennas, and a random stochastic Rayleigh-distributed component $\mathbf{H}_s$ which accounts for the scattered signals. The channel response is given as [30]

$$\mathbf{H} = \sqrt{\frac{1}{K+1}}\mathbf{H}_s + \sqrt{\frac{K}{K+1}}\mathbf{H}_d \tag{2.25}$$

ii. Kronecker Model

The Kronecker model [17] is based on the assumption that scatterers around the transmitter are uncorrelated with respect to those around the receiver. Thus, the spatial transmitter and receiver correlation are separable, which is equivalent to correlation matrices that can be written as Kronecker product

$$\mathbf{R}_H = \mathbf{R}_{\text{Tx}} \otimes \mathbf{R}_{\text{Rx}} \tag{2.26}$$

where $\otimes$ returns the Kronecker product of two matrices, $\mathbf{R}_{\text{Tx}}$ and $\mathbf{R}_{\text{Rx}}$ are the Tx and Rx correlation matrices, respectively

$$\begin{aligned} \mathbf{R}_{\text{Tx}} &= E\{\mathbf{H}^H\mathbf{H}\} \in \mathbb{C}^{M_t \times M_t} \\ \mathbf{R}_{\text{Rx}} &= E\{\mathbf{H}\mathbf{H}^H\} \in \mathbb{C}^{M_r \times M_r} \end{aligned} \tag{2.27}$$

The Kronecker product between two matrices is defined as

$$\mathbf{A}_{m\times n} \otimes \mathbf{B}_{p\times q} = \begin{bmatrix} \mathbf{A}(1,1)\mathbf{B} & \mathbf{A}(1,2)\mathbf{B} & \dots & \mathbf{A}(1,n)\mathbf{B} \\ \mathbf{A}(2,1)\mathbf{B} & \mathbf{A}(2,2)\mathbf{B} & \dots & \mathbf{A}(2,n)\mathbf{B} \\ \vdots & \vdots & \ddots & \vdots \\ \mathbf{A}(m,1)\mathbf{B} & \mathbf{A}(m,2)\mathbf{B} & \dots & \mathbf{A}(m,n)\mathbf{B} \end{bmatrix}_{mp\times nq}$$

It can be shown that under the above assumption, (2.24) simplifies to the *Kronecker model*

$$\mathbf{h} = (\mathbf{R}_{\text{Tx}} \otimes \mathbf{R}_{\text{Rx}})^{1/2}\mathbf{h}_{iid} \Leftrightarrow \mathbf{H} = \mathbf{R}_{\text{Rx}}^{1/2}\mathbf{H}_{iid}\,\mathbf{R}_{\text{Tx}}^{1/2} \tag{2.28}$$

where $\mathbf{H}_{iid} = \text{unvec}(\mathbf{h}_{iid})$. The Kronecker model is popular because of its simple analytical treatment. However, the main drawback of this model is that it forces both link ends to be separable, irrespective of whether the channel supports this or not.

iii. Weichselberger Model

The idea of Weichselberger model [31] was to relax the separability restriction of the Kronecker model and allow coupling between the transmitter and receiver eigenbases, i.e., to model the correlation properties at the receiver and transmitter jointly. Introducing the eigenvalue decomposition (EVD) of the Rx and Tx correlation matrices

$$\begin{aligned}\mathbf{R}_{\mathrm{Rx}} &= \sum_{m=1}^{M_r} \lambda_{\mathrm{Rx},m}\mathbf{u}_{\mathrm{Rx},m}\,\mathbf{u}_{\mathrm{Rx},m}^{H} = \mathbf{U}_{\mathrm{Rx}}\boldsymbol{\Lambda}_{\mathrm{Rx}}\mathbf{U}_{\mathrm{Rx}}^{H} \\ \mathbf{R}_{\mathrm{Tx}} &= \sum_{n=1}^{M_t} \lambda_{\mathrm{Tx},n}\mathbf{u}_{\mathrm{Tx},n}\,\mathbf{u}_{\mathrm{Tx},n}^{H} = \mathbf{U}_{\mathrm{Tx}}\boldsymbol{\Lambda}_{\mathrm{Tx}}\mathbf{U}_{\mathrm{Tx}}^{H}\end{aligned} \tag{2.29}$$

where $\mathbf{u}_{\mathrm{Rx},m}$ and $\mathbf{u}_{\mathrm{Tx},n}$ are the *receive* and *transmit eigenvectors*, and $\mathbf{U}_{\mathrm{Rx}}$ and $\mathbf{U}_{\mathrm{Tx}}$ are the *receive* and *transmit eigenbases*, respectively. $\boldsymbol{\Lambda}_{\mathrm{Rx}}$ and $\boldsymbol{\Lambda}_{\mathrm{Tx}}$ are diagonal matrices with the corresponding eigenvalues. The coupling between the two ends is determined by the power *coupling matrix* $\boldsymbol{\Omega}$ whose positive and real-valued coefficients ω_{mn} specify the mean amount of energy coupled from nth transmit eigenvector to the mth receive eigenvector; that is

$$\begin{aligned}\omega_{mn} &= \mathrm{E}\left\{\left\|\mathbf{u}_{\mathrm{Rx},m}^{H}\mathbf{H}\mathbf{u}_{\mathrm{Tx},n}^{*}\right\|^{2}\right\} \\ &= \left(\mathbf{u}_{\mathrm{Tx},n}\otimes\mathbf{u}_{\mathrm{Rx},m}\right)^{H}\mathbf{R}_{H}\left(\mathbf{u}_{\mathrm{Tx},n}\otimes\mathbf{u}_{\mathrm{Rx},m}\right)\end{aligned} \tag{2.30}$$

where $[\cdot]^{*}$ denotes complex conjugate, ω_{mn} is referred to as the *coupling coefficient* and can be arranged in matrix form as

$$\boldsymbol{\Omega} = \begin{pmatrix} \omega_{11} & \cdots & \omega_{1M_t} \\ \vdots & \ddots & \vdots \\ \omega_{M_t1} & \cdots & \omega_{M_rM_t} \end{pmatrix} \tag{2.31}$$

$\widetilde{\boldsymbol{\Omega}}$ is the element-wise square root of $\boldsymbol{\Omega}$ such that

$$\widetilde{\boldsymbol{\Omega}} = \begin{pmatrix} \sqrt{\omega_{11}} & \cdots & \sqrt{\omega_{1M_t}} \\ \vdots & \ddots & \vdots \\ \sqrt{\omega_{M_t1}} & \cdots & \sqrt{\omega_{M_rM_t}} \end{pmatrix} \tag{2.32}$$

Subsequently, the Weichselberger channel model can be written as [31]

$$\mathbf{H} = \mathbf{U}_{\mathrm{Rx}}(\tilde{\Omega} \odot \mathbf{G})\mathbf{U}_{\mathrm{Tx}}^{T} \tag{2.33}$$

where $\odot$ returns the element-wise Schur Hadamard multiplication and $[\cdot]^T$ denotes matrix/vector transpose.

iv. Structured Model

The structure model is the extension of the Weichselberger model to the wideband MIMO channel. It uses tensor[1] calculus to describe the coupling between scatterers across receive-transmit-delay space [17] [32]. It recasts the MIMO channel matrix as a tensor to account for correlation in all domains and especially between delay bins in the *power delay profile* (PDP). Assuming D delay bins, the model's key equation is given by

$$\mathbf{H} = \mathcal{W} \times_1 \mathbf{U}_{\mathrm{Rx}} \times_2 \mathbf{U}_{\mathrm{Tx}} \times_3 \mathbf{U}_{\mathrm{Del.}} \tag{2.34}$$

where $\times_n$ denotes the n-mode product, $\mathbf{U}_{\mathrm{Del.}}$ is the eigenbases of the delay correlation matrix, and $\mathcal{W} \in \mathbb{C}^{M_r \times M_t \times D}$ is a tensor whose entries reflect the wideband power coupling between the two ends ($\mathrm{w}_{mnd} = \mathrm{g}_{mnd}\sqrt{\omega_{mnd}}$), where g_{mnd} are chosen independently from a complex Gaussain distribution, and ω_{mnd} is the wideband coupling coefficient, That is given by

$$\omega_{mnd} = \left(\mathbf{u}_{\mathrm{Del},d} \otimes \mathbf{u}_{\mathrm{Tx},n} \otimes \mathbf{u}_{\mathrm{Rx},m}\right)^{H} \mathbf{R}_{WB,H}\left(\mathbf{u}_{\mathrm{Del},d} \otimes \mathbf{u}_{\mathrm{Tx},n} \otimes \mathbf{u}_{\mathrm{Rx},m}\right) \tag{2.35}$$

where $\mathbf{R}_{WB,H} \in \mathbb{C}^{M_t M_r D \times M_t M_r D}$ is the wideband correlation matrix.

2.3.2.2 Propagation-based analytical models

i. Finite Scatterers Model

The fundamental assumption of the finite scatterer model is that propagation can be modeled in terms of a finite number L of MPCs as illustrated in Fig. 2.8. Each path is indexed by an integer l and has a defined AOD ($\theta_{t,l}$) from the transmitting array, AOA ($\theta_{r,l}$) at the receiving array, path gain β_l defined as the ratio of the electric/magnetic field at the location of the receiving array to that at the transmitting array, and delay τ_l.

[1] Tensors are multidimensional generalization of matrices.

Assuming narrowband transmission, the channel matrix reads as [33]

$$\mathbf{H} = \sum_{l=1}^{L} \mathbf{a}_r(\theta_{r,l})\, \beta_l \mathbf{a}_t^H(\theta_{t,l}) \tag{2.36}$$

where $\mathbf{a}_r(\theta_{r,l}) \in \mathbb{C}^{M_r x 1}$ and $\mathbf{a}_t(\theta_{t,l}) \in \mathbb{C}^{M_t x 1}$ are the steering vectors at Rx and Tx corresponding to the lth MPC, respectively. The finite scatterers model not only accounts for single and doubly scattered components (paths (a) and (b) in Fig. 2.8) but also for split components (path (c) in Fig. 2.8) which may have a single AOD but subsequently split, resulting in two or more AOAs. Therefore, it may be regarded as a generalized version of most GSCMs which can deal only with single and doubly scattered components.

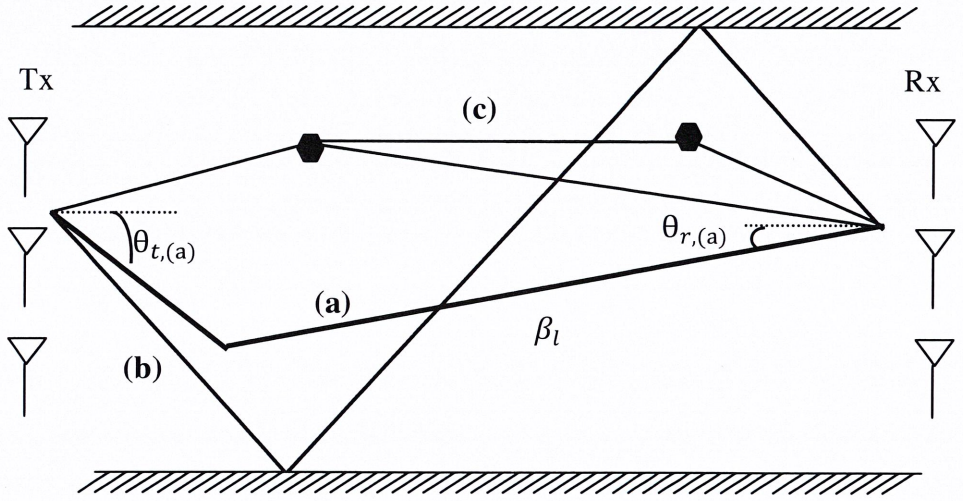


Fig. 2.8 Concept of the finite scatterers channel model, illustrating (a) typical single scattererd path, (b) reflected path, and (c) split component.

ii. Maximum Entropy Model

The maximum entropy principle was proposed to determine the distribution of the MIMO channel matrix based on a priori information that is available. This priori information might include properties of the propagation environment and system parameters (e.g., bandwidth, AODs, etc).The maximum entropy principle was justified by the objective to avoid any model assumptions not supported by the prior information [34]. In order to achieve consistency, regardless of the application of the model, the following axiom was defined:

If the prior information $\mathbf{I}_1$ which is the basis for channel model $\mathbf{H}_1$ is equivalent to the prior information $\mathbf{I}_2$ of channel model $\mathbf{H}_2$, then both models must be assigned the same probability distribution $p(\mathbf{H}_1) = p(\mathbf{H}_2)$. As an example, consider that the following prior information is available:

- number of scatterers at the transmit and receive side S_{Tx} and S_{Rx}, respectively;
- the steering vectors for all Tx and Rx scatterers, contained in the $M_t \times S_{\mathrm{Tx}}$ and $M_r \times S_{\mathrm{Rx}}$ matrices $\mathbf{A}_{\mathrm{Tx}}$ and $\mathbf{A}_{\mathrm{Rx}}$, respectively;
- the corresponding scatterer power $\mathbf{P}_{\mathrm{Tx}}$ and $\mathbf{P}_{\mathrm{Rx}}$; and
- the path gains between Tx and Rx scatterers, characterized by the coupling matrix $(\boldsymbol{\Omega} \in \mathbb{C}^{S_{\mathrm{Rx}} \times S_{\mathrm{Tx}}})$.

Then, the maximum entropy channel model was shown to equal

$$\mathbf{H} = \mathbf{A}_{\mathrm{Rx}} \mathbf{P}_{\mathrm{Rx}}{}^{1/2} (\boldsymbol{\Omega} \odot \mathbf{H}_{iid}) \mathbf{P}_{\mathrm{Tx}}{}^{1/2} \mathbf{A}_{\mathrm{Tx}}^{T} \tag{2.37}$$

where $\mathbf{H}_{iid} \in \mathbb{C}^{S_{\mathrm{Rx}} \times S_{\mathrm{Tx}}}$ is Gaussian matrix with i.i.d. elements. The main advantage of this approach is its flexibility since every new piece of information on the environment can be straightforwardly incorporated in a consistent way.

iii. Virtual Channel Representation

The virtual channel representation (VCR) is a well-mannered linear model, valid for uniform linear arrays (ULAs). The main idea is that the finite number of antennas represents discrete sampling in the aperture domains which are directly related to the angular domains via a Fourier transform (FT). The use of FT explains why the model can be applied simply to ULA configurations as the sampling needs to be uniform in the aperture domain. The model is virtual in the sense that it does not represent the real directions but only the contribution of the channel to those fixed directions. The VCR can be expressed as [35]

$$\mathbf{H} = \mathbf{F}_{\mathrm{Rx}} (\widetilde{\boldsymbol{\Omega}}_{\mathrm{virt}} \odot \mathbf{H}_{iid}) \mathbf{F}_{\mathrm{Tx}}^{T} \tag{2.38}$$

where $\mathbf{F}_{\mathrm{Rx}} \in \mathbb{C}^{M_r \times M_r}$ and $\mathbf{F}_{\mathrm{Tx}} \in \mathbb{C}^{M_t \times M_t}$ are the channel independent discrete Fourier transform (DFT) matrices . The columns of these orthonormal matrices constitute steering vectors into the directions of virtual angles. $\widetilde{\boldsymbol{\Omega}}_{\mathrm{virt}} \in \mathbb{C}^{M_r \times M_t}$ is the element-wise square root of $\boldsymbol{\Omega}_{\mathrm{virt}}$ whose entries reflect the power coupling between the nth virtual transmit angle and

the mth receive virtual angle. In this case, the coupling matrix is obtained through (2.31), by using the predefined DFT matrices $\mathbf{F}_{\mathrm{Rx}}$ and $\mathbf{F}_{\mathrm{Tx}}$ instead of the eigenbases $\mathbf{U}_{\mathrm{Rx}}$ and $\mathbf{U}_{\mathrm{Tx}}$, respectively.

iv. Distributed Scatterers Model

The distributed scatterers model was developed to assess the performance of outdoor MIMO systems [36]. The propagation scenario is illustrated in Fig. 2.9. Both the Tx and Rx are surrounded by a set of S actual near-field scatterers whose extent from the horizontal axis is denoted as D_t and D_r, respectively.

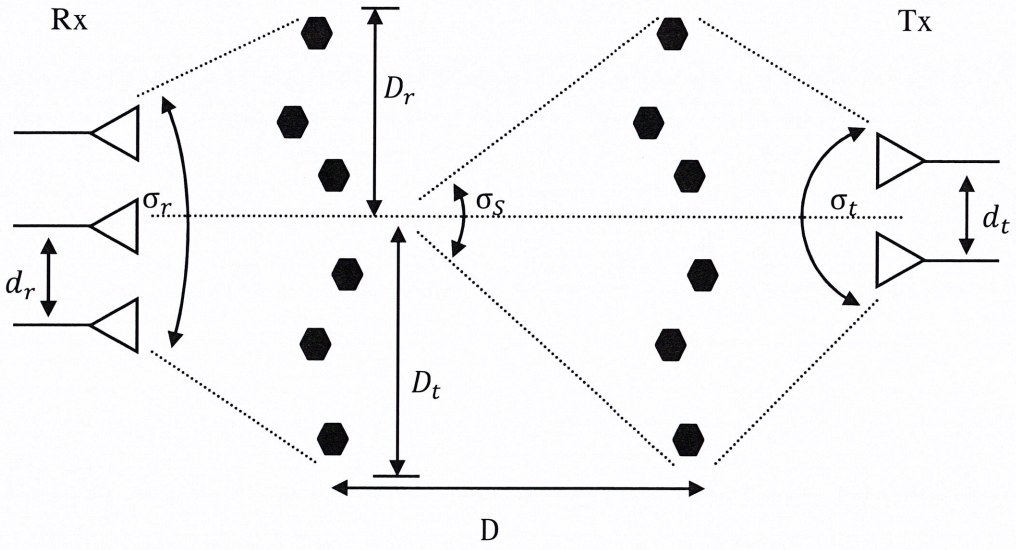


Fig. 2.9 Illustration of the distributed scattering model.

The value of S is assumed to be large enough to induce random fading while the arrangement of scatterers follows no certain pattern. In addition, the angular spreads of the reflected waves are σ_t and σ_r. The inter-element distance at Tx and Rx is expressed as d_t and d_r, respectively; the scatterers at the receive side can be seen as a virtual array of S elements between the Tx and Rx with an average element spacing $2D_r/S$. The MIMO channel transfer function is then written as

$$\mathbf{H} = \frac{1}{\sqrt{S}}\mathbf{R}^{1/2}_{\sigma_r,d_r}\mathbf{H}^{r}_{iid}\mathbf{R}^{1/2}_{\sigma_S,2D_r/S}\mathbf{H}^{t}_{iid}\mathbf{R}^{1/2}_{\sigma_r,d_r} \tag{2.39}$$

where $\frac{1}{\sqrt{S}}$ is a normalization factor , $\mathbf{H}^{r}_{iid} \in \mathbb{C}^{M_r \times S}$ and $\mathbf{H}^{t}_{iid} \in \mathbb{C}^{S \times M_t}$ are i.i.d. Rayleigh fading matrices, and σ_S is the angular spread for the virtual array

$$\tan(\sigma_S/2) = D_t/D \tag{2.40}$$

The deterministic matrices $\mathbf{R}_{\sigma_r,d_r}$, $\mathbf{R}_{\sigma_S,2D_r/S}$, and $\mathbf{R}_{\sigma_r,d_r}$control the spatial correlation seen from Tx, virtual array and the Rx, respectively.

2.3.3 Standardized Models

This section provides a brief review of the most standardized models, established by several international organizations. The standardized models are important tools for developing new radio systems. These models allow assessing the benefits of different techniques (signal processing, multiple access, etc.) for enhancing capacity and improving system performance. The aim is to give the reader a view of recent and ongoing channel modeling activities.

i. 3GPP Spatial Channel Model

The 3rd Generation Partnership Project (3GPP) system-level spatial channel model (SCM) has been designed for the simulation of third-generation networks in outdoor environments (urban microcells, urban and suburban macrocells) at a center frequency of 2 GHz and system bandwidth of 5 MHz [27]. SCM is a geometry- based stochastic channel model was developed for the purpose of calibration, where taps with different delays are assumed independent and can be fully characterized by their spatial parameters, i.e. angular spread, power azimuth spectrum (PAS), AOA/AOD. The model structure and simulation methodology are identical for all environments but the input parameters, like delay spread, angular spread and so forth, are different. In [27], a parameter table has been given which lists all the important parameters, such as number and power of paths and subpaths and spatial parameters.

ii. IEEE 802.11*n* Channel Model

This set of channel models, developed by High Throughput Task Group within the IEEE 802.11*n* Working Group, have been designed for indoor WLAN at both 2 GHz and 5 GHz with an operating bandwidth of 100 MHz [11]. These models essentially represent an improved and standardized version of the SV model with overlapping clusters in the delay domain. Six environments (A to F) are modeled, namely: flat-fading, residential, small office, typical office, large office, and open space. The IEEE 802.11*n* channel model is a physical

model, using a nongeometric stochastic approach. The directional impulse response is described as a sum of clusters. Each cluster consists of up to 18 delay taps (separated by at least 10 nanoseconds), and to each tap is assigned AOA and a truncated Laplacian PAS with angular spread ranging from 20^{o} to 40^{o} (and similar for the AOD). The number of clusters range from 2 to 6 (these numbers were found based on measurement data), and the overall RMS delay spread varies between 0 (flat fading) and 150 nanoseconds. This model would be studied in more details in the next chapter.

iii. METRA

The Multi-Element and Receive Antennas (METRA) channel model was developed within the Information Society Technologies (IST). The main objective of the IST METRA project was to analyze the feasibility and evaluate the performance of introducing multi-element adaptive antennas into mobile terminals in combination with adaptive base station antenna arrays for Universal Mobile Telecommunication Services (UMTS). The purpose of the channel characterization work in METRA was to accurately exploit the measurement data collected during the Smart Universal Beam-forming (SUNBEAM) in order to get a better insight in properties of MIMO radio channels. Influences of a large set of parameters and contexts, such as correlation, polarization, directional information, power imbalance, and presence of a LOS component have been studied in METRA. More information about METRA can be found in [37] [38].

iv. COST 259/273 Channel Models

"COST" is an abbreviation for *European cooperation in the field of scientific and technical research.* Several COST initiatives were dedicated to wireless communications, in particular COST 259 "Flexible personalized wireless communications" (1996-2000) [28] and COST 273 "Towards mobile broadband multimedia networks" (2001-2005) [39]. Both subprojects aimed to develop efficient and generalized radio channel models suitable for modern MIMO communications. The 3GPP and 802.11*n* models can be viewed as special cases of COST models (though with different parameter settings). The COST 259 is a physical model; it was the first model which explicitly investigated the complex relationships between BS- MS distance, delay dispersion, and angular spread. It is also general in the sense that it is defined for 13 different radio environments (e.g., typical urban, bad urban, Open Square, indoor office, and indoor corridor) that include macrocellular, microcellular, and picocellular

scenarios. The model relies on the key notations of *external* and *global* parameters. The former are fixed for a simulation run and include the following features of the simulation environments among others: frequency band, average BS-MS distance, average height of BS and MS antennas and average building heights and separations. The latter parameters must be extracted by exhaustive real-life measurement trials since their scope is to describe the propagation conditions of radio environments; in fact, they are sets of PDFs and/or statistical moments of the stochastic parameters. The main advantage of the COST 259 model is that it can handle the continuous motion the MS. However, there are two fundamental disadvantages of the COST 259 model. The first one is the assumption of stationary scatterers which implies that time variations are attributed only to the MS movement. Secondly, delay attenuations are modeled as complex Gaussian random variables which, in practice, mean that a relatively high number of MPCs should be present at each delay bin. The COST 273 model represents an extended version of the COST 259, since 10 different radio environments are considered (compared to 13) including some scenarios of high practical interest nowadays, such as peer-to-peer communications and fixed wireless access. The COST 273 employs the same generic channel model for all types that is also identical to that of COST 259 for macrocells; this is a significant distinction to the COST 259 model, which used different generic model for pico-, micro-, and macrocells. The key methodology of COST 273 is to model the mean angles and delays of clusters by geometrical considerations. The concept of *twin clusters* is introduced so that each cluster is divided into a cluster corresponding to the BS side and one at the MS. The angular dispersion at BS and MS are independently modeled while the two clusters have the same scatterer distributions. The two cluster representations are linked via a *stochastic cluster link delay*, which is the same for all scatterers within a cluster. This link delay guarantees realistic path delays while the placement of the cluster is defined by the angular cluster statistics as seen from the BS and MS, respectively.

v. SUI Models and IEEE 802.16

The Stanford university interim (SUI) channel models were developed for macro cellular fixed wireless access networks operating at 2.5 GHz, which were further enhanced in the framework of the IEEE 802.16 standard [40]. The targeted scenario for these models is as follows:

- Cell size is less than 10 km in radius;

- User's antenna is fixed and installed on rooftop (no LOS is required);
- BS height is 15 to 40 m, above rooftop level;
- System bandwidth is flexible from 2 to 2MHz.

The SUI composed of six typical channel models, all SUI models consist of three taps, and are valid for a distance between Tx and Rx equal to 7 km. The first tap is Ricean distributed for SUI channels 1 to 4, while all other taps are taken as Rayleigh fading. Each tap of any SUI channel is characterized by a single antenna correlation coefficient at the user's terminal (UT), irrespective of the UT array configuration, while the antenna correlation at the BS is taken as equal to zero, assuming a large BS antenna spacing. In addition, the antennas were assumed to be omnidirectional at both sides. IEEE 802.16 models are based on a modified version of the SUI channel models, valid for both omnidirectional and directional antennas. However, the model does not modify the correlations at the UT when reducing the antenna beamwidth. Additional features of the IEEE 802.16 standard include a path loss model. The path loss model covers three terrain categories: hilly terrain with moderate-to-heavy tree densities (category *A*, to be used with SUI models 5 and 6), mostly flat terrain with light tree densities (category *C*, to be used with SUI models 1 and 2), and terrain with intermediate path loss condition, captured in category *B* (corresponding to SUI 3 and 4).

2.4 Stochastic Spatial Clustered Channel Model

Spatial fading correlation is one of the crucial impairments in MIMO wireless communication systems. Capacity increases promised by MIMO systems mostly depend on the fading correlation properties of the radio channels. This section investigates the connection between these properties for a MIMO system using both the ULA and UCA geometries utilizing the stochastic spatial clustered (SSC) channel model.

As an initial stage before defining the spatial fading correlation function, it is necessary to develop the vector channel model for the ULA and UCA configurations. The vector channel model is based on the mathematical spatial channel model developed in [9] [10]. An illustration of the wave propagation for spatial channel model employing ULA array is shown in Fig. 2.10.

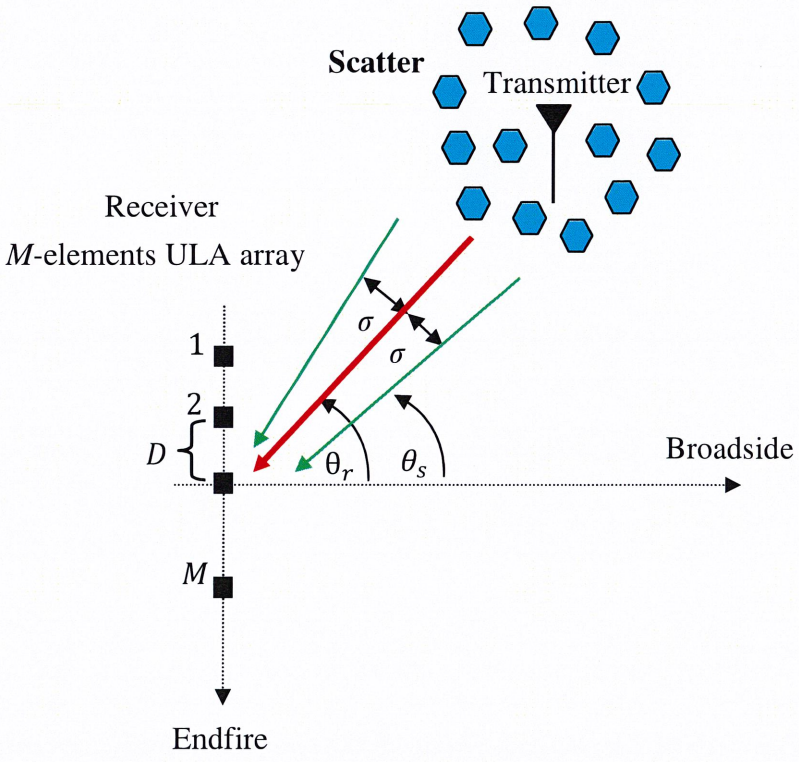


Fig. 2.10 Wireless communication system employing ULA array.

The array *steering vector* $\mathbf{v}(\theta_r)$ for specific arriving plane wave in a ULA can be written as [41]

$$\mathbf{v}(\theta_r) = \begin{bmatrix} v_1(\theta_r) \\ v_2(\theta_r) \\ v_3(\theta_r) \\ \vdots \\ v_M(\theta_r) \end{bmatrix} = \begin{bmatrix} 1 \\ e^{j2\pi\frac{D}{\lambda}\sin(\zeta)\sin(\theta_r)} \\ e^{j2\pi\frac{2D}{\lambda}\sin(\zeta)\sin(\theta_r)} \\ \vdots \\ e^{j2\pi\frac{(M-1)D}{\lambda}\sin(\zeta)\sin(\theta_r)} \end{bmatrix} \tag{2.41}$$

where D is the antenna element spacing, ζ is the elevation angle, and θ_r is the AOA at received antenna array. For simplicity, only the azimuth angles are considered in the propagation geometry ($\zeta = 90^o$). Similarly, Fig. 2.11 shows a wireless communication system employing a UCA array with M evenly spaced receive elements.

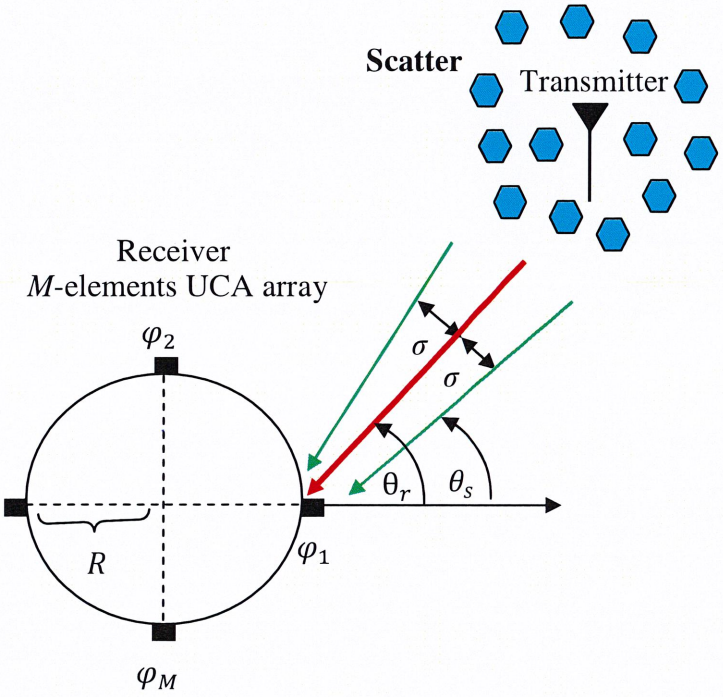


Fig. 2.11 Wireless communication system employing UCA array.

The array steering vector $\mathbf{v}(\theta_r)$ for a single received plane wave in a UCA can be written as [41]

$$\mathbf{v}(\theta_r) = \begin{bmatrix} v_1(\theta_r) \\ v_2(\theta_r) \\ \vdots \\ v_M(\theta_r) \end{bmatrix} = \begin{bmatrix} e^{j2\pi\frac{R}{\lambda}\cos(\theta_r-\varphi_1)} \\ e^{j2\pi\frac{R}{\lambda}\cos(\theta_r-\varphi_2)} \\ \vdots \\ e^{j2\pi\frac{R}{\lambda}\cos(\theta_r-\varphi_M)} \end{bmatrix} \tag{2.42}$$

where R is the circular radius of the antenna array, and φ_m is the phase excitation of mth element in azimuth plane.

The spatial fading correlation function $\mathrm{R}_s(np, mq)$ between two channels $h_{n,p}$ and $h_{m,q}$ for a MIMO channel can be defined as [41]

$$\mathrm{R}_s(np, mq) = E\left[h_{n,p} h_{mq}^*\right] \tag{2.43}$$

where $h_{n,p}$ is the multipath channel impulse response for the pth transmit antenna at the nth receive antenna elements. Subsequently, $\mathrm{R}_s(np, mq)$ can be written as [41]

$$\begin{aligned} \mathrm{R}_s(np, mq) &= E\left[v_n(\theta_s^{\mathrm{Rx}}) v_p(\theta_s^{\mathrm{Tx}}) v_m^*(\theta_s^{\mathrm{Rx}}) v_q^*(\theta_s^{\mathrm{Tx}})\right] \\ &= \int_{\theta_s^{\mathrm{Tx}}} \int_{\theta_s^{\mathrm{Rx}}} v_n(\theta_s^{\mathrm{Rx}}) v_p(\theta_s^{\mathrm{Tx}}) v_m^*(\theta_s^{\mathrm{Rx}}) v_q^*(\theta_s^{\mathrm{Tx}})\, p(\theta_s^{\mathrm{Tx}}, \theta_s^{\mathrm{Rx}}) d\theta_s^{\mathrm{Tx}} d\theta_s^{\mathrm{Rx}} \end{aligned} \tag{2.44}$$

where $v_n(\theta_s^{\mathrm{Rx}})$ and $v_m(\theta_s^{\mathrm{Rx}})$ are the array response for nth and mth receiving antennas and sth scatterer path at the receiver side, while, $v_p(\theta_s^{\mathrm{Tx}})$ and $v_q(\theta_s^{\mathrm{Tx}})$ are the array response for pth and qth transmitting antennas and sth scatterer path at the transmitter side, and $p(\theta_s^{\mathrm{Tx}}, \theta_s^{\mathrm{Rx}})$ is the joint probability density function of AOD and AOA. For a ULA, $v_i(\theta_s^y)$ can be expressed as

$$v_i(\theta_s^y) = e^{j2\pi \frac{D(i-1)}{\lambda} \sin(\theta_s^y)} \tag{2.45}$$

and for a UCA, $v_i(\theta_s^y)$ can be written as

$$v_i(\theta_s^y) = e^{j2\pi \frac{R}{\lambda} \cos(\theta_s^y - \varphi_i)} \tag{2.46}$$

where $i \in \{n, m, p, q\}$ and $y \in \{\mathrm{Tx}, \mathrm{Rx}\}$. Since θ_s^{Tx} and θ_s^{Rx} are statistically independent, (2.44) can be written as

$$\begin{aligned} \mathrm{R}_s(np, mq) &= \int_{\theta_s^{\mathrm{Tx}}} v_p(\theta_s^{\mathrm{Tx}}) v_q^*(\theta_s^{\mathrm{Tx}})\, p(\theta_s^{\mathrm{Tx}}) d\theta_s^{\mathrm{Tx}} \int_{\theta_s^{\mathrm{Rx}}} v_n(\theta_s^{\mathrm{Rx}})\, v_m^*(\theta_s^{\mathrm{Rx}}) p(\theta_s^{\mathrm{Rx}}) d\theta_s^{\mathrm{Rx}} \\ &= \mathrm{R}_s^{\mathrm{Tx}}(p, q) \mathrm{R}_s^{\mathrm{Rx}}(n, m) \end{aligned} \tag{2.47}$$

where $p(\theta_s^{\mathrm{Tx}})$ and $p(\theta_s^{\mathrm{Rx}})$ are the PDFs of AOD and AOA, respectively. $\mathrm{R}_s^{\mathrm{Tx}}(p, q)$ is the spatial correlation due to transmit antennas, and $\mathrm{R}_s^{\mathrm{Rx}}(n, m)$ is the spatial correlation due to receive antennas. Both $p(\theta_s^{\mathrm{Tx}})$ and $p(\theta_s^{\mathrm{Rx}})$ are known as the Power Azimuth Spectrum (PAS). In [16], it is shown that the pattern of PAS depends mainly on the distribution of the locally-

scattered components. In general, enormous amounts of locally-scattered components are observed by the MT in all different environments. Therefore, its PAS usually follows a uniform distribution. However, for the access point (AP) there are different PAS distributions (e.g. uniform, truncated Gaussian and truncated Laplacian) are observed depending on the characteristics of terrain, which is usually shown to have a small angular spread (AS), AS (σ) is defined as the standard deviation of the PAS distribution in degrees as shown in Fig. 2.10 and Fig. 2.11. Fig. 2.12 shows the PDF for the three PAS distributions with the central angle of incidence (θ) = 0^{o} and σ =20^{o}.

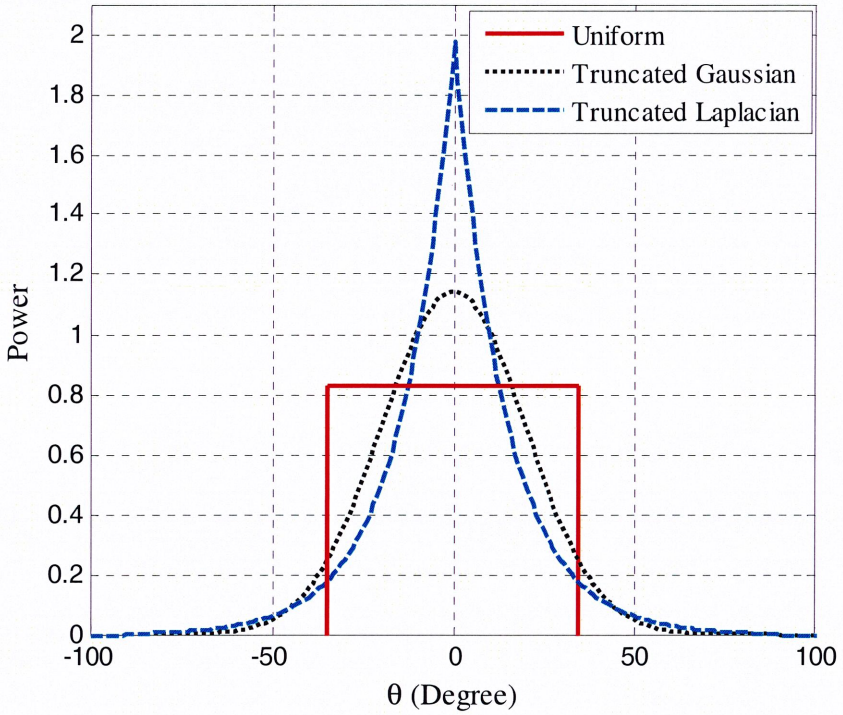


Fig. 2.12 Comparisons for the three PAS distributions ($\theta = 0^{o}$, $\sigma = 20^{o}$).

In this research, the truncated Laplacian PAS distribution at the BS is considered, because it is the best fit to measurement results in urban and rural areas, as revealed in [42]. Also, due to reciprocity of uplink and downlink communications, only the uplink spatial correlation function is presented. Consequently, for the sth scattering path on the uplink, θ_s^{Tx} is the AOD at the MT and θ_s^{Rx} is the AOA at the AP. Both $\theta_s^{\mathrm{Tx}}$and θ_s^{Rx} are random variables. θ_s^{Tx} is assumed uniformly distributed over $[0,2\pi]$. A uniform distribution for θ_s^{Tx} is expressed as

$$p(\theta_s^{\mathrm{Tx}}) = \begin{cases} \frac{1}{2\pi} & -\pi \le \theta_s^{\mathrm{Tx}} \le \pi \\ 0 & \text{otherwise,} \end{cases} \tag{2.48}$$

and θ_s^{Rx} has a truncated Laplacian PAS distribution, which can be expressed as

$$p(\theta_s^{\mathrm{Rx}}) = C_l e^{-a|\theta_s^{\mathrm{Rx}} - \theta_r|} \quad , -\pi + \theta_r \le \theta_s^{\mathrm{Rx}} \le \pi + \theta_r \tag{2.49}$$

where θ_r is the central AOA, and C_l is a normalization factor can be found by

$$\int_{-\pi}^{\pi} C_l e^{-a|\theta_s^{\mathrm{Rx}} - \theta_r|} \, d\theta_s^{\mathrm{Rx}} = 1 \tag{2.50}$$

which gives

$$C_l = \frac{a}{2(1 - e^{-a\pi})} \tag{2.51}$$

and a is a positive decaying factor which is related to the angle spread. Specifically, as a increases the angle spread decreases. The angle spread σ of the Laplacian distribution is defined as

$$\sigma = \frac{2}{a^2} - \frac{2ae^{-a\pi}}{1 - e^{-a\pi}} \left(\frac{\pi^2 a + 2\pi}{a^2} \right) \tag{2.52}$$

Using (2.47) the uplink spatial correlation can be written as

$$\mathrm{R}_s(np, mq)^u = \mathrm{R}_s^{\mathrm{Tx}}(p, q)^u \mathrm{R}_s^{\mathrm{Rx}}(n, m)^u \tag{2.53}$$

where

$$\begin{aligned} \mathrm{R}_s^{\mathrm{Tx}}(p, q)^u &= \int_{\theta_s^{\mathrm{Tx}}} v_p(\theta_s^{\mathrm{Tx}}) v_q^*(\theta_s^{\mathrm{Tx}}) \, p(\theta_s^{\mathrm{Tx}}) d\theta_s^{\mathrm{Tx}} \\ \mathrm{R}_s^{\mathrm{Rx}}(n, m)^u &= \int_{\theta_s^{\mathrm{Rx}}} v_n(\theta_s^{\mathrm{Rx}}) \, v_m^*(\theta_s^{\mathrm{Rx}}) p(\theta_s^{\mathrm{Rx}}) d\theta_s^{\mathrm{Rx}} \end{aligned} \tag{2.54}$$

In [43], it is shown that $\mathrm{R}_s^{\mathrm{Tx}}(p, q)^u$ with θ_s^{Tx} uniformly distributed over $[0,2\pi]$ for a ULA can be expressed as

$$\mathrm{R}_s^{\mathrm{Tx}}(p,q)^u = I_0\left(Z_l{}^{\mathrm{Tx}}\right) \tag{2.55}$$

where

$$Z_l{}^{\mathrm{Tx}} = \frac{2\pi(p-q)D_t}{\lambda} \tag{2.56}$$

In [44], it is shown that $\mathrm{R}_s^{\mathrm{Tx}}(p,q)^u$ with θ_s^{Tx} uniformly distributed over $[0,2\pi]$ for a UCA can be expressed as

$$\mathrm{R}_s^{\mathrm{Tx}}(p,q)^u = I_0\left(Z_c{}^{\mathrm{Tx}}\right) \tag{2.57}$$

where

$$Z_c{}^{\mathrm{Tx}} = \sqrt{Z_{1,\mathrm{Tx}}^2 + Z_{2,\mathrm{Tx}}^2} \tag{2.58}$$

and

$$\begin{aligned} Z_{1,\mathrm{Tx}} &= 2\pi\frac{R_t}{\lambda}\left[\cos(\varphi_p) - \cos(\varphi_q)\right] \\ Z_{2,\mathrm{Tx}} &= 2\pi\frac{R_t}{\lambda}\left[\sin(\varphi_p) - \sin(\varphi_q)\right] \end{aligned} \tag{2.59}$$

In [9], it is shown that the real and imaginary parts of receive spatial correlation between the nth and mth antenna element for a ULA with a truncated Laplacian AOA distribution as follows

$$\begin{aligned} \mathrm{Re}\{\mathrm{R}_s^{\mathrm{Rx}}(n,m)^u\} &= I_0\left(Z_l{}^{\mathrm{Rx}}\right) + 4C_l\sum_{k=1}^{\infty} a^2\frac{(1-e^{-a\pi})}{a^2+4k^2} I_{2k}\left(Z_l{}^{\mathrm{Rx}}\right)\cos\left[\left(2k(\theta_r)\right)\right] \\ \mathrm{Im}\{\mathrm{R}_s^{\mathrm{Rx}}(n,m)^u\} &= 4C_l\sum_{k=0}^{\infty} a\frac{(1+e^{-a\pi})}{a^2+(2k+1)^2} I_{2k+1}\left(Z_l{}^{\mathrm{Rx}}\right)\sin[(2k+1)(\theta_r)] \end{aligned} \tag{2.60}$$

where

$$Z_l{}^{\mathrm{Rx}} = \frac{2\pi(n-m)D_r}{\lambda} \tag{2.61}$$

In [44], it is shown that the receive spatial correlation nh and mth antenna element for a UCA with a truncated Laplacian AOA distribution can be expressed as

$$\mathrm{Re}\{\mathrm{R}_s^{\mathrm{Rx}}(n,m)^u\} = I_0\left(Z_c{}^{\mathrm{Rx}}\right) + 4C_l\sum_{k=1}^{\infty} a^2\frac{(1-e^{-a\pi})}{a^2+4k^2} I_{2k}\left(Z_c{}^{\mathrm{Rx}}\right)\cos\left[\left(2k(\theta_r+\alpha^r)\right)\right] \tag{2.62}$$

$$\mathrm{Im}\{\mathrm{R}_{\mathrm{S}}^{\mathrm{Rx}}(n,m)^{u}\} = 4C_l \sum_{k=0}^{\infty} a \frac{(1+e^{-a\pi})}{a^2+(2k+1)^2} I_{2k+1}\left(Z_c{}^{\mathrm{Rx}}\right) \sin[(2k+1)(\theta_r+\alpha^r)]$$

where $Z_c{}^{\mathrm{Rx}}$ is related to the antenna spacing and α^r is the relative angle between the nth and mth antenna element, that are defined as

$$\begin{aligned} Z_c{}^{\mathrm{Rx}} &= \sqrt{Z_{1,\mathrm{Rx}}^2 + Z_{2,\mathrm{Rx}}^2} \\ Z_{1,\mathrm{Rx}} &= 2\pi \frac{R_r}{\lambda}[\cos(\varphi_n) - \cos(\varphi_m)] \\ Z_{2,\mathrm{Rx}} &= 2\pi \frac{R_r}{\lambda}[\sin(\varphi_n) - \sin(\varphi_m)] \\ \sin(\alpha^r) &= \frac{Z_{1,\mathrm{Rx}}}{\sqrt{Z_{1,\mathrm{Rx}}^2 + Z_{2,\mathrm{Rx}}^2}} \\ \cos(\alpha^r) &= \frac{Z_{2,\mathrm{Rx}}}{\sqrt{Z_{1,\mathrm{Rx}}^2 + Z_{2,\mathrm{Rx}}^2}} \end{aligned} \tag{2.63}$$

The SSC channel model utilizes the Kronecker model that was described in Section 2.3.2.1. Thus, the SSC channel model can be represented as

$$\mathbf{H} = \mathbf{R}_{\mathrm{Rx}}^{1/2} \mathbf{H}_{iid}\, \mathbf{R}_{\mathrm{Tx}}^{1/2}$$

where $\mathbf{R}_{\mathrm{Tx}}$ and $\mathbf{R}_{\mathrm{Rx}}$ can be computed as follows

$$\begin{aligned} \mathbf{R}_{\mathrm{Tx}} &= \begin{bmatrix} \mathrm{R}_{\mathrm{S}}^{\mathrm{Tx}}(1,1) & \mathrm{R}_{\mathrm{S}}^{\mathrm{Tx}}(1,2) & \cdots & \mathrm{R}_{\mathrm{S}}^{\mathrm{Tx}}(1,M_t) \\ \mathrm{R}_{\mathrm{S}}^{\mathrm{Tx}}(2,1) & \mathrm{R}_{\mathrm{S}}^{\mathrm{Tx}}(2,2) & \cdots & \mathrm{R}_{\mathrm{S}}^{\mathrm{Tx}}(2,M_t) \\ \vdots & \vdots & \ddots & \vdots \\ \mathrm{R}_{\mathrm{S}}^{\mathrm{Tx}}(M_t,1) & \mathrm{R}_{\mathrm{S}}^{\mathrm{Tx}}(M_t,2) & \cdots & \mathrm{R}_{\mathrm{S}}^{\mathrm{Tx}}(M_t,M_t) \end{bmatrix} \\ \mathbf{R}_{\mathrm{Rx}} &= \begin{bmatrix} \mathrm{R}_{\mathrm{S}}^{\mathrm{Rx}}(1,1) & \mathrm{R}_{\mathrm{S}}^{\mathrm{Rx}}(1,2) & \cdots & \mathrm{R}_{\mathrm{S}}^{\mathrm{Rx}}(1,M_r) \\ \mathrm{R}_{\mathrm{S}}^{\mathrm{Rx}}(2,1) & \mathrm{R}_{\mathrm{S}}^{\mathrm{Rx}}(2,2) & \cdots & \mathrm{R}_{\mathrm{S}}^{\mathrm{Rx}}(2,M_r) \\ \vdots & \vdots & \ddots & \vdots \\ \mathrm{R}_{\mathrm{S}}^{\mathrm{Rx}}(M_r,1) & \mathrm{R}_{\mathrm{S}}^{\mathrm{Rx}}(M_r,2) & \cdots & \mathrm{R}_{\mathrm{S}}^{\mathrm{Rx}}(M_r,M_r) \end{bmatrix} \end{aligned} \tag{2.64}$$

2.4.1 Numerical Results

In this section, the numerical analysis of spatial fading correlation is presented for practical uplink application that is shown in Fig. 2.13. As shown in Fig. 2.13 below, a ULA with four

antenna elements at the transmitter MT and a UCA or a ULA with four antenna elements at the receiver AP are considered.

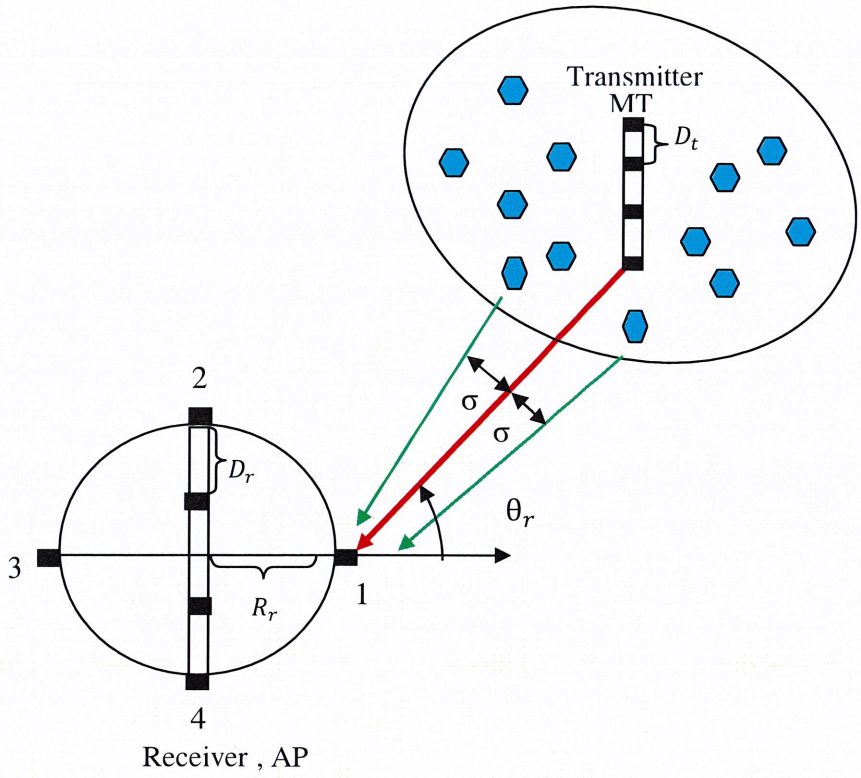


Fig. 2.13 MIMO communication system employing ULA/UCA configurations.

The antenna spacing D_t at the MT is fixed at 0.5λ and the antenna spacing at the AP is varied. Once more, $|R_S(ab,cd)^u|$ is defined as the uplink spatial fading correlation between the link from transmit antenna b to receive antenna a and the link from transmit antenna d to receive antenna c. Both links are assumed to be independent of each other, Hence,

$$|R_S(ab,cd)^u| = \left|R_s^{Tx}(b,d)^u R_s^{Rx}(a,c)^u\right|$$

For example, $|R_S(42,12)^u|$ is the spatial correlation between the link from transmit antenna 2 to receive antenna 4, and the link from transmit antenna 2 to receive antenna 1. Fig. 2.14 presents the spatial fading correlation ($|R_S(21,11)^u|$, $|R_S(43,32)^u|$, $|R_S(33,12)^u|$ and $|R_S(31,11)^u|$) for ULA receiver versus the antenna spacing when θ_r =45° and σ =20°. As it can be seen that the spatial correlation decreases as D_r increases. In addition, as expected $|R_S(31,11)^u|$ gives a lower correlation than $|R_S(21,11)^u|$ for the same parameter D_r. Fig. 2.15 shows the spatial fading correlation ($|R_S(21,11)^u|$, $|R_S(31,41)^u|$, $|R_S(31,21)^u|$,

$|R_S(41,11)^u|$, $|R_S(12,21)^u|$ and $|R_S(32,21)^u|$) for UCA receiver versus the antenna spacing when the θ_r =45° and σ =20°. As expected, the spatial fading correlation decreases as R_r increases. Also, as can be seen that due to the symmetry of the UCA, the fading correlation $|R_S(21,11)^u| = |R_S(31,41)^u|$ and $|R_S(31,21)^u| = |R_S(41,11)^u|$. Furthermore, $|R_S(31,21)^u|$ gives higher correlation than $|R_S(21,11)^u|$. The impact of AS and central AOA on spatial fading correlation of ULA and UCA configurations is illustrated in Fig. 2.16 and Fig. 2.17. To have a fair comparison between the two geometries, aperture size should be made the same (i.e., diameter of UCA = length of ULA). Thus, for ULA spacing D_r=0.5λ, the UCA radius is assumed to be R_r =0.75λ. Fig. 2.16 shows the spatial correlation $|R_S(21,11)^u|$of ULA and UCA configurations versus AS for different AOAs, θ_r ={0°, 45°, 90°}. Whilst Fig. 2.17 shows the spatial correlation $|R_S(21,11)^u|$ of ULA and UCA configurations versus AOA for different AS, σ={3°, 7°, 20°}. From these Figs. it is apparent that the spatial fading correlation decreases as AS increases. In addition, at small AS the spatial correlation is less affected by AOA for both ULA and UCA geometries. Furthermore, it can be seen that for ULA geometry, the maximum correlation can be attained at θ_r =90° (endfire angle), in view of the fact that the antenna elements are inline or parallel with the direction of AOA. The minimum correlation can be achieved when θ_r=0° (broadside angle) in this case the antenna elements are normal to the direction of AOA. Moreover, the UCA experiences the lowest correction at θ_r=45° and the highest at θ_r=0° and θ_r=90°. This is also due to the fact that the correlation along lines perpendicular to the central AOA is lower than along lines parallel to the AOA. As compared to ULA, the UCA experiences lower correlation.

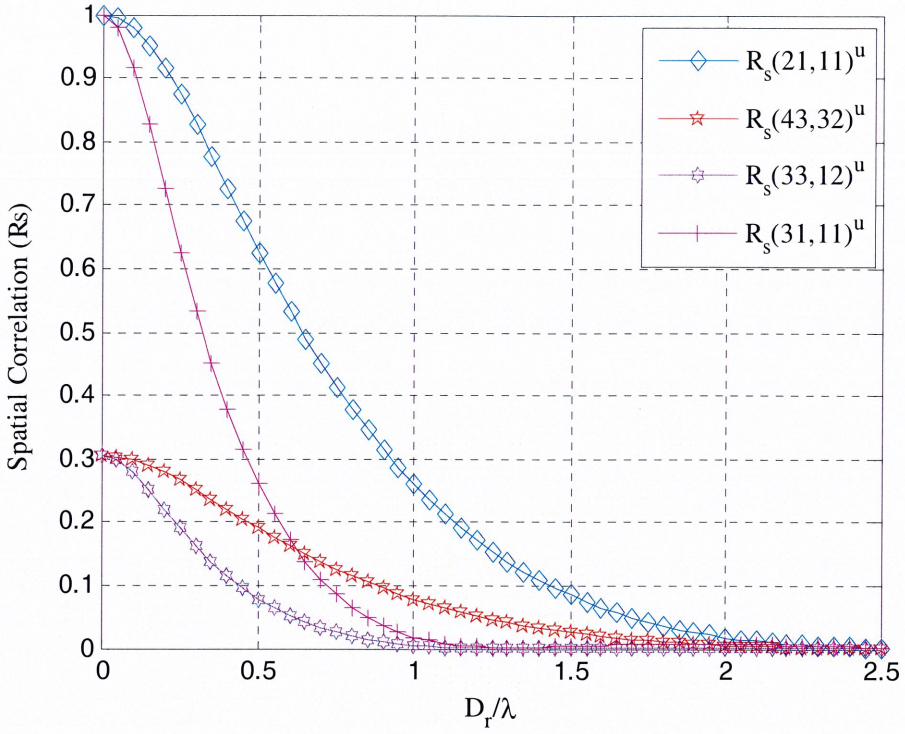


Fig. 2.14 Spatial correlation (Rs) versus antenna spacing for ULA configuration at $\theta_r = 45^o$ and $\sigma = 20^o$.

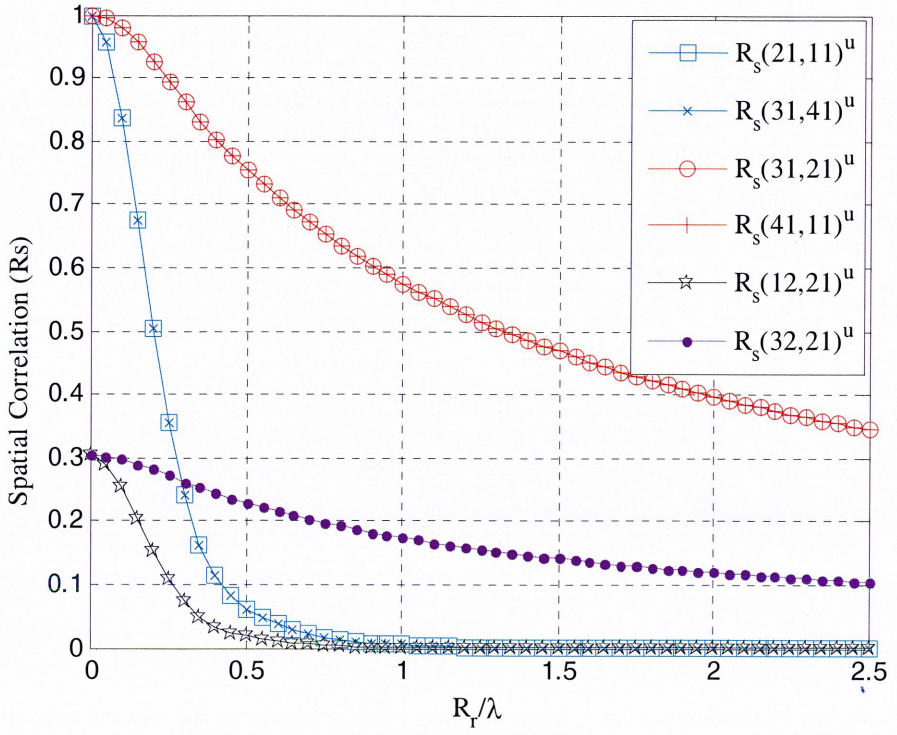


Fig. 2.15 Spatial correlation (Rs) versus antenna spacing for UCA configuration at $\theta_r = 45^o$ and $\sigma = 20^o$.

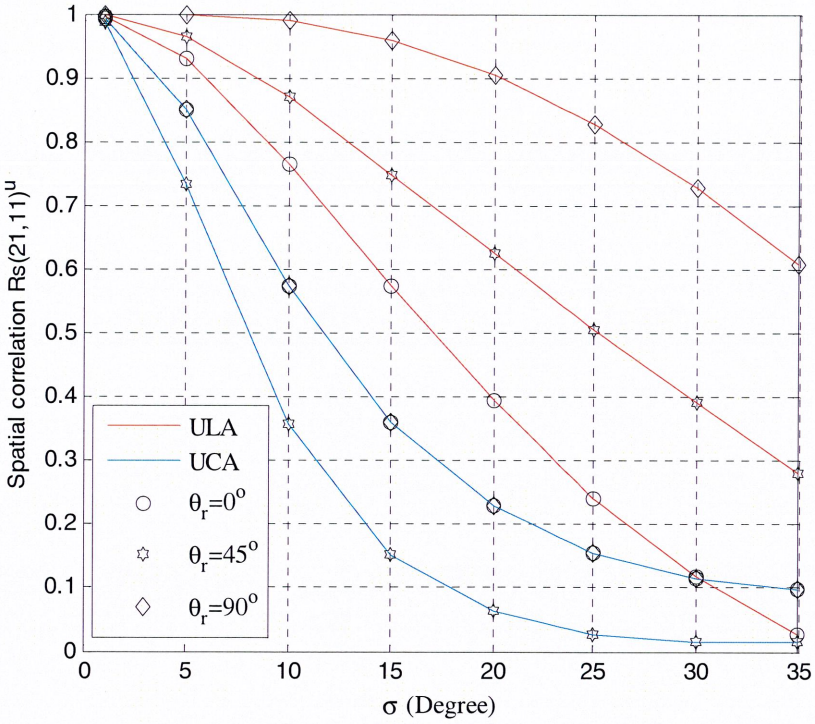


Fig. 2.16 Spatial correlation of ULA and UCA configurations vs. AS (σ) for different AOA, $\theta_r = \{0^o, 45^o, 90^o\}$, $D_r = 0.5\lambda$, and $R_r = 0.75\lambda$.

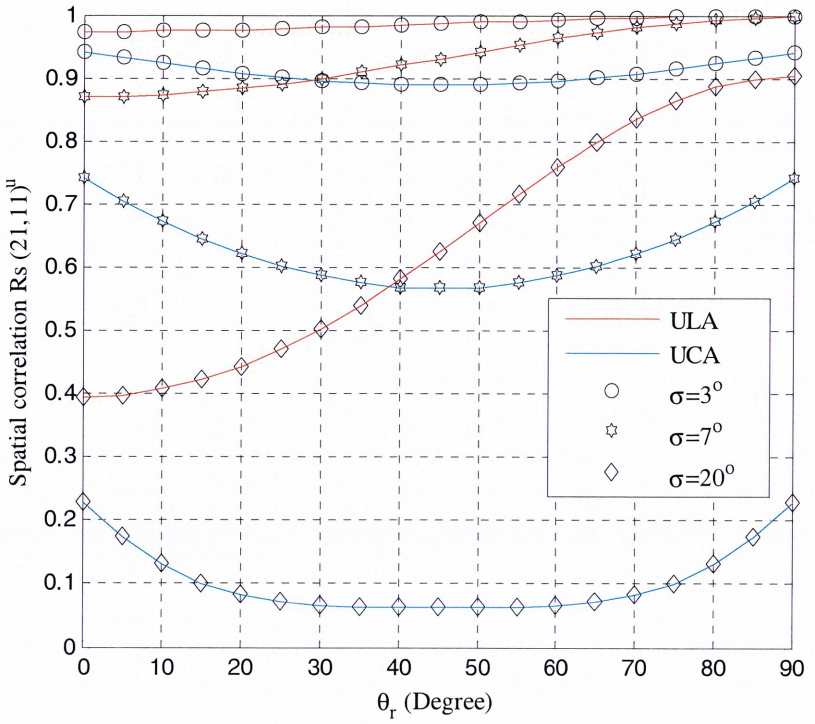


Fig. 2.17 Spatial correlation of ULA and UCA configurations vs. AOA (θ_r) for different AS, $\sigma = \{3^o, 7^o, 20^o\}$, $D_r = 0.5\lambda$, and $R_r = 0.75\lambda$.

2.5 MIMO Channel Capacity

The channel capacity is defined as the maximum possible transmission rate such that the probability of error is arbitrarily small [2]. In this section, the analysis is taken from [16] [1] [3]. The capacity of deterministic MIMO channel is defined as

$$C = \max_{p(\boldsymbol{a})} I(\boldsymbol{a}; \mathbf{y}) \tag{2.65}$$

where $p(\boldsymbol{a})$ is the PDF of the transmit signal vector $\boldsymbol{a}$, and $I(\boldsymbol{a}; \mathbf{y})$ is the mutual information of random vectors $\boldsymbol{a}$ and $\mathbf{y}$. Namely, the channel capacity is the maximum mutual information that can be achieved by varying the PDF of the transmit signal vector. From the fundamental principle of the information theory, the mutual information of the two random vectors, $\boldsymbol{a}$ and $\mathbf{y}$, is given as

$$I(\boldsymbol{a}; \mathbf{y}) = H(\mathbf{y}) - H(\mathbf{y}|\boldsymbol{a}) \tag{2.66}$$

where $H(\mathbf{y})$ is the differential entropy of the vector $\mathbf{y}$, while $H(\mathbf{y}|\boldsymbol{a})$ is the conditional differential entropy of the vector $\mathbf{y}$, given knowledge of the vector $\boldsymbol{a}$. Since the vectors $\boldsymbol{a}$ and $\mathbf{n}$ are statistically independent, $H(\mathbf{y}|\boldsymbol{a}) = H(\mathbf{n})$, (2.66) simplifies to

$$I(\boldsymbol{a}; \mathbf{y}) = H(\mathbf{y}) - H(\mathbf{n}) \tag{2.67}$$

Maximizing the mutual information $I(\boldsymbol{a}; \mathbf{y})$ reduces to maximizing $H(\mathbf{y})$. The autocorrelation function of $\boldsymbol{y}$, $\mathbf{R}_{yy} = E[\mathbf{y}\mathbf{y}^H]$, for narrowband time-invariant wireless channel satisfies [16]

$$\mathbf{R}_{yy} = \frac{\mathrm{E}_a}{M_t}\mathbf{H}\mathbf{R}_{aa}\mathbf{H}^H + \sigma_n^2\mathbf{I}_{M_r} \tag{2.68}$$

where σ_n^2 is the power spectral density of the additive noise $\{\mathrm{n}_i\}_{i=1}^{M_r}$, $\mathbf{I}_{M_r} \in \mathbb{C}^{M_r \times M_r}$ is identity matrix and $\mathbf{R}_{aa} = E[\boldsymbol{a}\boldsymbol{a}^H]$ is the autocorrelation of transmitted signal vector. The differential entropy $H(\mathbf{y})$ is maximized when $\mathbf{y}$ is zero-mean circular symmetric complex Gaussian (ZMCSCG). This implies that $\boldsymbol{a}$ must also be ZMCSCG. Then the differential entropies of vectors $\boldsymbol{y}$ and $\mathbf{n}$ are given by

$$H(\mathbf{y}) = \log_2\left(\det(\pi e\mathbf{R}_{yy})\right) \tag{2.69}$$

$$H(\mathbf{n}) = \log_2\left(\det(\pi e \sigma_n^2 \mathbf{I}_{M_r})\right)$$

where $\det(\cdot)$ is the determinant operation. Thus, the mutual information of (2.67) is expressed as [16]

$$I(\boldsymbol{a};\mathbf{y}) = \log_2 \det\left(\mathbf{I}_{M_r} + \frac{\mathrm{E}_a}{M_t \sigma_n^2}\mathbf{H}\mathbf{R}_{aa}\mathbf{H}^H\right) \tag{2.70}$$

The autocorrelation matrix of $\boldsymbol{a}$ must satisfy $\mathrm{Tr}(\mathbf{R}_{aa}) = M_t$ in order to constrain the total transmitted energy over a symbol period. Hence, from (2.65), the capacity of MIMO channel is given by

$$C = \max_{\mathrm{Tr}(\mathbf{R}_{aa})=M_t} \log_2 \det\left(\mathbf{I}_{M_r} + \frac{\mathrm{E}_a}{M_t \sigma_n^2}\mathbf{H}\mathbf{R}_{aa}\mathbf{H}^H\right), \quad \text{(bps/Hz)} \tag{2.71}$$

where $\mathrm{Tr}(\cdot)$ is a matrix trace operator, defined to be the sum of the diagonal elements and "bps/Hz" is the unit of capacity (bits per seconds per Hertz).

The channel matrix $\mathbf{H}$ is assumed to be perfectly known at the receiver. Channel knowledge at the receiver is maintained via training symbols, this principle will be studied in chapter 5. In the following sub-sections the deterministic channel capacity is derived based on the availability of the channel state information (CSI) at the transmitter.

2.5.1 Uniform Power Allocation Scheme

Without any knowledge of the channel characteristics, the only way to distribute the transmit power is to share it equally on all the M_t transmit antenna elements. Assuming independent transmitted signals, i.e., $\mathbf{R}_{aa} = \mathbf{I}_{M_t}$. Hence, the capacity of MIMO channel in the absence of CSI at the transmitter is given by

$$C_U = \log_2 \det\left(\mathbf{I}_{M_r} + \frac{\mathrm{E}_a}{M_t \sigma_n^2}\mathbf{H}\mathbf{H}^H\right) \tag{2.72}$$

n which $\mathbf{H}\mathbf{H}^H \in \mathbb{C}^{M_r \times M_r}$ is a positive semi-definite Hermitian matrix. The EVD of such a matrix is given by $\mathbf{Q}\boldsymbol{\Lambda}\mathbf{Q}^H$, where $\mathbf{Q} \in \mathbb{C}^{M_r \times M_r}$ is a unitary matrix satisfying $\mathbf{Q}^H\mathbf{Q} = \mathbf{Q}\mathbf{Q}^H = \mathbf{I}_{M_r}$ and $\boldsymbol{\Lambda} \in \mathbb{C}^{M_r \times M_r}$ is a diagonal matrix with its diagonal elements (eigenvalues) given as $\{\lambda_i\}_{i=1}^{M_r}$. Then, the capacity of the MIMO channel is given by

$$C_U = \log_2 \det\left(\mathbf{I}_{M_r} + \frac{\mathrm{E}_a}{M_t \sigma_n^2}\mathbf{Q}\mathbf{\Lambda}\mathbf{Q}^H\right) \tag{2.73}$$

Using the identity $\det(\mathbf{I}_m + \mathbf{AB}) = \det(\mathbf{I}_n + \mathbf{BA})$, where $\mathbf{A}\ \mathbb{C}^{m\times n}$ and $\mathbf{B}\ \mathbb{C}^{n\times m}$, the channel capacity in (2.73) simplifies to

$$C_U = \log_2 \det\left(\mathbf{I}_{M_r} + \frac{\mathrm{E}_a}{M_t \sigma_n^2}\mathbf{\Lambda}\right) \tag{2.74}$$

or equivalently

$$C_U = \sum_{i=1}^{r} \log_2\left(1 + \frac{\mathrm{E}_a}{M_t \sigma_n^2}\lambda_i\right) \tag{2.75}$$

where r denotes the rank of $\mathbf{H}$, that is, $r \leq \min(M_t, M_r)$ and $\min(x)$ represents the minimum value out of the set of parameters x. From (2.75), it can be seen that a MIMO channel is converted into r parallel spatial sub-channels, with equal power allocated to each sub-channel.

2.5.2 Water-Pouring Power Allocation Scheme

Channel knowledge at the transmitter can be maintained via feedback from the receiver or through the reciprocity principle in a duplex system. Here, the model decomposition can be performed as shown in Fig. 2.18.

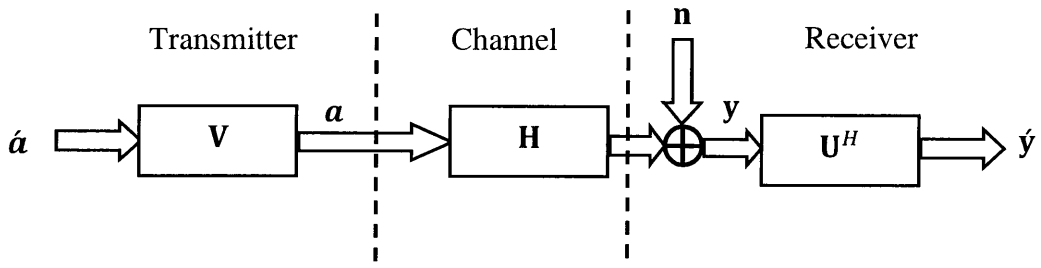


Fig. 2.18 Schematic of model decomposition of **H** when the channel is known to the transmitter and receiver.

In which the transmitted signal is pre-processed with $\mathbf{V}$ in the transmitter (based on the fact that $\mathbf{H} = \mathbf{U}\mathbf{V}^H$ through the singular value decomposition (SVD[1]) and then, a received signal is post-processed with $\mathbf{U}^H$ in the receiver. Referring to the notations in Fig. 2.18, the output signal in the receiver can be written as

$$\acute{\mathbf{y}} = \sqrt{\frac{E_a}{M_t}}\mathbf{U}^H\mathbf{H}\mathbf{V}\acute{\boldsymbol{a}} + \mathbf{U}^H\mathbf{n} = \sqrt{\frac{E_a}{M_t}}\acute{\boldsymbol{a}} + \acute{\mathbf{n}} \tag{2.76}$$

where $\acute{\mathbf{y}} \in \mathbb{C}^{r\times 1}$ is the transformed received signal vector and $\acute{\mathbf{n}} \in \mathbb{C}^{r\times 1}$ is the transformed noise vector with autocorrelation matrix $E[\acute{\mathbf{n}}\acute{\mathbf{n}}^H] = \sigma_n^2\mathbf{I}_r$. The vector $\acute{\boldsymbol{a}} \in \mathbb{C}^{r\times 1}$ must satisfy $E[\acute{\boldsymbol{a}}\acute{\boldsymbol{a}}^H] = M_t$ to constrain the total transmit energy. (2.76) shows that with channel knowledge at the transmitter, $\mathbf{H}$ can be decomposed into r virtual single-transmit, single-receive (SISO) channels satisfying

$$\acute{y}_i = \sqrt{\frac{E_a}{M_t}}\sqrt{\lambda_i}\acute{a}_i + \acute{n}_i, \quad i = 1,2,\dots,r \tag{2.77}$$

This representation can be illustrated Fig. 2.19.

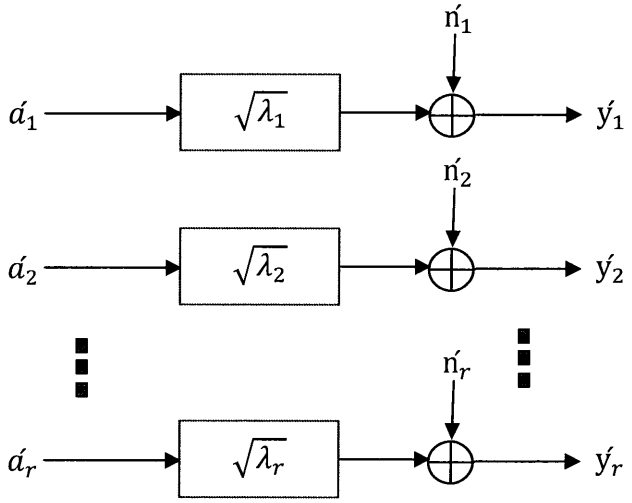


Fig. 2.19 The r virtual SISO channels obtained from the model decomposition.

[1] where $\mathbf{U} \in \mathbb{C}^{M_r\times r}$ and $\mathbf{V} \in \mathbb{C}^{M_t\times r}$ are unitary matrices ($\mathbf{U}^H\mathbf{U} = \mathbf{V}^H\mathbf{V} = \mathbf{I}_r$) and $=$ $\mathrm{diag}\{\sigma_1, \sigma_2, \dots, \sigma_r\}$ with $\sigma_i \geq 0$ and $\sigma_i \geq \sigma_{i+1}$, where σ_i is the ith singular value of the channel and related to the eigenvalue by $(\sigma_i = \sqrt{\lambda_i})$.

If the transmit power for the *i*th transmit antenna is given by $\gamma_i = E[|a_i|^2]$, the capacity of the *i*th virtual SISO channel is

$$C_i(\gamma_i) = \log_2\left(1 + \frac{E_a\gamma_i}{M_t\sigma_n^2}\lambda_i\right), \quad i = 1,2,\dots,r \tag{2.78}$$

Assuming that total available power at the transmitter is limited to

$$E[\boldsymbol{a}^H\boldsymbol{a}] = \sum_{i=1}^{M_t} E[|a_i|^2] = M_t \tag{2.79}$$

The capacity of the MIMO channel is the sum of the individual parallel SISO channel capacities and is given by

$$C_W = \sum_{i=1}^{r} \log_2\left(1 + \frac{E_a\gamma_i}{M_t\sigma_n^2}\lambda_i\right) \quad \text{subject to} \sum_{i=1}^{r}\gamma_i = M_t \tag{2.80}$$

Since, the transmitter can access the spatial sub-channels; it can allocate variable energy across the sub-channels to maximize the mutual information. The mutual information maximization problem becomes

$$C_W = \max_{\Sigma_{i=1}^{r}\gamma_i = M_t} \sum_{i=1}^{r} \log_2\left(1 + \frac{E_a\gamma_i}{M_t\sigma_n^2}\lambda_i\right) \tag{2.81}$$

Using Lagrangian methods, the optimal energy allocation policy, ${\gamma_i}^{opt}$, satisfies

$$\begin{gathered}{\gamma_i}^{opt} = \left(\mu - \frac{M_t\sigma_n^2}{E_a\lambda_i}\right)^+, \quad i = 1,\dots,r \text{ and} \\ \sum_{i=1}^{r}{\gamma_i}^{opt} = M_t\end{gathered} \tag{2.82}$$

where μ is a constant and $(x)^+$ implies

$$(x)^+ = \begin{cases} x, & x \geq 0 \\ 0, & x < 0 \end{cases}$$

The optimal energy allocation is found iteratively through the "water-pouring algorithm" which is described as follows:

Setting the iteration count p to 1 and calculate the constant μ in (2.82)

$$\mu = \frac{M_t}{(r-p+1)}\left[1 + \frac{\sigma_n^2}{\mathrm{E}_a}\sum_{i=1}^{r-p+1}\frac{1}{\lambda_i}\right] \tag{2.83}$$

Using the value of μ found above, the power allocated to the ith sub-channel can be calculated using

$$\gamma_i = \left(\mu - \frac{M_t\sigma_n^2}{\mathrm{E}_a\lambda_i}\right); \quad i = 1,2,\ldots,r-p+1 \tag{2.84}$$

If the power allocated to the channel with the lowest gain is negative, i.e, $\gamma_{r-p+1} < 0$, this channel is discarded by setting $\gamma_{r-p+1}^{opt} = 0$ and rerun the algorithm with the iteration count incremented by 1. The optimal power allocation strategy, therefore, allocates power to those spatial sub-channels that are non-negative. Fig. 2.20 illustrates the water-pouring algorithm. It addresses the fact that more power must be allocated to the sub-channel with higher signal-to-noise ratio (SNR), i.e. SNR= $\frac{E_a}{\sigma_n^2}$.

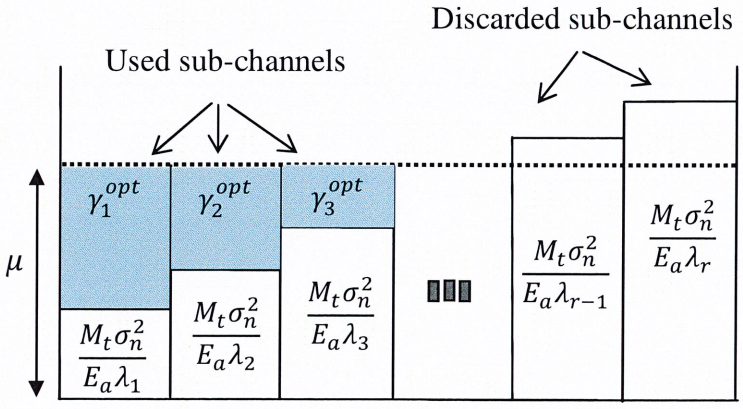


Fig. 2.20 Schematic of water-pouring power allocation algorithm.

Furthermore, if an SNR is below the threshold given in terms of μ, the corresponding sub-channels must be discarded, that is, no power allocated to them.

2.5.3 Ergodic Capacity

Since the channel **H** is random, the information rate associated with the MIMO channel is a random variable. Fig. 2.21 shows the cumulative distribution function (CDF) of the information rate of a flat fading MIMO channel with $M_t = M_r = 2$, obtained through Monte Carlo methods for SNR = 10 dB when uniform power allocation scheme is applied and the sample channels are drawn from $\mathbf{H}_{iid}$. In analyzing the capacity of fading channels two commonly used statistics are the *ergodic* capacity and the *outage* capacity [1], as shown in Fig. 2.21. In this thesis, the channel capacity is analyzed as ergodic process.

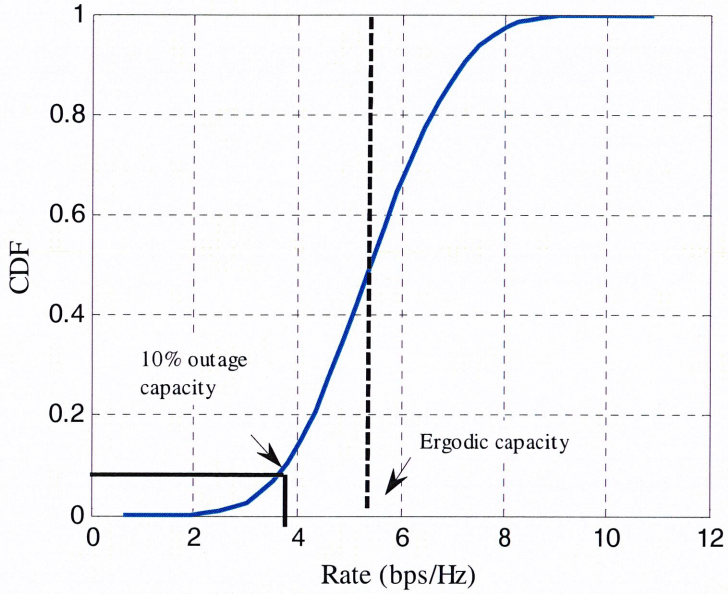


Fig. 2.21 CDF information rate for $\mathbf{H}_{iid}$ MIMO channel with M_t=M_r= 2 and SNR= 10dB.

The ergodic capacity of a MIMO channel is the ensemble average of the information rate over the distribution of the elements of the channel matrix **H**. It is the capacity of the channel when every channel matrix **H** is an independent realization, i.e., it has no relationship to the previous matrix but is typically representative of its class (ergodic). When the CSI is not available at the transmitter, the ergodic capacity is given by

$$\bar{C}_U = E\left[\sum_{i=1}^{r} \log_2\left(1 + \frac{\mathrm{E}_a}{M_t \sigma_n^2}\lambda_i\right)\right] \tag{2.85}$$

The ergodic capacity is the median of the CDF curve as depicted in Fig. 2.21. In this case it is 5.4 bps/Hz. Fig. 2.22 shows the ergodic capacity for various antenna elements ($M_r \times M_t$)

versus SNR. As expected, the ergodic capacity increases with increasing SNR and also with M_t and M_r. However, increasing the number of receiving antennas has a more significant impact on MIMO capacity than increasing the number of transmitting antennas. In addition, it shows the huge capacity increase of MIMO channel over SIMO, MISO and SISO channels. Moreover, at high SNR the capacity increases by 4 bps/Hz for every 3 dB increases for MIMO channel and the capacity increases by 1 bps/Hz of SNR increase for SIMO, MISO or SISO

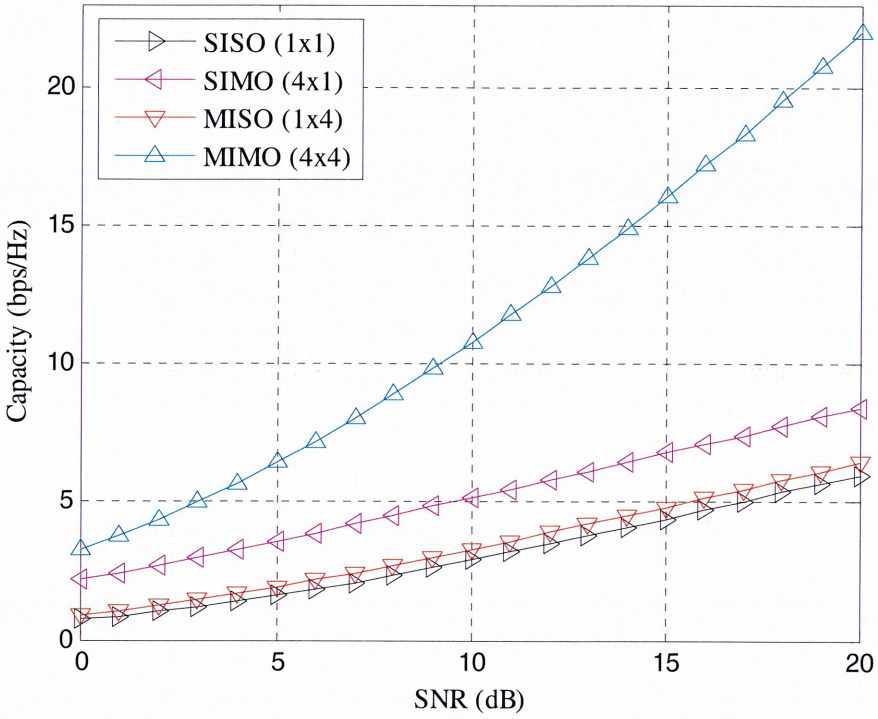


Fig. 2.22 Ergodic capacity for different antenna elements versus SNR.

When CSI is present at the transmitter, the ergodic capacity is defined as the ensemble average of the capacity achieved when water-pouring optimization is performed for each realization of **H**, and is given by

$$\bar{C}_W = E\left[\sum_{i=1}^{r} \log_2\left(1 + \frac{\mathrm{E}_a \gamma_i}{M_t \sigma_n^2} \lambda_i\right)\right] \tag{2.86}$$

Fig. 2.23 compares the ergodic capacity of a MIMO channel with $M_t = M_r = 4$, for the cases that uniform and water-pouring power allocation schemes are applied. As expected, the capacity with water-pouring strategy is always higher than the one with uniform power

allocation scheme. This advantage reduces at higher SNR and is true for MIMO channels with $M_t = M_r = M$. This can be explained as follows:

At high SNR, from (2.71), the capacity of MIMO channel can be approximated as

$$C \approx \max_{\mathrm{Tr}(\mathbf{R}_{aa})=M} \log_2 \det(\mathbf{R}_{aa}) + \log_2 \det\left(\frac{\mathrm{E}_a}{M\sigma_n^2}\mathbf{H}\mathbf{H}^H\right) \tag{2.87}$$

With water-pouring power allocation strategy, $\log_2 \det(\mathbf{R}_{aa})$ is maximized, subject to the constraint $\mathrm{Tr}(\mathbf{R}_{aa}) = M$ when $\mathbf{R}_{aa} = \mathbf{I}_M$, which is also the optimal autocorrelation matrix with the uniform scheme. Therefore, the water-pouring solution will approach the uniform scheme at high SNR.

Fig. 2.24 Compares the ergodic capacity for different number of transmit and receive antennas with uniform and water-pouring power allocation schemes at SNR= 10 dB. It shows that when the number of transmit antennas is lower than the number of receive antennas ($M_t < M_r$) there is almost no gain in the water-pouring power allocation. However, when ($M_t > M_r$) there is a significant potential gain can be achieved by water-pouring power allocation strategy. For eight transmit and four receive antennas ($M_t = 8, M_r = 4$), the gain is about 3.51 bps/Hz and for twelve transmit and four receive antennas ($M_t = 12, M_r = 4$) it is about 5.84 bps/Hz. In addition, when the number of transmit and receive antennas is equal ($M_t = M_r = M$) the capacity gap between water-pouring and uniform ($\bar{C}_{UW}$) increases at higher M (e.g. $M = 4, \bar{C}_{UW} = 0.53$; $M = 8, \bar{C}_{UW} = 1.29$; $M = 12, \bar{C}_{UW} = 2.02$), but will be reduced at high enough SNR as shown in Fig. 2.18.

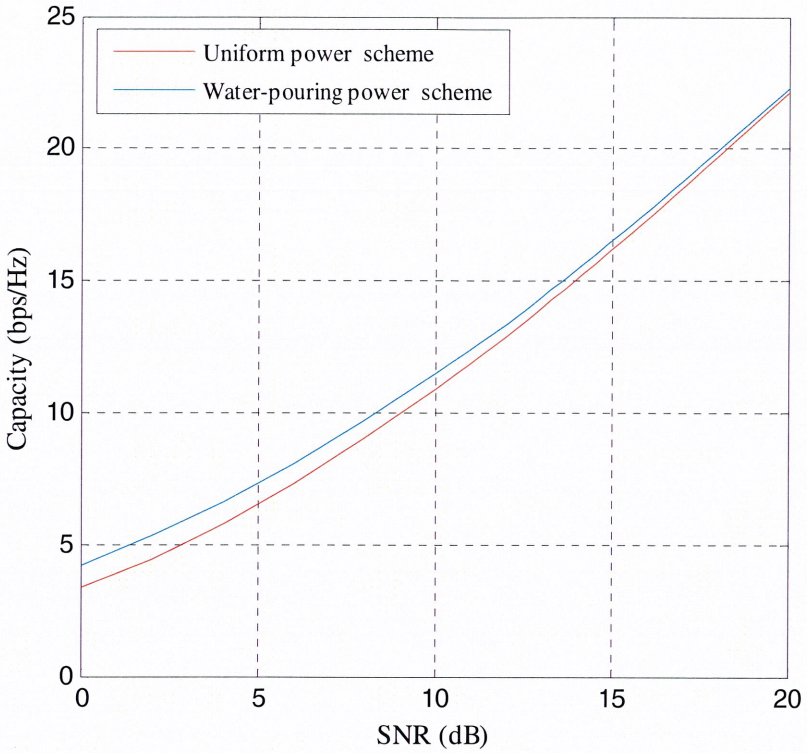


Fig. 2.23 Comparison of ergodic capacity of $M_t = M_r = 4$ MIMO channel with uniform and water-pouring power allocation schemes.

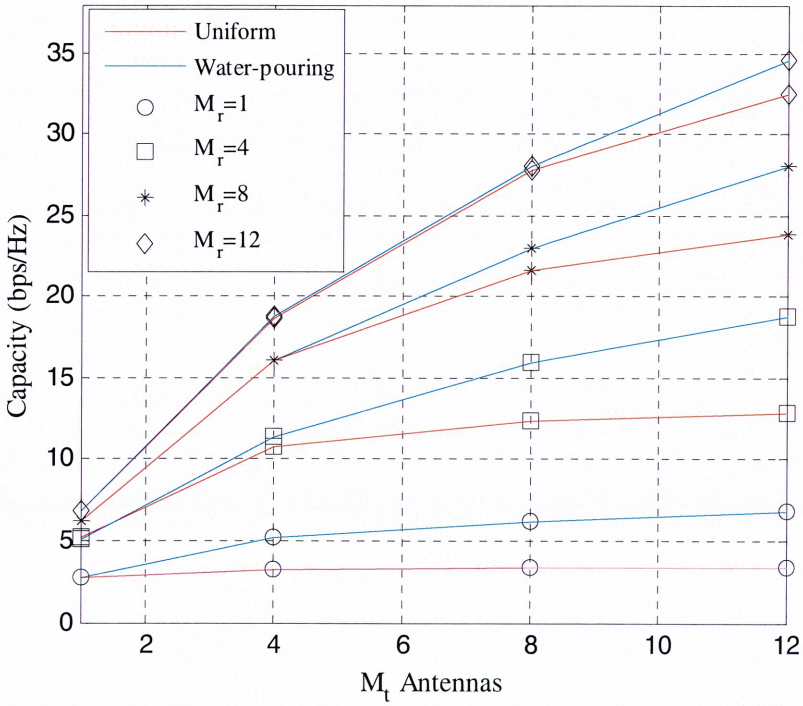


Fig. 2.24 Comparison of ergodic capacity for different number of transmit M_t and receive M_r antennas with uniform and water-pouring power allocation schemes at SNR = 10 dB.

2.6 Conclusion

In this chapter, firstly, the characteristics of multipath channel models for wireless environments are reviewed. Secondly, an overview of the radio propagation and channel models for wireless MIMO systems was presented. MIMO channel models were classified into physical models and analytical models. Physical models focus on the double-directional propagation mechanisms between the location of transmitter and receiver without taking the antenna configuration into account. Analytical models capture physical wave propagation and antenna configuration simultaneously by describing the impulse response (equivalently, the transfer function) between the antenna arrays at both link ends. In addition, a number of channel models proposed in the context of recent wireless standards were summarized. Then, the SSC channel model was presented. An analytical expression for the spatial fading correlation function utilizing the SSC channel model was expressed for ULA and UCA geometries in wireless environment. The channel spatial fading correlation is a function of the angle of arrival, angle spread and distance between elements. The numerical results showed that the spatial fading correlation decreases as antenna spacing and/or angle spread increase. In addition, the correlation along lines perpendicular to the central AOA is lower than along lines parallel to the AOA. Finally, the information-theoretic MIMO channel capacity was presented. The MIMO channel capacity was derived according to the availability of CSI at the transmitter. Without any knowledge of the channel characteristics, the energy is spread equally among all the transmit antennas (i.e., uniform power allocation scheme). However, with the channel knowledge at the transmitter, the capacity can be increased by resorting to the so-called "water-pouring principle", by assigning various levels of energy to various transmitting antennas. This energy is assigned on the basis that the better the channel, the more energy it acquires and vice versa. As well, numerical results were compared between the uniform and water-pouring power allocation schemes. The comparison showed that the water-pouring strategy is an optimal energy allocation algorithm when the number of transmitter antennas is greater than the number of receiver antennas.

Chapter 3

Spatial-Temporal Realistic Clustered Channel Model for Circular Array Based WLAN MIMO Systems

The MIMO technology offers a spatial diversity that can be utilized to achieve significant capacity gain as well as improve system performance [2]. Most of studies for the design and performance evaluation of MIMO wireless communication systems use simplified statistical channel models that are idealized abstractions of temporal and spatial correlation [8] [45]. The main limitation of these channel models is that realistic channel conditions are not included as it provides a simple and intuitive relation to physical directions and propagation environments. Various measurements show that realistic MIMO channels provide different capacity values [46]. Therefore, developing accurate and realistic correlated channels is essential and of crucial importance to predict an accurate performance of real MIMO systems. Some realistic models are proposed as standardized channel models were unified and agreed on by many scientific parties worldwide to be used in the development of modern MIMO systems (refer to Section 2.3.3). These models assume that transmitter and receiver MIMO antennas are restricted to ULA antennas. However, recently there has been increased interest in using UCA antennas [47] [48] [49] [50] [51] [52] [53] [54], which are perhaps the next most common array geometries for future generation access points due to their enhanced azimuth coverage. Therefore, in this chapter, the work in [51] is extended and a more realistic spatially and temporally clustered channel model is developed to be applied in the simulation

of UCA-MIMO systems applying IEEE 802.11*n* standard. The proposed model accounts for six different real propagation scenarios that are applied in IEEE 802.11 TG*n* channel model. Numerical simulations are performed to study the eigenvalues distribution of sub-channels and the effect of LOS component existence. Also, the channel capacity is investigated under various realistic scenarios when varying the transmitted power schemes. As well, the number of antenna elements and the azimuth orientation angle of the employed antenna geometries are studied. This chapter is organized as follows: Section 3.1 presents the TG*n* channel models. Section 3.2 describes the MIMO channel model and presents the modifications to the existing IEEE 802.11*n* channel model to employ UCA configuration. Section 3.3 demonstrates the numerical results and presents a thorough discussion about the applicability of the developed channel model. Finally, Section 3.4 concludes the chapter and summarizes the key findings.

3.1 IEEE 802.11*n* TG*n* Channel Models

In response to growing market demand for higher-performance wireless local area networks (WLANs), the Institute of Electrical and Electronics Engineers- Standards Association (IEEE-SA) approved the creation of the IEEE 802.11 Task Group n (802.11 TG*n*) during the second half of 2003. In Table 3.1, the TG*n* channel model parameters are summarized for both LOS and NLOS conditions.

Table 3.1 IEEE 802.11*n* channel models.

Model	Environment	K (dB) LOS/NLOS	d_{BP} (m)	Delay (ns)	Clusters
A	Flat fading	0/-∞	5	0	1
B	Residential	0/-∞	5	15	2
C	Residential (small office)	0/-∞	5	30	2
D	Typical office	3/-∞	10	50	3
E	Large office	6/-∞	20	100	4
F	Large space (indoor/outdoor)	6/-∞	30	150	6

As depicted in Table 3.1 the TG*n* channel models comprise six models (A to F), which represent a variety of indoor environments, ranging from small environments (A to C), such

as residential homes, with rms delay spreads from 0 to 30 ns, up to larger areas (D to F), such as open spaces and office environments, with rms delay spreads from 50 to 150 ns [55].

For each channel model, if the distance between the transmitter and receiver is less than the breakpoint distance (d_{BP}) then the channel is assumed to have a LOS path otherwise it is a NLOS channel. The LOS Ricean K-factor is applicable only to the first tap while all the other taps K-factor remain at -∞ dB. The LOS component of the first tap is added on top of the NLOS component so that the total energy of the first tap for the LOS channels becomes higher than the value defined in the PDP in Appendix A. According to [11], the AOD and AOA of the LOS component are hard-coded at 45°.

The IEEE 802.11n standard utilizes spatial and temporal clustered (STC) channel model, which involves treating reflection paths as clusters of rays. Each cluster has a PDP (power at different delays, i.e., taps in discrete time), which is used in finding the MIMO channel tap coefficients. This approach was introduced first by Saleh and Valenzuela and later extended by many other researchers (refer to Section 2.3.3).

As depicted in Table 3.1 various numbers of clusters are assigned to the TGn channel models. The models 'B', 'C', 'D', 'E', and 'F' would have 2, 2, 3, 4, and 6 clusters, respectively, while, model 'A' consists of only one tap. The parameters used to model each cluster are the AOD from the transmitter, AOA at the receiver, and AS at both stations. According to [11], the PAS distribution of clusters and corresponding taps is assumed to be truncated Laplacian. The PDP and cluster parameters for the six models are defined in tables in Appendix A.

3.2 Spatial-Temporal Clustered Channel Model

In this section, the spatial-temporal clustered (STC) channel model is introduced. Considering a downlink of IEEE 802.11n MIMO WLAN communication system operating in an indoor environment, where the transmitter is an AP and the receiver is a wireless station (STA). Fig. 3.1 shows ($M_r \times M_t$) MIMO WLAN system with M_t and M_r -elements antenna array at AP and STA, respectively. We consider the arrays at STA and AP to be either ULA with inter-element spacing D_r and D_t or UCA of radius R_r and R_t, respectively. Also, Fig. 3.1 illustrates a graphical representation of the clustered channel model where the angle that each ith element location makes with the horizontal axis is denoted as ϕ_i and φ_i for transmitter and the receiver, respectively. θ_d and θ_r are the AoD and AoA, respectively. Additionally, it is

assumed that the channel is composed of several moving scatterers that are local to STA. Thus, the received signal is the sum of multiple plane waves with random phases. Under this assumption, the channel consists of multiple sample taps, which are associated with different clusters.

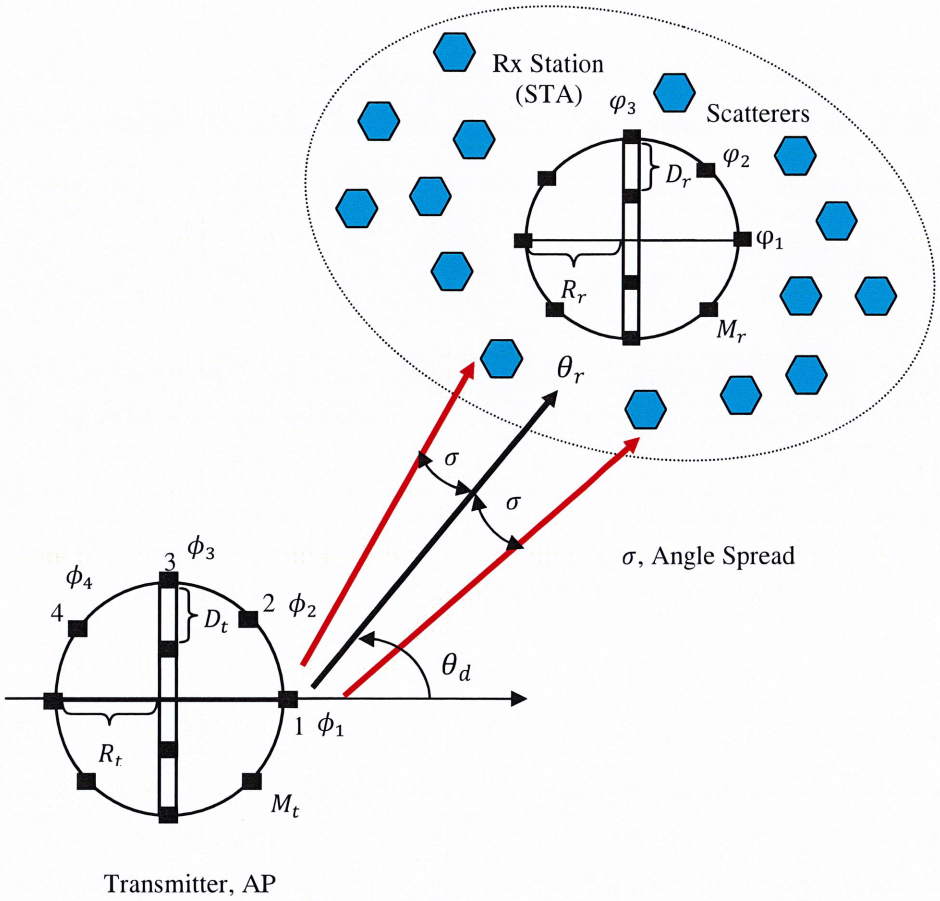


Fig. 3.1 MIMO communication system employing ($M_r \times M_t$) ULA/UCA configurations.

The discrete-time impulse response of MIMO channel matrix can be written as in [55]

$$\mathbf{H}(t) = \sum_{l=1}^{L} \mathbf{H}_l(t)\, \delta(t - \tau_l) \tag{3.1}$$

where t denotes the discrete time index, L is the number of effectively nonzero channel taps (corresponding to the channel clusters), $\mathbf{H}_l(t)$ is the $M_r \times M_t$ channel matrix for the lth tap, $\delta(t - \tau_l)$ is the Kronecker delta function for τ_l delay at lth tap. For simplicity, notation t will be omitted in the following equations. For the TGn channel models in [11] the lth channel tap, matrix $\mathbf{H}_l$, at one instance of time can be written as the sum of a constant LOS matrix and a variable Rayleigh NLOS matrix. Note that the LOS matrix is considered constant in [11],

under the assumption that the transmitter and receiver locations are fixed, and only the surrounding objects are in motion, affecting the NLOS matrix. Thus, the lth channel tap, matrix $\mathbf{H}_l$, can be written as follows:

$$\mathbf{H}_l = \mathbf{H}_l^{LOS} + \mathbf{H}_l^{NLOS} = \sqrt{\mathrm{P}_l}\left(\sqrt{\frac{K_l}{K_l+1}}e^{j2\pi\frac{v_o}{\lambda}t\cos\left(\frac{\pi}{4}\right)}\boldsymbol{S} + \sqrt{\frac{1}{K_l+1}}\mathbf{Ca}\right) \tag{3.2}$$

where:

- P_l is the overall power of channel tap l, it represents the sum of the fixed LOS power and the variable NLOS power of the lth tap, the latter being defined by the model's PDP. This leads to $\mathrm{P}_l = \mathrm{PDP}(l)(1 + K_l)$.
- K_l is the Ricean K-factor represents the relative strength of the LOS component. When $K_l = 0$, (3.2) represents a NLOS channel (the LOS matrix term is eliminated). In this case, the values of $\mathbf{H}_l$ follow a Rayleigh distribution. Otherwise, (3.2) describes a LOS channel, which follows a Ricean distribution. Typical values for the LOS channel models defined in Table 3.1 range from 0 dB to 6 dB. For NLOS channels, $K = -\infty$ dB.
- v_o is the environmental scatterer speed (defined as 1.2 km/h in [11]).
- $\boldsymbol{S}$ is the Rice steering matrix (described in Section 3.2.1).
- $\boldsymbol{C}$ is the spatial correlation-shaping matrix (described in Section 3.2.2).
- $\mathbf{a}$ represents a vector of time-domain obtained by passing independent complex Gaussian random samples through a filter that is shaped based on the Doppler model (described in Section 3.2.3).

3.2.1 Rice Steering Matrix

The Rice steering matrix ($\boldsymbol{S}$) for ULA configurations at both STA and AP ends can be expressed as [56]

$$\boldsymbol{S} = \begin{bmatrix} 1 \\ e^{j2\pi\frac{D_r}{\lambda}\sin(\theta_r)} \\ e^{j2\pi\frac{2D_r}{\lambda}\sin(\theta_r)} \\ \vdots \\ e^{j2\pi\frac{(M_r-1)D_r}{\lambda}\sin(\theta_r)} \end{bmatrix}^T \times \begin{bmatrix} 1 \\ e^{j2\pi\frac{D_t}{\lambda}\sin(\theta_d)} \\ e^{j2\pi\frac{2D_t}{\lambda}\sin(\theta_d)} \\ \vdots \\ e^{j2\pi\frac{(M_t-1)D_t}{\lambda}\sin(\theta_d)} \end{bmatrix} \tag{3.3}$$

In addition, the model is adapted to include UCA configurations as shown in Fig. 3.1. Therefore, in this case the steering matrix can be written as follows:

$$\boldsymbol{S} = \begin{bmatrix} e^{j2\pi\frac{R_r}{\lambda}\cos(\theta_r-\varphi_1)} \\ e^{j2\pi\frac{R_r}{\lambda}\cos(\theta_r-\varphi_2)} \\ \vdots \\ e^{j2\pi\frac{R_r}{\lambda}\cos(\theta_r-\varphi_{M_r})} \end{bmatrix}^T \times \begin{bmatrix} e^{j2\pi\frac{R}{\lambda}\cos(\theta_d-\phi_1)} \\ e^{j2\pi\frac{R}{\lambda}\cos(\theta_d-\phi_2)} \\ \vdots \\ e^{j2\pi\frac{R}{\lambda}\cos(\theta_d-\phi_{M_t})} \end{bmatrix} \tag{3.4}$$

For all TG*n* channel models in [11], the LOS contribution is only applied to the first tap (i.e., delay 0), as the LOS path arrives first, and experiences no reflections. The LOS component is added on top of the NLOS clusters, resulting in a higher overall power than the original NLOS power delay profiles defined in Appendix A. In addition, according to [11], the AOA and AOD for the LOS path of the channel are assumed to be fixed at 45°. Furthermore, the exponential term in (3.2) is due to the phase change introduced in the LOS path, by the channel, due to the movement of scattering objects with velocity v_o.

3.2.2 Antenna Correlation Modelling

The correlation- shaping matrix **C** in (3.2) defines the spatial correlation coefficients, which are generated as follows:

1. First by using the Kronecker model described in Section 2.3.2.1, a spatial correlation matrix is given as

$$\mathbf{R}_H = \mathbf{R}_{\mathrm{Tx}} \otimes \mathbf{R}_{\mathrm{Rx}} \in \mathbb{C}^{M_tM_r \times M_tM_r} \tag{3.5}$$

2. Using $\mathbf{R}_H$ in (3.5), a root-power correlation matrix Γ is given as

$$\boldsymbol{\Gamma} = \begin{cases} \sqrt{\mathbf{R}_H}, & \text{for field type} \\ \mathbf{R}_H, & \text{for complex type} \end{cases}$$

where $\boldsymbol{\Gamma}$ is a non-singular matrix which can be decomposed into a symmetric mapping matrix (or correlation-shaping matrix) with the Cholesky or square-root decomposition as follows:

$$\Gamma = \mathbf{C}\mathbf{C}^T \tag{3.6}$$

Note that $\mathbf{C}$ in (3.6) can be found by Cholesky decomposition or square-root decomposition, depending on whether $\mathbf{R}_{\mathrm{Tx}}$ and $\mathbf{R}_{\mathrm{Rx}}$ are given as the complex matrices or real matrices, respectively [56]. Computing the $\mathbf{R}_{\mathrm{Tx}}$ and $\mathbf{R}_{\mathrm{Rx}}$ correlation matrices for each tap require the PAS distribution and its angular spread, the central AOA and AOD values, and the power of each cluster tap. The TG*n* channel models use the truncated Laplacian PAS distribution, which was found to match closely the angle of arrival statistics within a cluster for urban environments [55]. The $\mathbf{R}_{\mathrm{Tx}}$ and $\mathbf{R}_{\mathrm{Rx}}$ correlation matrices can be determined by using the relationships defined in section 2.4. Thus, for a receiver equipped with ULA antenna configuration, the complex correlation coefficients between *m*th and *n*th antennas can be determined by using (2.60) and (2.61). In addition, a similar expression can be obtained for $\mathbf{R}_{\mathrm{Tx}}$ coefficients as in (2.60) and (2.61) by replacing θ_r, D_r with θ_d, D_t, respectively. Similarly, for a receiver employs UCA antenna configuration, the complex correlation coefficients between *m*-th and *n*-th antennas can be determined by using (2.62) and (2.63). As well, a similar expression can be obtained for $\mathbf{R}_{\mathrm{Tx}}$ coefficients as in (2.62) and (2.63) by replacing θ_r, R_r, φ_m, φ_n with θ_d, R_t, ϕ_m, ϕ_n, respectively.

3.2.3 Temporal Doppler Component

The fading characteristics of indoor wireless channels are different from the outdoor channels. In indoor wireless systems the transmitter and receiver are stationary and objects are moving in between, where the motion of objects occurs at walking speeds approximately 1.2 km/h (0.333 m/s) [11]. The motion results in a change in the reflection paths from transmitting to receiving antennas, which in turn induces change (i.e., gain or fade) in the amplitude of the received signal. This results from the shift in carrier frequency of the signal [55]. The maximum frequency shift is known as Doppler spread f_d and it is defined as:

$$f_d = \frac{v_o}{\lambda} \tag{3.7}$$

where v_o is the speed of object motion and λ is the wavelength defined by $\frac{c}{f_c}$, where c is the light speed (c = 3×10^8 m/s) and f_c is the carrier frequency (f_c = 5.25 GHz or 2.4 GHz). Therefore, the motion results in a frequency shift of 5.83 Hz and 2.67 Hz at f_c = 5.25 GHz and 2.4 GHz, respectively.

Different techniques are used to include the Doppler effect in the channel model. Clark/Gans [16] and Jakes [17] models are the most popular channel models use the fading spectrum in order to produce realistic fading waveforms that have proper time correlation.

Also, Time Domain- Filtered White Gaussian Noise (TD-FWGN) model is widely used. This model is similar to the Clark/Gans model however the Doppler filter is implemented directly in the time domain. The IEEE 802.11n standard utilizes this TD-FWGN model to include the Doppler effect. The fading channel is generated by filtering the complex Gaussian random process with the time domain filter whose frequency response corresponds to the Doppler Spectrum [17]. Fig. 3.2 illustrates an overview of this model.

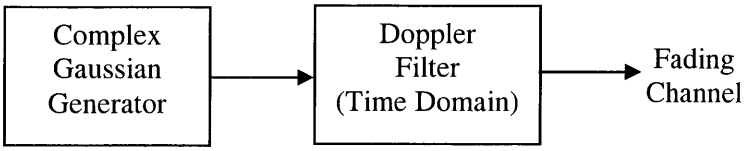


Fig. 3.2 An overview of TD-FWGN model.

As shown in Fig. 3.2 the Doppler filter produces the fading channel. The spectral shape of the Doppler spread determines the time domain fading waveform and dictates the temporal correlation. The Doppler power spectrum $S(f)$ for indoor environments had been defined in order to fit the Doppler power spectrum measurements [11]. Thus, $S(f)$ can be expressed as:

$$S(f) = \frac{1}{1 + A\left(\frac{f}{f_d}\right)^2} \tag{3.8}$$

where A is a constant, defined to set $S(f)$=0.1 at frequency f_d, thus A=9. $S(f)$ is similar to the "Bell" shape spectrum, as shown in Fig. 3.3.

The autocorrelation function (inverse Fourier transform of $S(f)$) is given by

$$R = \frac{\pi f_d}{\sqrt{A}} e^{-\frac{2\pi f_d}{\sqrt{A}}\Delta t} \tag{3.9}$$

and the time period where the channel remains essentially time-invariant is known as coherence time T_c and can be expressed as [11]:

$$T_c = \frac{\sqrt{A}}{2\pi f_d}\ln(2) \tag{3.10}$$

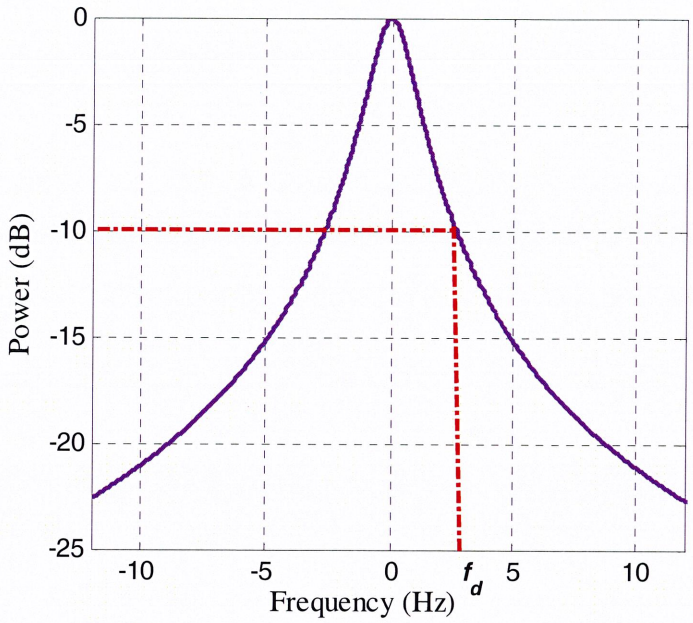


Fig. 3.3 "Bell" shape Doppler power spectrum at f_c =2.4 GHz.

3.3 Numerical Results and Analysis

In this section, the channel capacity of UCA-MIMO WLAN systems is studied and compared using the numerically developed realistic channel model. Unless specified, 4×4 MIMO system, both ends utilize UCA configuration with radius 0.75 wavelength spacing. 10000 channel realizations and NLOS scenario with SNR=10 dB are considered. If ULA configuration is being used then the inter-elements spacing is considered to be 0.5λ. The six standard TG*n* channel model profiles (A-F) defined in [11] are used here to realize realistic scenarios throughout the following simulation study cases.

Fig. 3.4 shows PDF of the AOA for model 'F' and illustrates how the power is distributed among the taps and clusters. The model has 5 overlapping clusters with 18 taps. All taps PDF are considered as truncated Laplacian functions [11].

Fig. 3.5 illustrates the channel spatial correlation R_s (21, 11) between the links h_{11} and h_{21} for all taps of model 'F' versus the UCA radius in the receiver. It is obvious that the spatial correlation decreases as UCA antenna radius increases. In addition, one can see that the

spatial correlation differs for various taps depending on AOA and the angular spread of each tap.

Fig. 3.6 presents the Doppler power spectrum in the bell-shape at carrier frequency = 5.25 GHz. The filter parameters are hard coded, filter order =7 and the normalized Doppler spread = 1/300. The transfer function H(z) of the Doppler filter is given by

$$H(z) = \frac{2.8\times10^{-4}-1.3\times10^{-3}z^{-1}+2.6\times10^{-3}z^{-2}-3\times10^{-3}z^{-3}+2.2\times10^{-3}z^{-4}-9.9\times10^{-4}z^{-5}+2.6\times10^{-4}z^{-6}-2.5\times10^{-5}z^{-7}}{1-5.9z^{-1}+14.8z^{-2}-19.8z^{-3}+15.2z^{-4}-6.4z^{-5}+1.3z^{-6}-0.06z^{-7}}$$

As can be seen that at power =-10 dB, the Doppler frequency f_d= 0.0194*300=5.83 Hz.

Fig. 3.7 illustrates the capacity versus receiver raduis for the TGn channel models for 4x4 UCA-MIMO at SNR=10 dB. As can be seen that model 'A' experiences the lower correlation in view of the fact that it has only one tap, and the maximum capacity can be achived by model 'F', since it has more clusters and 18 taps with wider AS. Furthermore, it can be noticed that as the channel has more clusters with wider AS, a larger capacity can be achieved (refere to Appendix-A).

Fig. 3.8 plots the cumulative distribution function of the eigenvalues of channel models 'A', 'B' and 'F' for 4×4 MIMO UCA based system. It is known that the steeper slope the CDF curve has the less amplitude of the fluctuation in the signal, i.e., the fades due to the multipath are less deep, and therefore a higher degree of diversity is obtained. Fig. 3.8 illustrates the impact of each sub-channel, identified in, upon the total capacity available for different channel models. As can be seen, the largest eigenvalue characteristic (λ_1) is nearly the same for most of the channel models. However, the difference increases between models 'A', 'B' and 'F' is more distinguished for 2nd, 3rd and 4th eigenvalues, respectively. According to (2.75) the higher summation of eigenvalues the higher capacity thus, as shown in the Figure model 'F' has the highest summation of eignvalues that leads to the highest capacity. This result was expected due to the high number of clusters and multi-paths components that are included in model 'F' compared to other models.

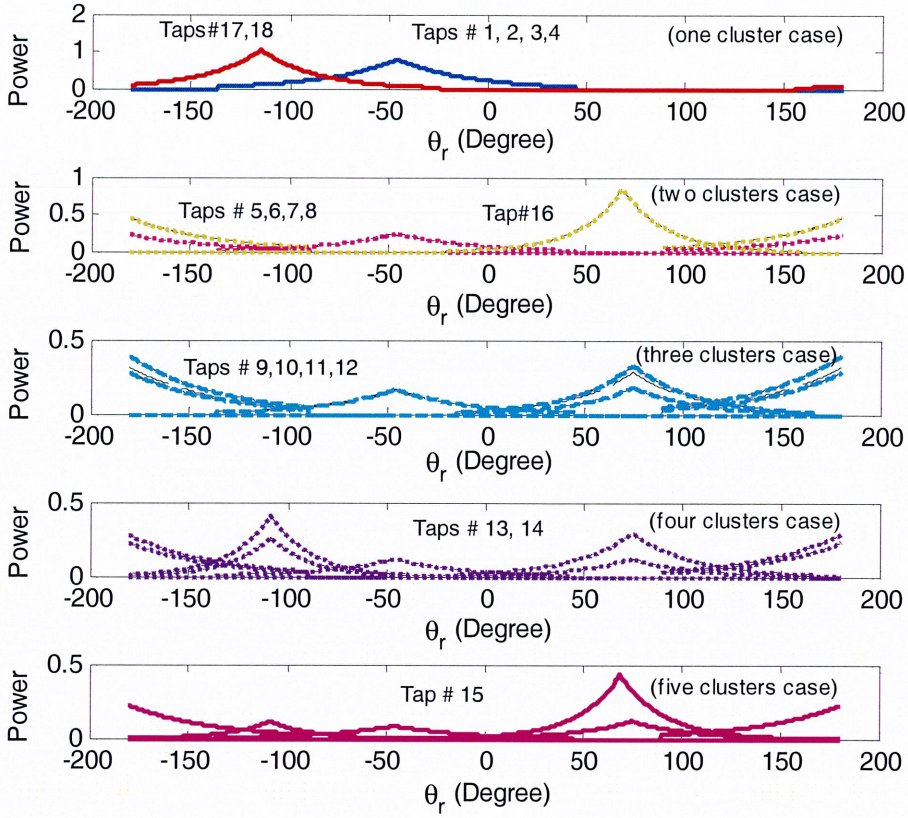


Fig. 3.4 PDF of the AOA for the taps of model 'F'.

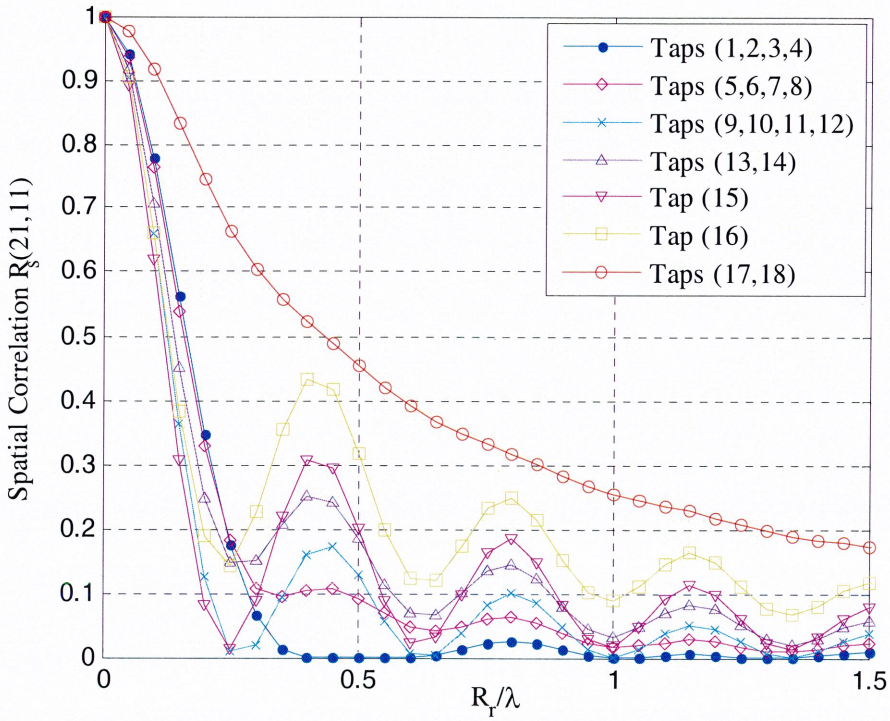


Fig. 3.5 Rs(21,11) for various taps of model 'F' versus UCA radius in the receiver.

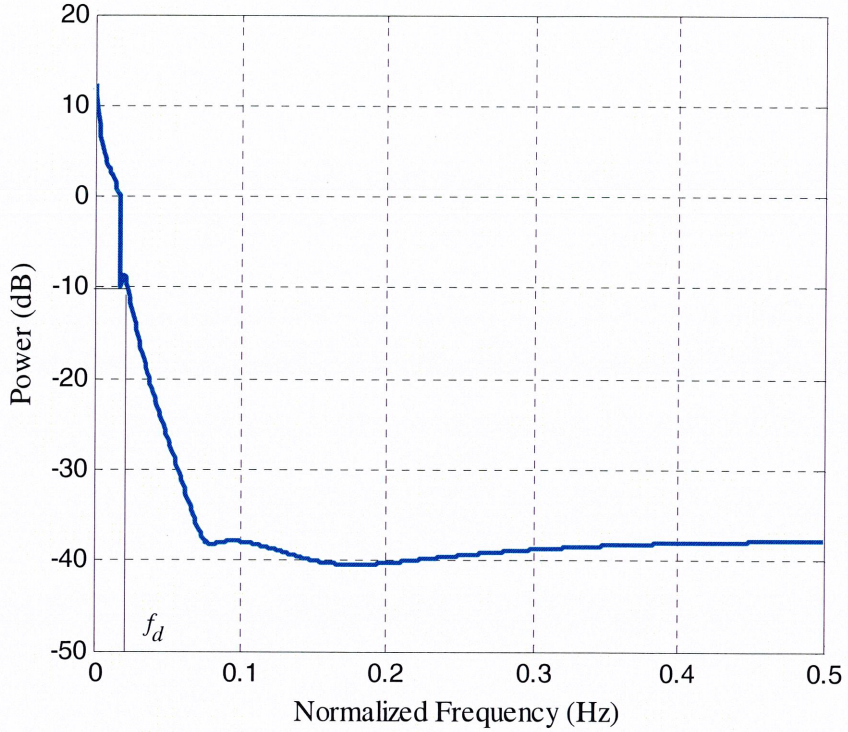


Fig. 3.6 Doppler Spectrum in the bell-shape at f_c =5.25 GHz.

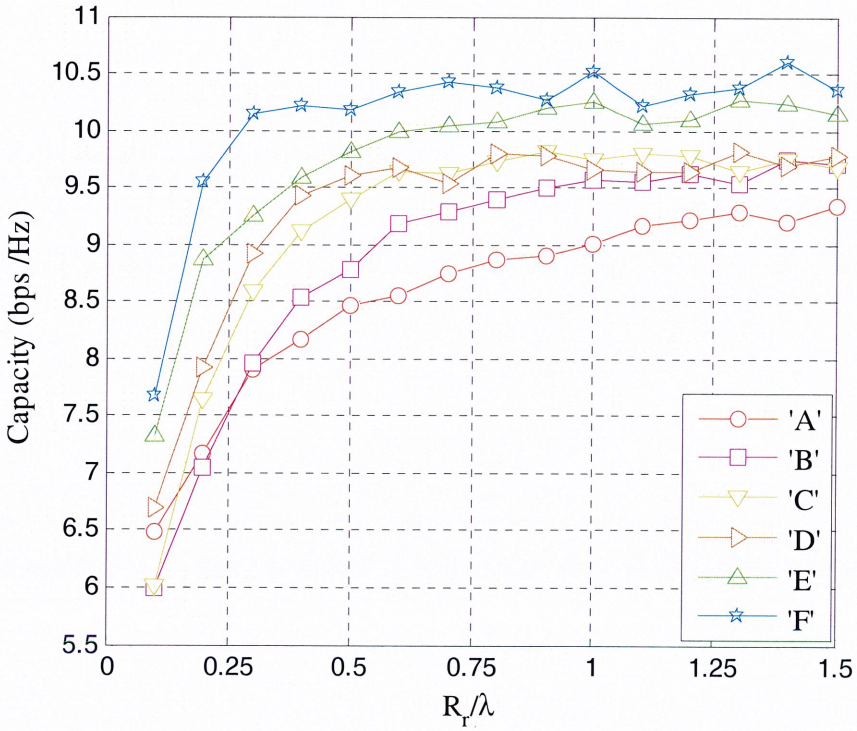


Fig. 3.7 Capacity versus radius for the TG*n* channel models for 4x4 UCA-MIMO and SNR=10 dB.

The capacity dependence on the azimuth rotating of the receiver configuration (orientation of STA) with respect to different channel models is studied. The rotation is measured by the orientation angle (θ_r) shown in Fig. 3.1 with respect to a reference angle φ_1 that is used as a reference for the prescribed AOAs defined by TG*n* models. Two cases are considered: case (1): 4×4 UCA Based system radii R_t, R_r=0.75λ and case (2): 4×4 ULA Based system with inter-element distance D_t, D_r=0.5λ. The results are demonstrated in Fig. 3.9, the presented results reveal that the capacity in general is more affected by the orientation angle in the ULA unlike in the UCA. This effect gives a privilege to the use of UCA receiver. Also, as can be observed that the mean capacity for different models ('A', 'B', and 'F') and configurations (ULA and UCA) is compared to the mean 4x4 (i.i.d) MIMO capacity, capacity for this case is found to be =10.823 bps/Hz. As expected for Model 'A' ULA configuration, since Model 'A' has only one tap one cluster at AOA=45°, then by rotating the ULA by 45° the signal will impinge the array from the endfire direction. In this case the correlation will be highest and the capacity will be minimum. In contrary, if the ULA is rotated by 135° we get the maximum capacity because in this case signal arrives at the broadside of the array. Also it can be observed that the capacity of model 'F' is almost constant and it has the highest values for both configurations. Model 'B' for ULA has the lowest throughput values. In case of UCA the mean capacity is approximately between a minimum of 77% of the mean i.i.d. capacity (for model 'A' at angle 67.5°) and a maximum of 96% of the mean i.i.d. capacity (for model 'F' at angle 67.5°). However, for the ULA case the mean capacity is approximately between a minimum of 62% of the mean i.i.d. capacity (for model 'B' at angle 157.5°) and a maximum of 95% of the mean i.i.d. capacity (for model 'F' at angle 90). Here, it can be concluded that, the variations range of capacity for ULA-MIMO configuration over various orientations and different channel conditions is higher than that for UCA-MIMO configuration under the same orientations and channel conditions.

Fig. 3.10 presents the capacity versus UCA radius for channel models 'A', 'B', and 'F. For each model the capacity is investigated at M_r = 2, 4, and 8. The capacity of model 'F' has the highest value for all cases because of the 18 taps and 6 clusters arriving to the UCA array from different AOAs. One tap, one cluster model 'A' found to be the lower bound for all cases. As can be seen, for 'A', 'B' and 'F' models, the values of mean capacity at $R_r = 0.75\lambda$

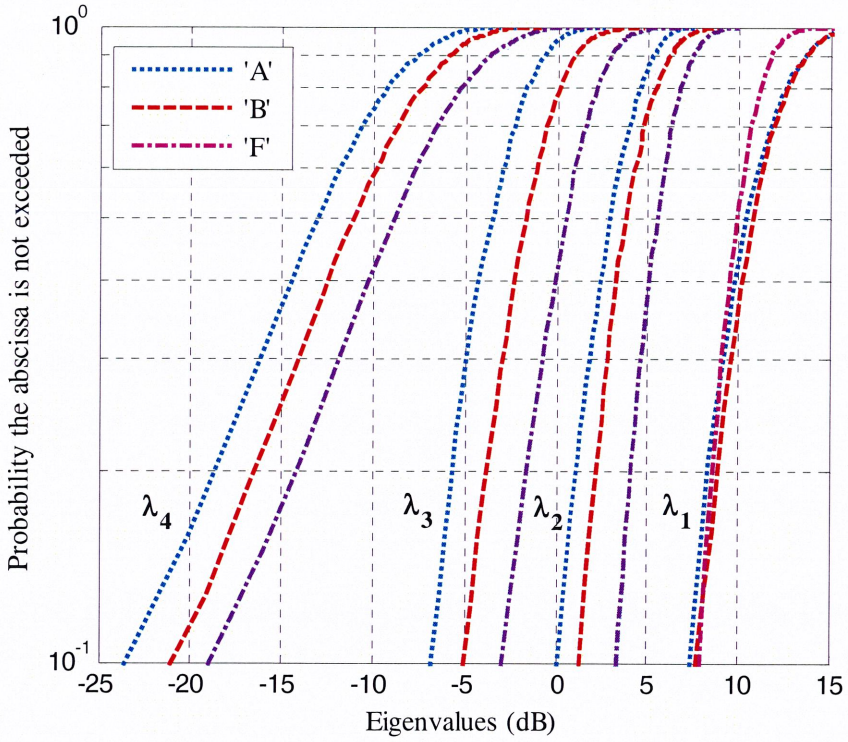


Fig. 3.8 Channel singular values CDFs of models 'A', 'B' and 'F' for 4x4 UCA-MIMO.

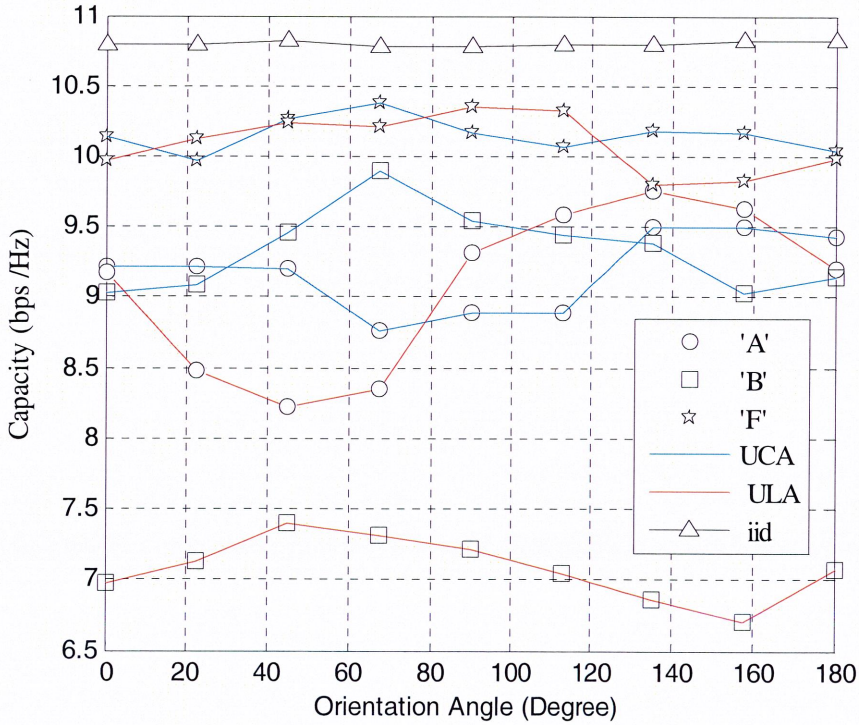


Fig. 3.9 Capacity versus azimuth orientation angle at the receiver side for ULA and UCA configurations and SNR=10 dB.

are respectively 5.5, 5.8 and 6.1 (for $M_r = 2$) and 12.32, 12.98 and 15.12 (for $M_r = 8$). These results show that as M_r increases, the capacity values are more affected by the model selection. This indicates that the environment profiles should be carefully modeled and selected whenever capacity investigations are performed in particular for higher order MIMO.

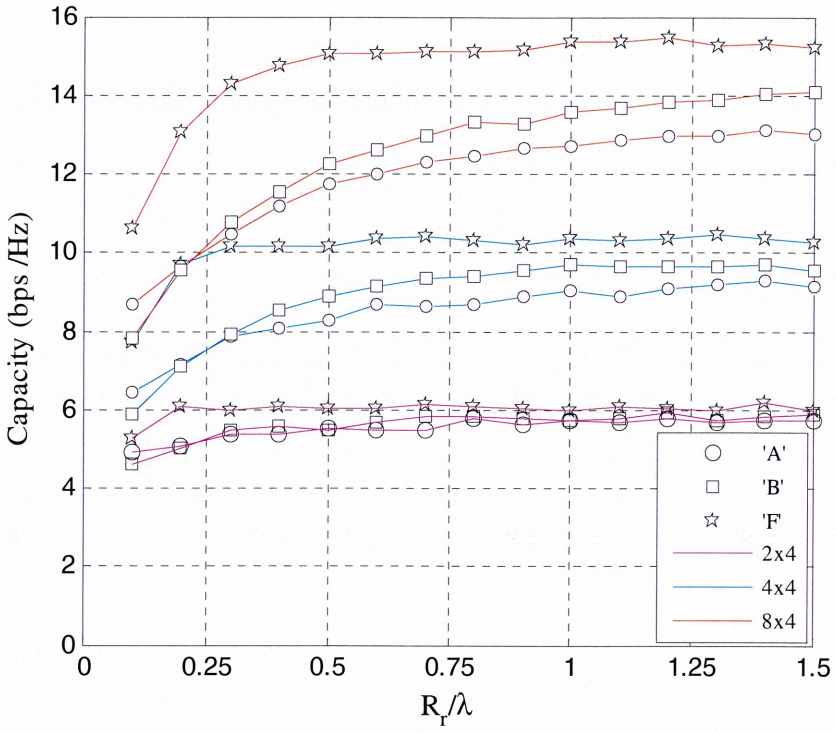


Fig. 3.10 Capacity versus radius of models 'A', 'B' and 'F' for $M_t = 4$ and $M_r = 2,4,8$.

Next, LOS conditions for UCA based MIMO systems are examined by assuming that the LOS component will be included if the separation between the transmitter AP and the receiver STA is within breakpoint distance. The LOS is configured by adding a standard Ricean K-factor reported in [11] to the first tap while all the other taps *K*-factor remain at -∞ dB as in IEEE 802.11*n* model. The LOS component of the first tap is added on top of the NLOS component so that the total energy of the first tap for the LOS channels becomes higher than the value defined in the PDP. Fig. 3.11 shows the capacity CDFs for 4x4 UCA based MIMO under 'A', 'B', and 'F' channel scenarios for both LOS and NLOS cases. As noticed from the figure, the LOS component degrades the capacity of the system working in all channel scenarios. It is found that in NLOS conditions, capacity improves by 20% compared to the case where LOS component included. The improvement is less pronounced for model 'F'

than other models due to its many multipath taps. Therefore, the effect of the 1st LOS tap will be less significant.

Capacity result for UCA based MIMO system applying the water-pouring power allocation scheme under different channel conditions is shown in Fig. 3.12. In water-pouring strategy, the power allocated to each sub-channel is optimized to maximize the system capacity. Fig. 3.12 shows capacity versus SNR for channel models 'A', 'B' and 'F' for 4x4 UCA based MIMO system applying the uniform and water-pouring schemes. For all models the results show that the capacity delivered by water-pouring power allocation scheme is superior to the one achieved with uniform power specifically for low SNRs. In addition, as can be seen that at low SNR (SNR $\leq$ 10 dB) the capacity of the channel models 'A', 'B' and 'F' with water-pouring power allocation scheme is greater than the capacity of the i.i.d channel with uniform power allocation strategy.

The capacity dependence on the use of ULA or UCA geometry at both ends of MIMO system is studied and compared in Fig. 3.13 and Fig. 3.14. Four antenna configuration combinations were considered "ULA, ULA", "ULA, UCA", "UCA, ULA" and "UCA, UCA". For each combination "X, Y", "X" represents the antenna geometry of the transmitter and "Y" refer to the antenna configuration of the receiver. Thus, in downlink, "ULA, UCA" means that the AP transmitter uses a ULA and STA receiver uses a UCA. To have a fair comparison, configurations were assumed to have identical maximum aperture dimension in all examples. Fig. 3.13 and Fig. 3.14 compare channel capacity of the TG*n* models for four different antenna configurations, 4x4 MIMO channel, radius of UCA R=0.75λ and inter-element spacing of ULA D=0.5λ. The result shows that for models 'A', 'D' and 'F' the four antenna configurations experience almost the same capacity. For model 'B' the highest capacity can be achieved by utilizing "UCA, UCA" configuration. For model 'C' the maximum capacity can be attained from "ULA, UCA" and "UCA, UCA" configurations. For model 'E' the highest capacity can be achieved by applying "UCA, ULA" and "UCA, UCA" configurations. From these findings, it can be concluded that for each particular channel profile out of the six environments, there is an optimal configuration that maximizes the channel capacity. In addition, the capacity in models 'B', 'C' and 'E' are affected by the antenna configurations. Whereas, in models 'A', 'D' and 'F' the capacity does not affected by the antenna configurations. Furthermore, it can be seen that the "UCA, UCA" configuration can maximizes the channel capacity in all environments.

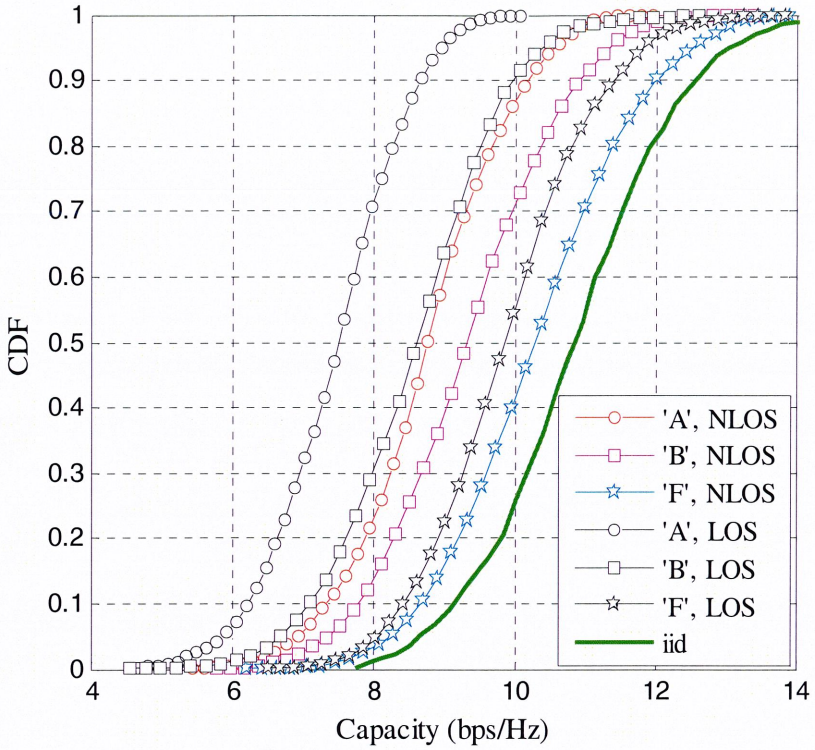


Fig. 3.11 CDFs of capacity for models 'A', 'B' and 'F' for 4x4 UCA-MIMO with LOS and NLOS conditions at SNR= 10 dB.

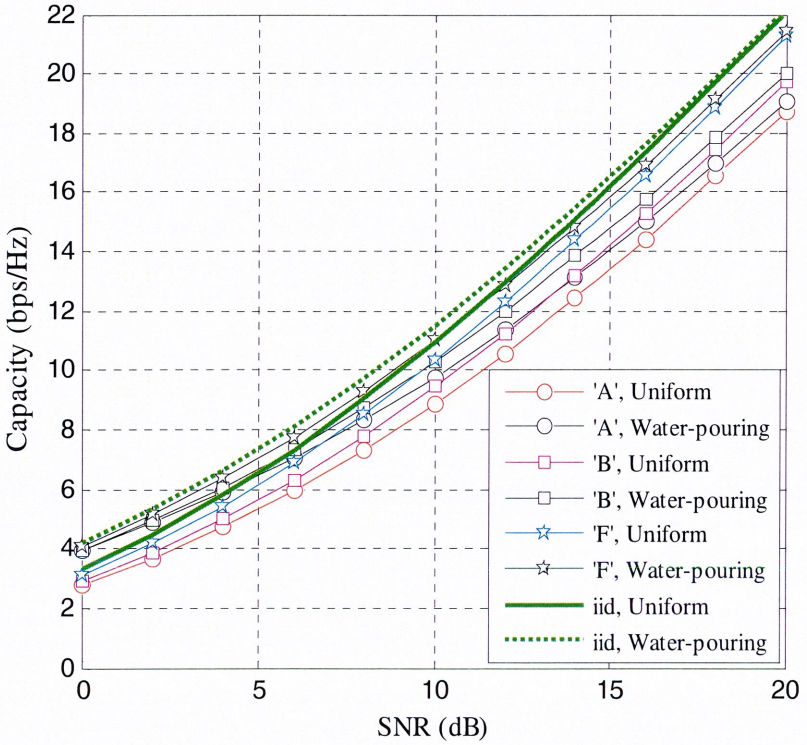


Fig. 3.12 Ergodic capacities of channels 'A', 'B', and 'F' versus SNR, for 4x4 UCA based system with uniform and water-pouring power allocation schemes.

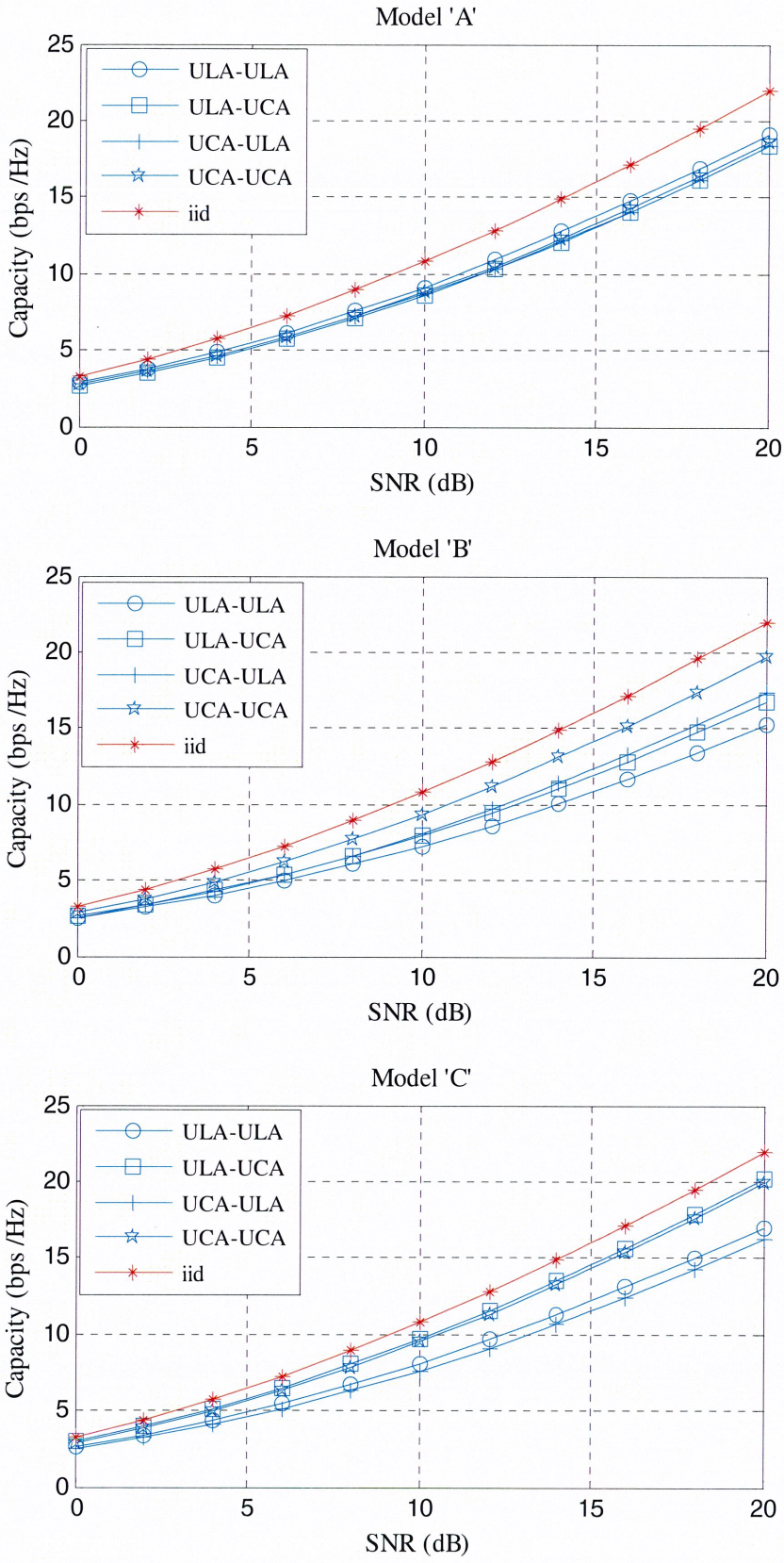


Fig. 3.13 Comparisons of channel capacity for four antenna configurations, for models 'A', 'B' and 'C'.

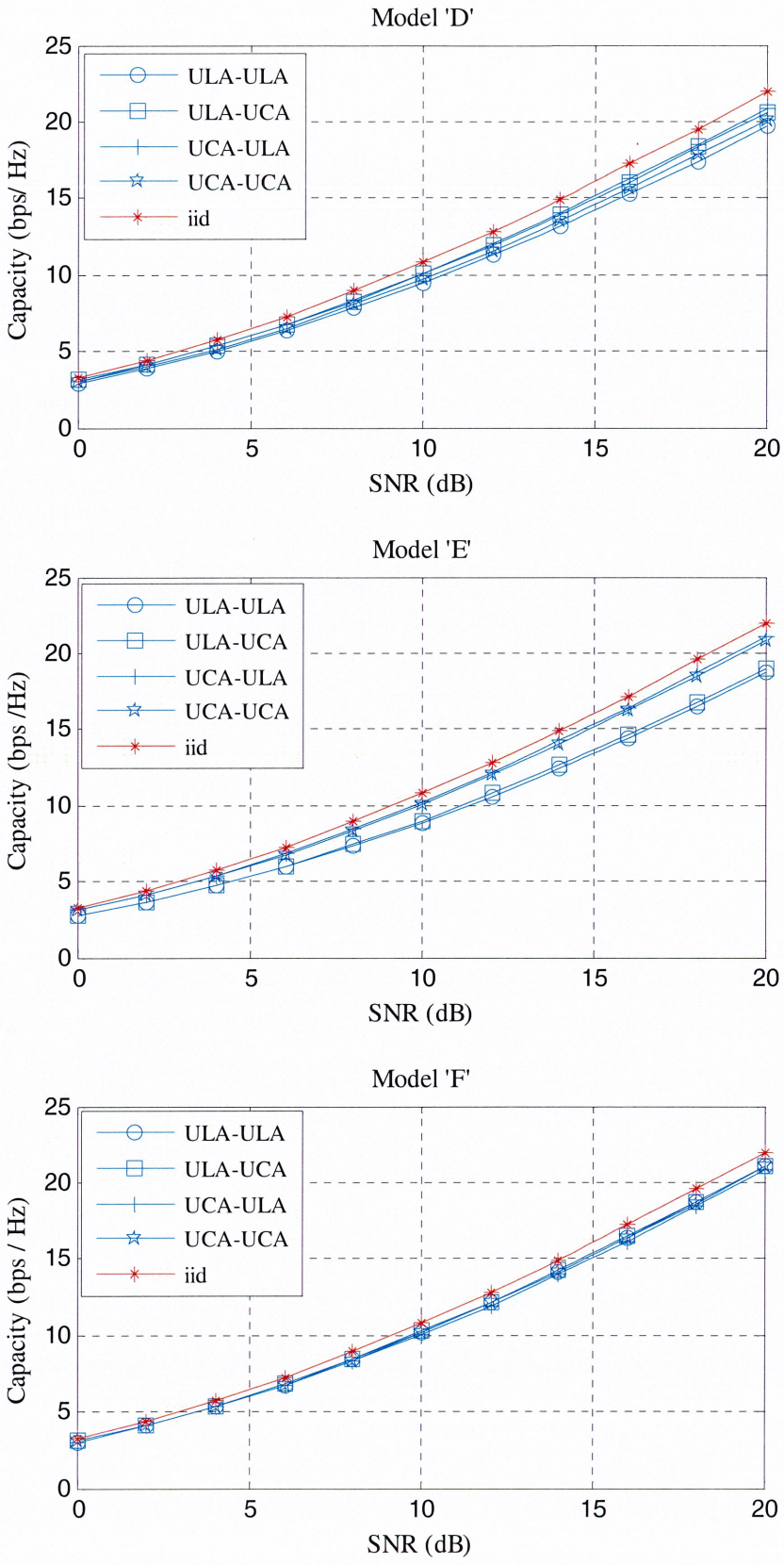


Fig. 3.14 Comparisons of channel capacity for four antenna configurations, for models 'D', 'E' and 'F'.

3.4 Conclusion

In this chapter, a modification to IEEE 802.11*n* standard channel model was proposed to consider the application of using UCA configuration in MIMO WLAN systems. Realistic spatial-temporal clustered channel model was developed and includes spatial fading correlation for six different environment profiles. Each profile is distinguished by its predefined parameters such as number of clusters, number of taps within each cluster, power delay profile of the taps, and angle of incidence of each tap. The impact of the selection of realistic channel profile on the eignvalue of each sub-channel and the total system capacity values were studied. The capacity dependence on the used ULA or UCA geometries and their orientations at both ends of the MIMO system was studied and compared. It has been found that the variations range of capacity for ULA-MIMO configuration over various orientations and different channel conditions is higher than that for UCA-MIMO configuration under the same orientations and channel conditions. The influence of the LOS component on the link performance was presented for UCA based systems and it has been shown that the LOS component existence is not preferable for MIMO systems. Both uniform and water-pouring power allocation schemes have been simulated for UCA based systems and it can be said that capacity of water-pouring power allocation scheme is superior to the one achieved with uniform power specifically for low SNRs. Furthermore, at low SNR the capacity of the TG*n* models with water-pouring power allocation scheme is greater than the one achieved by i.i.d uncorrelated channel with uniform power allocation strategy. In addition, the channel capacity of TG*n* models for various antenna configurations at both ends has been investigated. The results have been shown that for models 'A', 'D' and 'F' the various antenna configurations experience almost the same capacity. For model 'B' the highest capacity can be achieved by utilizing "UCA, UCA" configuration. For model 'C' the maximum capacity can be attained from "ULA, UCA" and "UCA, UCA" configurations. For model 'E' the highest capacity can be achieved by applying "UCA, ULA" and "UCA, UCA" configurations. Therefore, there is an optimal configuration that maximizes the channel capacity. Furthermore, it has been shown that the "UCA, UCA" configuration can maximize the channel capacity in all environments. Finally, the realistic channel model that has been introduced in this chapter could be effectively utilized to provide an accurate capacity for next generation WLANs.

Chapter 4

Effects of Fading Correlation on the Performance of Spatial Multiplexing MIMO Systems

In MIMO communications system very high spectral efficiency can be realized by means of *spatial multiplexing*, where *independent* information streams are transmitted in parallel over different transmit antennas. Bell-Labs Layered Space Time (BLAST) architecture was proposed by Foschini in [6] to take advantage of the promising capacity of MIMO channels. Originally diagonal BLAST (D-BLAST) was recommended with diagonal coding structure. However, it suffers from some technical complexities which make it inappropriate for initial implementation. Thus, a modified version of D-BLAST was then proposed and implemented in real-time in the laboratory known as vertical BLAST (V-BLAST) [57]. The results show that the spectral efficiency reached to 42 bps/Hz using 8 transmitter and 12 receiver antennas in a highly scattering environment. This result is unprecedented and unattainable with the conventional techniques. This high spectral efficiency is enabled by the fact that a scattering environment makes the signal from every individual transmitter appear highly uncorrelated at each receive antennas. As a result, the signal corresponding to every transmitter has a distinct spatial signature at the receiver. These different spatial signatures allow the receiver to effectively decode the data streams radiated from the individual transmit antennas. The reliability is reduced if the signals arriving at the receivers are correlated. Therefore, it is important to investigate the effects of fading correlation on the performance of V-BLAST

system. This chapter covers the basic principles and detection algorithms for V-BLAST. In addition, the impact of channel spatial correlation on the system performance is investigated for both the ULA and UCA geometries. This chapter is organized as follows: Section 4.1 reviews the V-BLAST architecture. Section 4.2 addresses the signal detection techniques for spatially multiplexed MIMO systems including linear signal detection, successive interference cancellation (SIC), parallel interference cancellation (PIC) and maximum likelihood (ML). Section 4.3 presents the numerical results and performance analysis. Section 4.4 concludes the chapter with some remarks.

4.1 V-BLAST Architecture

The V-BLAST block diagram is shown in Fig. 4.1. There are M_t transmit antennas and M_r receive antennas, where $M_r \geq M_t$. The data stream is de multiplexed into M_t sub-streams of equal length. These sub-streams are known as layers. After de multiplexing, these sub-streams are mapped by using M-array phase shift keying (M-PSK) or M-array quadrature amplitude modulation (M-QAM) scheme and modulated sub-streams are simultaneously transmitted over the M_t antennas. The receivers operate co-channel, each receiver antenna receives a superposition of faded signals radiated from all M_t transmit antennas.

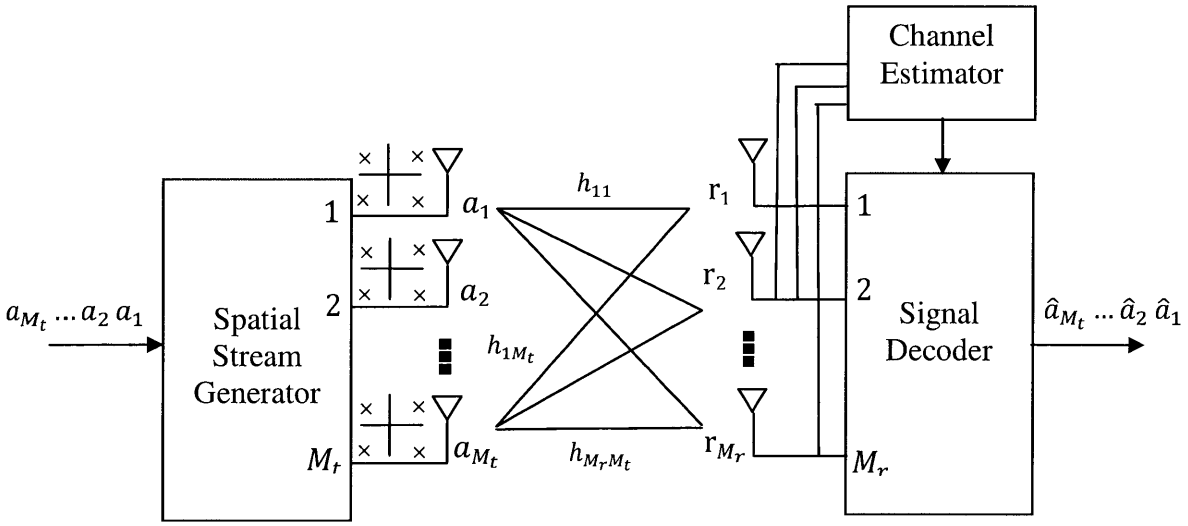


Fig. 4.1 Block diagram of V-BLAST architecture.

The received vector **r**, at instant of time, can be represented as

$$\mathbf{r} = \sqrt{\frac{E_a}{M_t}}\mathbf{H}\boldsymbol{a} + \mathbf{n} = \sqrt{\frac{E_a}{M_t}}\left(\mathbf{H}_1 a_1 + \mathbf{H}_2 a_2 + \cdots + \mathbf{H}_{M_t} a_{M_t}\right) + \mathbf{n} \tag{4.1}$$

where $\mathbf{H}_i$ is the ith column vector of the channel matrix $\mathbf{H}$. Recall, E_a is the total transmitted power, $\boldsymbol{a}$ denotes the vector of the transmitted symbols and $\mathbf{n}$ is the complex Gaussian noise vector with zero mean and variance σ_n^2.

4.2 MIMO Detection Techniques

In this section, the detection techniques for MIMO spatial multiplexing systems, namely, the linear signal detection, successive interference cancellation (SIC), parallel interference cancellation (PIC) and maximum likelihood (ML) are studied.

4.2.1 Linear Signal Detection

Linear signal detection method treats all transmitted signals as interferences except for the desired stream from the target transmit antenna. Therefore, interference signals from other transmit antennas are minimized or nullified. To facilitate the detection of desired signals from each antenna, the effect of the channel is inverted by a weight matrix $\mathbf{W}$ such that [16]

$$\hat{\boldsymbol{a}} = \left[\hat{a}_1\ \hat{a}_2\ \ldots.\ \hat{a}_{M_t}\right]^T = \mathbf{W}\mathbf{r} \tag{4.2}$$

The standard linear detection methods include the zero-forcing (ZF) technique and the minimum mean square error (MMSE) technique.

4.2.1.1 Zero Forcing Signal Detection

The zero-forcing technique nullifies the interference by the following weight matrix [58]

$$\mathbf{W}_{ZF} = \sqrt{\frac{M_t}{E_a}}\mathbf{H}^{\dagger} \tag{4.3}$$

where $\mathbf{H}^{\dagger} = (\mathbf{H}^H\mathbf{H})^{-1}\mathbf{H}^H$ denotes the Moor-Penrose inverse of the channel matrix $\mathbf{H}$. Thus, the result of ZF detector is

$$\hat{\boldsymbol{a}}_{ZF} = \mathbf{W}_{ZF}\mathbf{r} = \boldsymbol{a} + \sqrt{\frac{M_t}{E_a}}\mathbf{H}^{\dagger}\mathbf{n} = \boldsymbol{a} + \tilde{\mathbf{n}}_{ZF} \tag{4.4}$$

which is the transmitted data vector $\boldsymbol{a}$ corrupted by the transformed noise $\tilde{\mathbf{n}}_{ZF}$. This means that the interference caused by the channel $\mathbf{H}$ is completely removed (forced to zero). However, it suffers from the 'noise enhancement' that results from the transformed noise $\tilde{\mathbf{n}}_{ZF} = \sqrt{\frac{M_t}{E_a}}\mathbf{H}^{\dagger}\mathbf{n}$ that is in general larger than $\mathbf{n}$. The transformed noise power can be evaluated as

$$\|\tilde{\mathbf{n}}_{ZF}\|_2^2 = \left\| \sqrt{\frac{M_t}{E_a}} (\mathbf{H}^H\mathbf{H})^{-1}\mathbf{H}^H\mathbf{n} \right\|_2^2 \tag{4.5}$$

Using the SVD in Section 2.5.2, then

$$\|\tilde{\mathbf{n}}_{ZF}\|_2^2 = \left\| \sqrt{\frac{M_t}{E_a}} \mathbf{V}^{-1}\mathbf{U}^H\mathbf{n} \right\|_2^2 \tag{4.6}$$

The expected value of the transformed noise power is given as [16]

$$E\{\|\tilde{\mathbf{n}}_{ZF}\|_2^2\} = E\left\{ \left\| \sqrt{\frac{M_t}{E_a}} \mathbf{V}^{-1}\mathbf{U}^H\mathbf{n} \right\|_2^2 \right\} = \frac{M_t}{E_a}\sigma_n^2 \mathrm{Tr}(^{-2}) = \frac{M_t}{E_a}\sum_{i=1}^{M_t}\frac{\sigma_n^2}{\sigma_i^2} \tag{4.7}$$

4.2.1.2 Minimum Mean Square Error Signal Detection

The noise enhancement effect in the ZF detector can be reduced by using the minimum mean square error (MMSE) detector. The weight matrix of MMSE detector can be written as [58]

$$\mathbf{W}_{MMSE} = \sqrt{\frac{M_t}{E_a}}\left(\mathbf{H}^H\mathbf{H} + \frac{M_t\sigma_n^2}{E_a}\mathbf{I}_{M_t}\right)^{-1}\mathbf{H}^H \tag{4.8}$$

Thus, the result of MMSE detector is

$$\hat{\boldsymbol{a}}_{MMSE} = \mathbf{W}_{MMSE}\mathbf{r} = \tilde{\boldsymbol{a}} + \sqrt{\frac{M_t}{E_a}}\left(\mathbf{H}^H\mathbf{H} + \frac{M_t\sigma_n^2}{E_a}\mathbf{I}_{M_t}\right)^{-1}\mathbf{H}^H\mathbf{n} = \tilde{\boldsymbol{a}} + \tilde{\mathbf{n}}_{MMSE} \tag{4.9}$$

The transformed noise power $\tilde{\mathbf{n}}_{MMSE}$ can be evaluated as

$$\|\tilde{\mathbf{n}}_{MMSE}\|_2^2 = \left\| \sqrt{\frac{M_t}{E_a}}\left(\mathbf{H}^H\mathbf{H} + \frac{M_t\sigma_n^2}{E_a}\mathbf{I}_{M_t}\right)^{-1}\mathbf{H}^H\mathbf{n} \right\|_2^2 \tag{4.10}$$

Using the SVD, transformed noise power can be expressed as

$$\begin{aligned}\|\tilde{\mathbf{n}}_{MMSE}\|_2^2 &= \left\| \sqrt{\frac{M_t}{E_a}} \left(\mathbf{V}^2 \mathbf{V}^H + \frac{M_t \sigma_n^2}{E_a} \mathbf{I}_{M_t} \right)^{-1} \mathbf{V} \mathbf{U}^H \mathbf{n} \right\|_2^2 \\ &= \left\| \sqrt{\frac{M_t}{E_a}} \mathbf{V} \left(+ \frac{M_t \sigma_n^2}{E_a} - 1 \right)^{-1} \mathbf{U}^H \mathbf{n} \right\|_2^2 \end{aligned} \tag{4.11}$$

The expected value of $\|\tilde{\mathbf{n}}_{MMSE}\|_2^2$ is given as [16]

$$\begin{aligned} E\{\|\tilde{\mathbf{n}}_{MMSE}\|_2^2\} &= E\left\{ \left\| \sqrt{\frac{M_t}{E_a}} \mathbf{V} \left(+ \frac{M_t \sigma_n^2}{E_a} - 1 \right)^{-1} \mathbf{U}^H \mathbf{n} \right\|_2^2 \right\} \\ &= \frac{M_t}{E_a} \mathrm{Tr}\left(\sigma_n^2 \left(+ \frac{M_t \sigma_n^2}{E_a} - 1 \right)^{-2} \right) \\ &= \frac{M_t}{E_a} \sum_{i=1}^{M_t} \frac{\sigma_n^2 \sigma_i^2}{\left(\sigma_i^2 + \frac{M_t \sigma_n^2}{E_a} \right)^2} \end{aligned} \tag{4.12}$$

Noise enhancement effect in the linear detectors is significant when the condition number of the channel matrix is large, that is, the minimum singular value is very small. Thus, the noise enhancement effects due to the minimum singular value for the ZF and MMSE linear detectors are respectively given as

$$E\{\|\tilde{\mathbf{n}}_{ZF}\|_2^2\} = \frac{M_t}{E_a} \sum_{i=1}^{M_t} \frac{\sigma_n^2}{\sigma_i^2} \approx \frac{M_t}{E_a} \frac{\sigma_n^2}{\sigma_{\min}^2} \tag{4.13}$$

$$E\{\|\tilde{\mathbf{n}}_{MMSE}\|_2^2\} = \frac{M_t}{E_a} \sum_{i=1}^{M_t} \frac{\sigma_n^2 \sigma_i^2}{\left(\sigma_i^2 + \frac{M_t \sigma_n^2}{E_a} \right)^2} \approx \frac{M_t}{E_a} \frac{\sigma_n^2 \sigma_{\min}^2}{\left(\sigma_{\min}^2 + \frac{M_t \sigma_n^2}{E_a} \right)^2} \tag{4.14}$$

where $\sigma_{\min}^2 = \min\left(\sigma_1^2, \sigma_2^2, \ldots, \sigma_{M_t}^2\right)$. It is clear that the effect of noise enhancement in MMSE detector is less critical than that in ZF detector.

4.2.2 Successive Interference Cancellation Signal Detection

The performance of linear detection methods is worse than that of the other nonlinear receiver techniques. However, they require a low complexity of hardware implementation [16]. The

performance can be improved without significant increasing in the complexity by using the successive interference cancellation (SIC) technique. The SIC algorithm is based on the linear detection technique (ZF or MMSE) combined with symbol cancellation. It first detects the first layer of the signal and then cancels its effect from the overall received signal vector. It then proceeds to the next layer and so on [3]. During the symbol cancellation step, all previous decisions are assumed to be correct. When an incorrect decision is made, interference can be added in, rather than being subtracted out. This results in error propagation into the subsequent layers. To get around this problem the ordered SIC detection algorithm was introduced. In this case, the signal with the strongest signal-to-noise ratio is selected for processing. This improves the quality of the decision and reduces the chances of error propagation. The full Ordered SIC detection algorithm is described in [59] [60] as a recursive procedure, including determination of the optimal ordering, as follows:

Initialization:

$$i = 1 \tag{4.15a}$$

$$\mathbf{W}_1 = \mathbf{H}^+ \tag{4.15b}$$

Recursion:

$$k_i = \underset{j \notin \{k_1 \ldots k_{i-1}\}}{\arg\min} \left\| (\mathbf{W}_i)_j \right\|^2 \tag{4.15c}$$

$$y_{k_i} = (\mathbf{W}_i)_{k_i} \mathbf{r}_i \tag{4.15d}$$

$$\hat{a}_{k_i} = (y_{k_i}) \tag{4.15e}$$

$$\mathbf{r}_{i+1} = \mathbf{r}_i - \hat{a}_{k_i} (\mathbf{H})_{k_i} \tag{4.15f}$$

$$\mathbf{W}_{i+1} = \mathbf{H}^+_{\overline{k_i}} \tag{4.15g}$$

$$i = i + 1 \tag{4.15h}$$

where $\mathbf{H}^+$ denotes the weight matrix of the linear detector (ZF or MMSE), $(\mathbf{W}_i)_j$ is the jth row of $\mathbf{W}_i$, $(.)$ is a quantizer to the nearest constellation point, $(\mathbf{H})_{k_i}$ signifies the k_ith column of $\mathbf{H}$, $\mathbf{H}_{\overline{k_i}}$ represents the matrix obtained by zeroing the k_i-th column of $\mathbf{H}$, and $\mathbf{H}^+_{\overline{k_i}}$ is the weight matrix of $\mathbf{H}_{\overline{k_i}}$. In the above algorithm, (4.15c) determines the optimal ordering of the layer to be detected; (4.15d) performs *nulling* and computes the decision statistic; (4.15e) slices computed decision statistic and yields the decision; (4.15f) performs *cancellation* by decision feedback, and (4.15g) computes the new weight matrix for the next iteration. The entire ordered SIC scheme is demonstrated in Fig. 4.2.

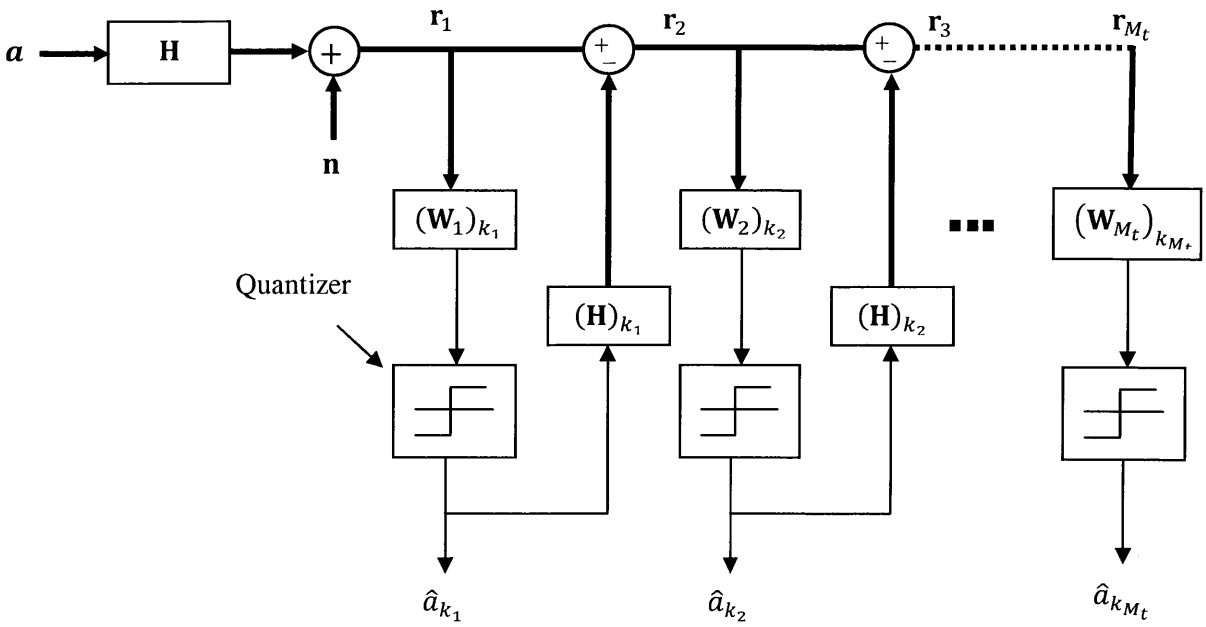


Fig. 4.2 Ordered SIC signal detection diagram.

There are several disadvantages with the SIC scheme. It needs for power reordering at each stage of detection, and the number of stages required increases linearly with the number of transmit antennas. Hence, long system delays can also be expected when the number of stages is large.

4.2.3 Parallel Interference Cancellation Signal Detection

The parallel interference cancellation (PIC) detection scheme was proposed in [61] [62], this method does not require power reordering and helps reduce the system delay at the cost of higher computational complexity. The parallel detector consists of two or more stages, as opposed to the sequential detector which consists of as many stages as the number of symbols to be detected. The entire parallel detection technique is illustrated in Fig. 4.3. The first stage gives a rough estimate of the symbols and the second stage refines this estimate. The output can also be further iterated to improve the performance. The first stage could be either ZF or MMSE; the output of the first stage detection can be written as [61]

$$\tilde{\boldsymbol{a}} = (\mathbf{H}^{+}\mathbf{r}) \tag{4.16a}$$

Next, M_t auxiliary symbol vectors are constructed from $\tilde{\boldsymbol{a}}$ such that in each vector a symbol is nulled out. This can be expressed as

$$\tilde{\boldsymbol{a}}_k = \boldsymbol{J}_k \tilde{\boldsymbol{a}}, \quad k = 1, \ldots, M_t \tag{4.16b}$$

where $\boldsymbol{J}_k$ is the identity matrix with the k-th element set to zero. Then, M_t auxiliary receive vectors are formed from the auxiliary symbol vectors by

$$\tilde{\mathbf{r}}_k = \mathbf{r} - \mathbf{H}\tilde{\boldsymbol{a}}_k, \quad k = 1, \ldots, M_t \tag{4.16c}$$

Finally, the transmitted symbols can be estimated using the weight vector of the appropriate column of the channel matrix

$$\hat{a}_k = (\mathbf{H}^+{}_k \tilde{\mathbf{r}}_k), \quad k = 1, \ldots, M_t \tag{4.16d}$$

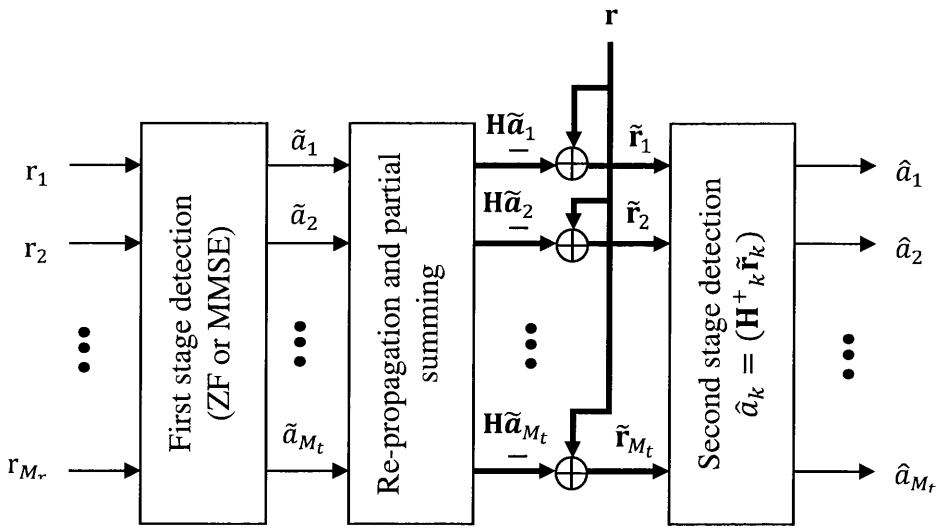


Fig. 4.3 PIC signal detection diagram.

Numerical examples are presented in Appendix B, which demonstrate the algorithms of ordered SIC and PIC detection techniques.

4.2.4 Maximum Likelihood Signal Detection

The Maximum likelihood (ML) detector calculates the Euclidean distance between the received signal vector and the product of all possible transmitted signal vectors with the given channel **H**, and finds the one with the minimum distance [16]. The ML detector is given by [58]

$$\hat{a} = \arg\min_{\boldsymbol{a}\in s} \left\| \mathbf{r} - \sqrt{\frac{E_a}{M_t}}\mathbf{H}\boldsymbol{a} \right\|^2 \tag{4.17}$$

where $s = A^{M_t}$ denotes the set of all possible transmitted data vector $\boldsymbol{a}$. The ML method achieves the optimal performance in the sense of minimizing the error probability. However, its complexity increases exponentially as modulation order and/or the number of transmit antennas increases.

4.3 Numerical Results

In this section, the performance of the aforementioned detection techniques is investigated. Firstly, a comparison between these techniques is presented with the uncorrelated channel $\boldsymbol{H}_{iid}$. Secondly, the effects of spatial fading correlation on the performance of ordered SIC-MMSE are studied utilizing the SSC channel model presented in Section 2.3. These effects are studied for a 4x4 MIMO channel employing ULA with inter-element spacing of D_t=0.5λ at the transmitter and ULA with inter-element spacing of D_r=0.5λ or UCA with circular radius R_r =1.5D_r at the receiver. Finally, the performance of the ordered SIC-MMSE is also presented with the developed STC channel model. Without loss of generality, the numerical studies are performed for 4x4 MIMO channel, the V-BLAST system is simulated with Quadrature Phase-Shift Keying (QPSK) modulation technique, and 125000 channel realizations. In this numerical analysis, the fading channel characteristics are assumed to be known perfectly at the receiver.

The performance of linear (ZF and MMSE), SIC and ML detectors versus SNR is shown in Fig. 4.4. As can be seen that the performance achieved by the SIC techniques is better than that of the linear detectors. In addition, it shows that the ordering of layers improves performance considerably in view of the fact that the ordered algorithm detects the strongest signal first. As a result, the strongest interference is cancelled first. On average, this leads to improved BER performance in the sequentially detected layers. The figure shows that the ordered scheme (OSIC) obtains a performance gain compared with of unordered (USIC) scheme for both ZF and MMSE nulling techniques. Besides, the performance of MMSE nulling criteria outperforms ZF. Since, the MMSE utilizes the knowledge of the signal to

noise ratio to improve performance. Moreover, it is obvious that the ML is an optimum detection technique and it outperforms the OSIC-MMSE scheme.

Fig. 4.5 compares the BER performance of the linear (ZF and MMSE), PIC and ML detectors. As can be seen that the performance of PIC detector is better than linear detector for the same nulling criteria. In addition, it shows that the MMSE nulling criteria for both detection techniques outperforms the ZF. Furthermore, it presents the optimum performance that can be achieved by the ML detector.

Fig. 4.6 compares the performance of the SIC technique with the PIC detector. It can be observed that for SNR≥10 dB, the PIC-ZF and PIC-MMSE detectors achieve similar performance to USIC-ZF and USIC-MMSE schemes, respectively. Also, as can be noticed that for SNR<10 dB, the performance of the PIC-ZF detector is slightly better than OSIC-ZF scheme. Moreover, it shows that the best suboptimal performance can be obtained by the OSIC-MMSE.

Fig. 4.7 shows the diversity gain[1] that results from increasing the number of receiver antennas for OSIC-MMSE detection, M_t=2 and M_r={2,3,4}. As can be seen that as number of receiver antennas (M_r) increases the reliability of the system is improved. The increase in the slope of the bit-error-rate corresponds to the diversity gain in the system.

Fig. 4.8 shows the performance of the ULA and UCA receiver as a function of AOA (θ_r) for various SNR, SNR= {0, 10, 20} dB, and angular spread, σ =20°. Also, the performance of uncorrelated $\mathbf{H}_{iid}$ 'iid' is presented for comparison. It can be seen that at low SNR the channel spatial fading correlation has a less effect on the reliability of the system. In turn, at moderate and high SNR the spatial correlation reduces the BER performance. As seen at θ_r=90°, the ULA receiver obtains 7 dB and 15 dB, UCA receiver attains 2 dB and 5 dB performance loss compared with uncorrelated channel at SNR=10 dB and SNR=20 dB, respectively. Moreover, the presented result reveals that the system performance in general is more affected by the correlation in the ULA unlike the UCA.

[1] **Diversity gain:** Improvement in the link reliability obtained by transmitting the same data on independently fading branches.

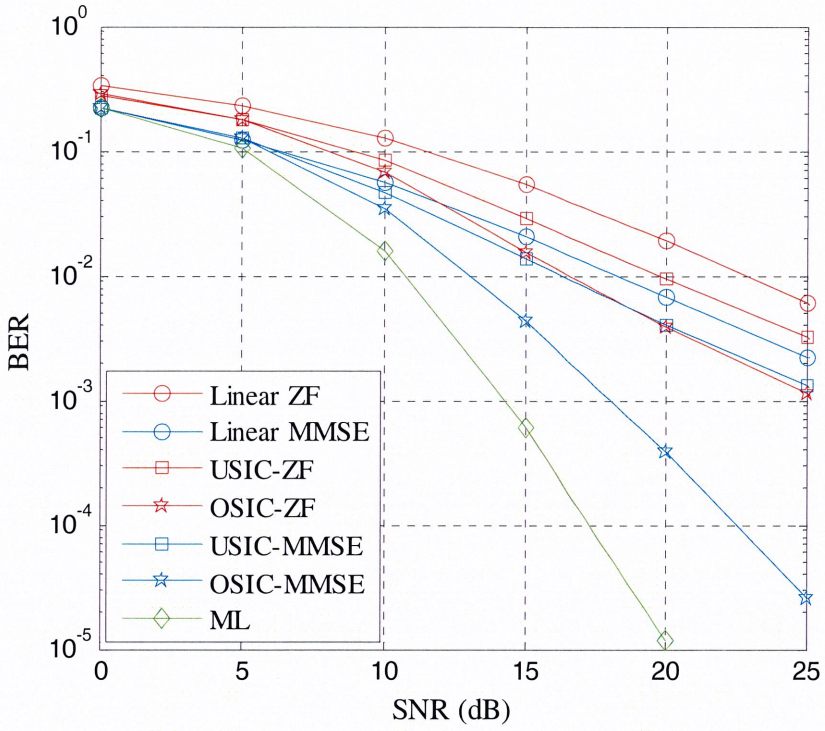


Fig. 4.4 BER performance of SIC detector versus SNR with uncorrelated channel.

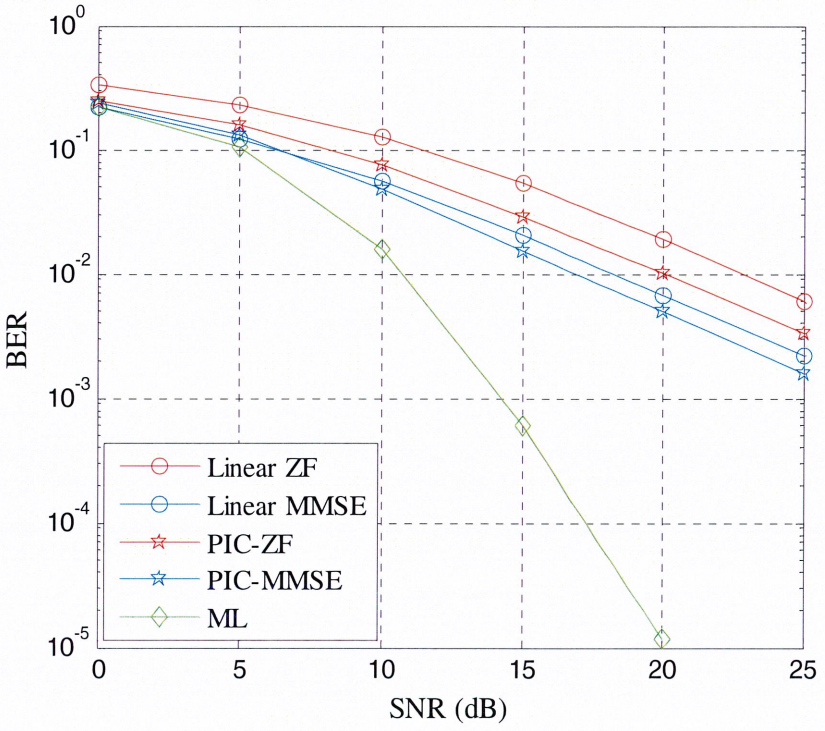


Fig. 4.5 BER performance of PIC detector versus SNR with uncorrelated channel.

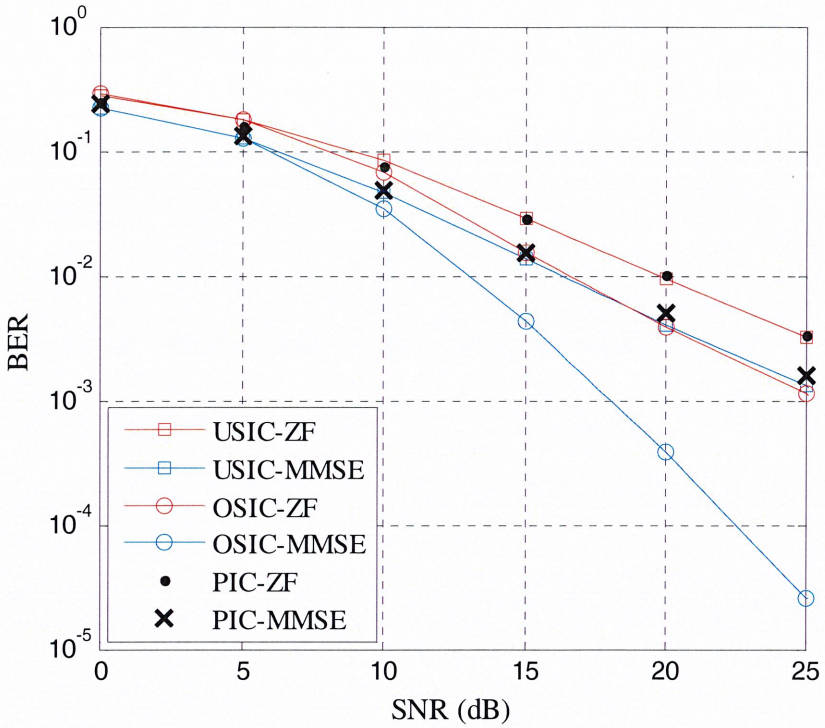


Fig. 4.6 Comparison between the performance of SIC and PIC detectors with uncorrelated channel.

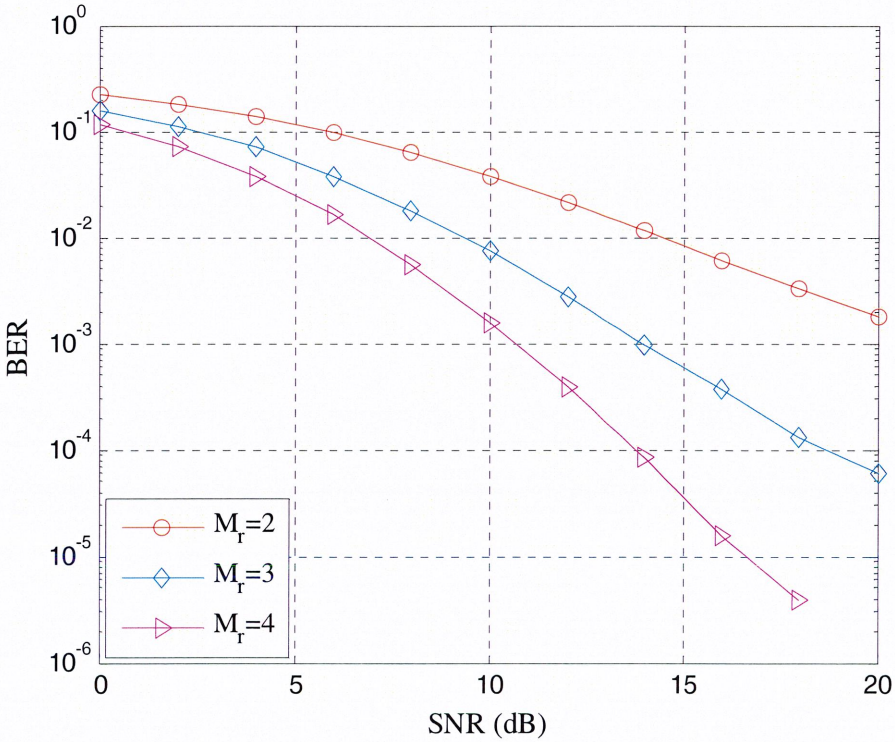


Fig. 4.7 Performance of OSIC-MMSE with uncorrelated channel for $M_t = 2$ and $M_r = \{2,3,4\}$.

As shown, the UCA significantly outperforms the ULA at endfire (θ_r=90°). However, at central AOA values less than approximately 45° and greater than 135° (i.e., approaching the broadside of the ULA), the linear array performs similarly to or even better than the UCA.

Fig. 4.9 shows the performance of the ULA and UCA receiver as a function of AOA (θ_r) for various angular spread, σ = {1°, 5°, 20°}, and fixed SNR= 20 dB. As shown, the variability in the performance of both arrays is more pronounced at moderate and high angle spreads. It can be noticed that at small and moderated angle spreads the UCA performs similarly to or even better than the linear array. At high angular spread, the UCA outperforms the ULA by an over an order of magnitude at endfire (θ_r=90°), while, the ULA provides an order of magnitude improvement over the UCA near the broadside of the ULA (θ_r=0° and 180°). This variability in the ULA performance is due to the fact that the correlation between elements is high for the ULA when the central AOA is near end fire. The worst case for the UCA when θ_r=45° and 135° since in these cases two elements are directly behind and parallel to the other two elements (strongly correlated).

Fig. 4.10 compares the BER performance of the ULA and UCA receiver versus the angle spread (σ) at SNR=20 dB, and various AOA, θ_r = {0°, 45°, 90°}. As shown, for both antenna arrays as the angle spread increases (correlation decreases) the reliability of the system is improved. Again, the performance of the ULA is poor for θ_r=90° since the correlation across the array is high. Therefore, there is little diversity advantage. As well, the worst performance of the UCA when θ_r=45°. Since, in this case the correlation is high in view of the fact that elements three and four are directly behind elements one and two. In addition, as can be noticed the all curves (except, the ULA at θ_r=90°) approach the same performance as σ increases. Because for large σ, the AOA distribution approaches a uniform distribution which will provide low correlation among antennas for any value of θ_r.

Fig. 4.11 illustrates the BER performance of ULA and UCA receiver versus the receiver antenna spacing ($\frac{D_r}{\lambda}$) for σ =20°, SNR=20 dB, and various AOA θ_r={0°, 45°, 90°}. Note that D_r is the inter-element spacing for ULA and it is also related to the UCA radius such that the both arrays have the same aperture size. Thus, for 4x4 MIMO channel the radius of a UCA is related to the inter-element spacing of a ULA by (R_r=1.5D_r) . It can be seen that as the array size increases, the BER performance improves and floors at a certain value that is about one wavelength.

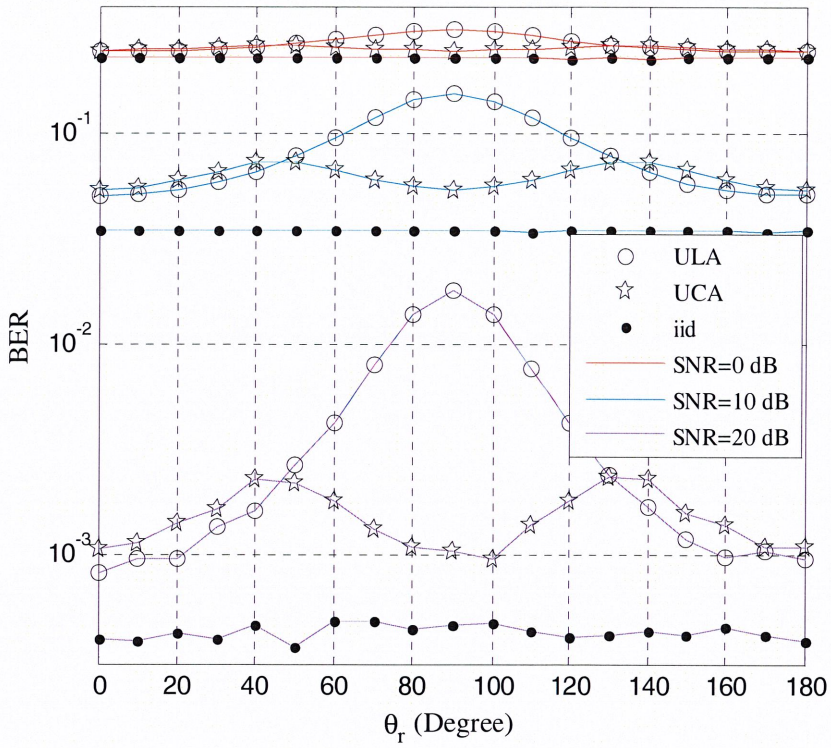


Fig. 4.8 BER performance of OSIC-MMSE detector for ULA and UCA receiver as a function of central AOA (θ_r) at various SNR, SNR= {0, 10, 20} dB, and σ =20°.

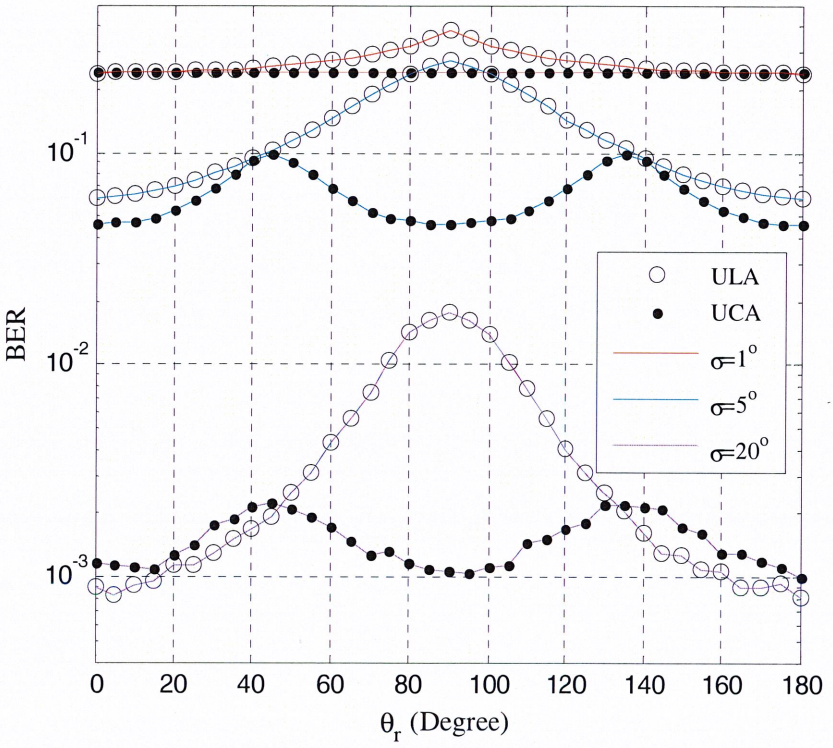


Fig. 4.9 BER performance of OSIC-MMSE detector for ULA and UCA receiver as a function of central AOA (θ_r) at various AS, σ = {1°, 5°, 20°}, and SNR= 20 dB.

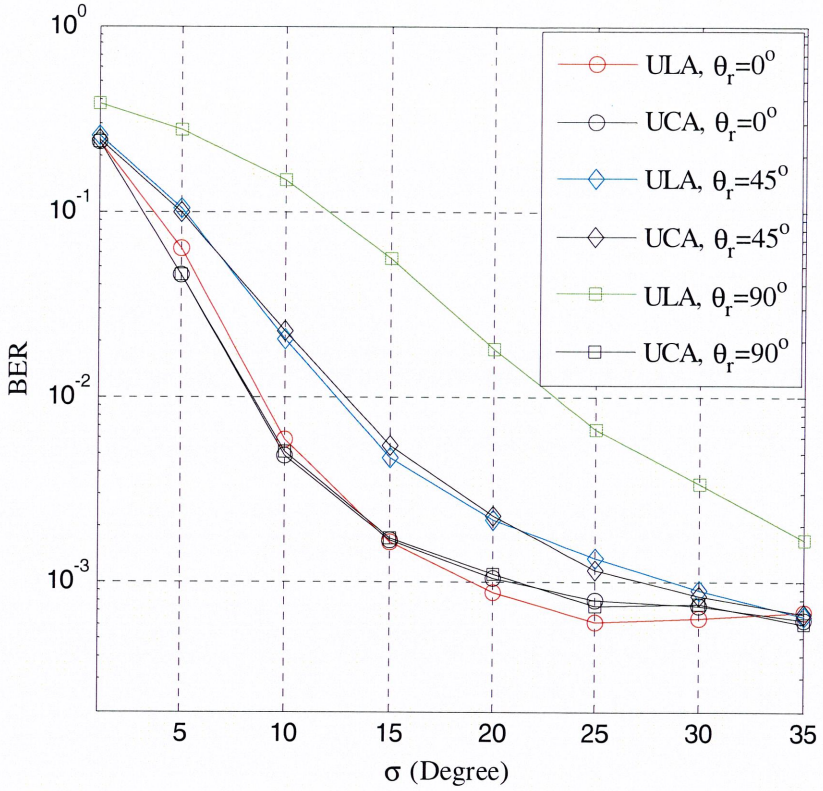


Fig. 4.10 BER performance of OSIC-MMSE detector for ULA and UCA receiver versus angular spread (σ) at different AOA, θ_r = {0°, 45°, 90°}, and SNR= 20dB.

However, this behavior can't be seen for the ULA at θ_r=90°. Again this is because all four elements are in-line with the central AOA leading to high correlation between elements. However, for other values of θ_r, the ULA does approach the BER floor ($P_e = 6x10^{-4}$) since the four elements eventually become uncorrelated. The UCA also shows improving for θ_r=0°, 45°, 90° with increasing D_r. As expected, the worst case is θ_r=45°. Again, in this case elements three and four are directly behind elements one and two and, thus, will be highly correlated with those elements. However, as D_r increases the correlation is gradually diminished and the performance is close to the BER floor, unlike the worst case of ULA. At θ_r =0°, elements three is directly behind and, thus, highly correlated with element one. Consequently, as D_r increases the performance quickly approaches the BER floor. At θ_r =90°, all four elements become decorrelated as D_r is increased. Thus, the performance approaches the BER floor.

Finally, the BER performance is examined for WLAN 802.11*n* system utilizing VBLAST (SIC-MMSE) for 4x4 MIMO system employing UCA configurations at both ends considering Binary Phase Shift Keying (BPSK). Two radii R_r =0.5λ and 0.75λ are considered at STA

receiver. Fig. 4.12 illustrates a comparison of BER performance curves under different TG*n* models. Corresponding BER of an uncorrelated fading channel '*iid*' is also included for comparison. As can be seen that the link has its best performance for Model 'F' conditions, in this case it is the nearest performance curve to the uncorrelated fading channel curve. Model 'F' performance curve is followed by model 'C' then model 'A' with the lowest performance. Also, as expected, that the link performance improves as the radius of UCA at STA end increases from 0.5λ to 0.75λ.

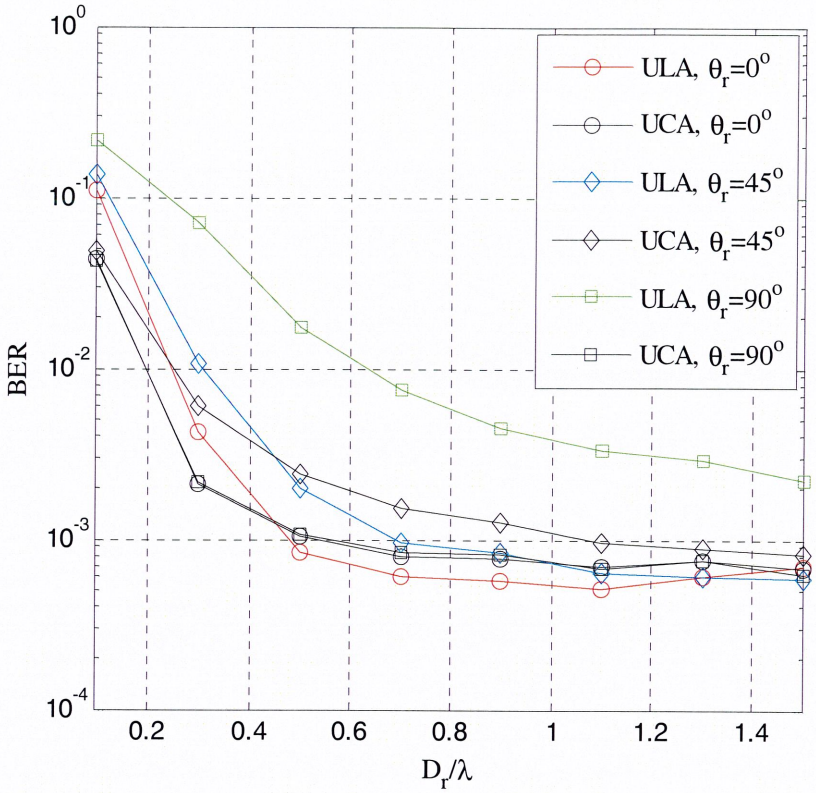


Fig. 4.11 BER performance of OSIC-MMSE detector for ULA and UCA receiver versus receiver antenna spacing for different AOA, θ_r = {0°, 45°, 90°}, σ =20°, and SNR= 20dB.

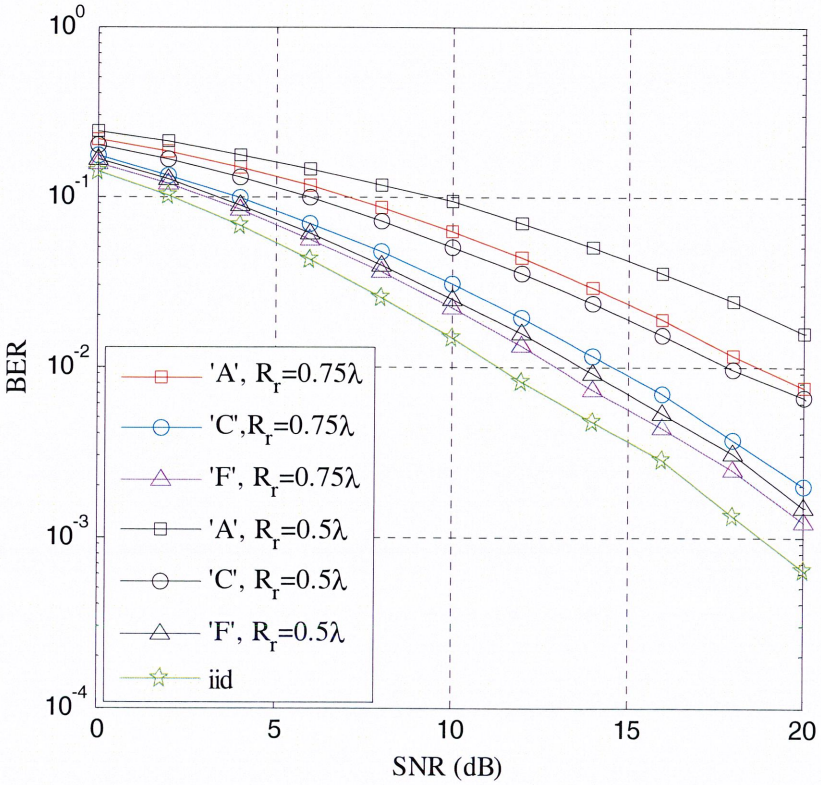


Fig. 4.12 BER performance of OSIC-MMSE detector for models 'A', 'C' and 'F' at various receiver radii (R_r=0.5λ and R_r=0.75λ).

4.4 Conclusion

In this chapter, the V-BLAST architecture and detection algorithms were presented. The principles of V-BLAST detection techniques including the suboptimal methods (linear signal detection, SIC and PIC) and optimal scheme which is ML detector were studied. Simulation results showed that the OSIC-MMSE yields the best bit error rate performance over the other schemes. However, there are several disadvantages with this scheme. It needs power reordering at each stage of detection, and the number of stages required increases linearly with the number of transmit antennas. As a result, long system delays can be expected when the number of stages is large. In addition, simulation results proved that the performance of PIC scheme is extremely close to the performance of unordered SIC scheme. Thus, PIC scheme offers a trade-off between the performance and system delay. In view of the fact that PIC scheme does not require power ordering and helps reduce the system delay. Since, it consists of two or more stages, as opposed to the SIC scheme. Furthermore, the impact of spatial fading correlation on the V-BLAST system based on the OSIC-MMSE scheme was investigated. The investigations compared the diversity performance of ULA and UCA. The results showed that the UCA outperforms the ULA for small and moderate angle spreads for similar aperture size. However, at high angle spread the ULA outperforms the UCA for certain angles-of-arrival (e.g., near broadside of the ULA). In addition, the worst performance for ULA occurs at the endfire angle. Given that, all elements are in-line with the central angle of arrival that leads to high correlation between elements. As well, the worst performance for UCA occurs at θ_r=45° and 135°, because, in these cases the correlation is high in view of the fact that elements three and four are directly behind elements one and two. Hence, the central angle of arrival has a significant impact on the BER performance of both the UCA and ULA. In addition, with small values of angle spread, there is little diversity advantage from either array; while for large angle spreads both arrays provide enhancement to the performance. Moreover, the performance analysis was investigated under realistic IEEE802.11*n* different channel scenarios. The result shows that with a proper selection of UCA radius the performance of uncorrelated channel can be achieved by model 'F', which is a simulation of large space indoor environment conditions.

Chapter 5

Effects of Spatial Correlation on the MIMO Channel Estimation Error

Most MIMO systems are based on perfect channel knowledge being available at the receiver. However, perfect channel knowledge is never known a priori. In practice, the channel has to be estimated to acquire the CSI at the receiver and at the transmitter in some cases. The MIMO channel estimation can be classified into two methods. Firstly, the data-aided, pilot based method that is based on training symbols with a priori known at the receiver [63] [64]. The second is a non-data aided, blind based, method that relies only on the received symbols [65] [66]. In these blind techniques, CSI is attained by exploiting statistical information and/or transmitted symbols properties (like finite alphabet, constant modulus, etc.). However, compared with training, blind channel estimation generally requires a long data record and high complexity. Therefore, this work focuses on the data aided based channel estimation method performance under different channel conditions. In [67] and [12], a number of training based methods have been studied including the least squares (LS), the scaled least squares (SLS), the linear minimum mean square error (LMMSE), and Relaxed minimum mean square error (RMMSE). The optimal training sequence designs are introduced for a MIMO system in [68]. In [69] and [70], it has been demonstrated that the presence of spatial correlation can help to achieve a better quality CSI. In [71], the impact of channel spatial correlation on the channel estimation error is evaluated when UCA antenna is employed at the receiver side. In this chapter, LS, SLS, LMMSE, and RMMSE training-based channel estimation methods are implemented and studied by applying the SSC channel model. The performance of channel estimators is investigated when applying optimum and orthogonal

training sequences. Also, the channel estimation accuracy of the LMMSE estimator is investigated at various angles of arrival, angle spread and inter-element spacing for both the ULA and UCA geometries. Moreover, the channel capacity is studied with considering the channel estimation error. This chapter is organized as follows: Section 5.1 presents the training-based channel estimation methods. Section 5.2 presents the numerical results and performance analysis Section 5.3 concludes the chapter with some remarks.

5.1 Training-Based Channel Estimation Methods

For training-based channel estimation, the relationship between the received signal and the training sequence is given by

$$\mathbf{Y} = \mathbf{HP} + \mathbf{N} \tag{5.1}$$

where $\mathbf{Y} \in \mathbb{C}^{M_r \times L}$ is received signal matrix, $\mathbf{P} \in \mathbb{C}^{M_t \times L}$ is the training sequence matrix and $\mathbf{N} \in \mathbb{C}^{M_r \times L}$ is the complex Gaussian noise matrix with zero mean and variance σ_n^2. L is the length of the training sequence.

The goal of a channel estimation algorithm is to recover the channel matrix **H** based on the knowledge of **Y** and **P**. The training based LS, SLS, LMMSE and RMMSE channel estimation methods are demonstrated in the following subsections. In this section, the analysis is taken from [12] and [67].

5.1.1 Least Squares Channel Estimator

Knowing **P** and **Y**, the least squares (LS) estimate for the channel matrix is given by

$$\widehat{\mathbf{H}}_{LS} = \mathbf{YP}^{\dagger} \tag{5.2}$$

As can be seen, the estimator does not require any knowledge about the channel parameters. The transmitted training power constrained by the following expression

$$\|\mathbf{P}\|_F^2 = \rho \tag{5.3}$$

where ρ is a given constant representing the total power and $\|.\|_F^2$ is the Frobenius matrix norm. According to [12]and [67] the minimum mean square error (MSE) of the estimated channel matrix is given as

$$\sigma^2_{e_{LS}} = \min_{\mathbf{P}} E\left\{\left\|\mathbf{H} - \widehat{\mathbf{H}}_{\mathbf{LS}}\right\|_F^2\right\} \quad \text{subject to} \quad \|\mathbf{P}\|_F^2 = \rho \tag{5.4}$$

Then Using (5.3) and (5.4)

$$\begin{aligned}
\sigma^2_{e_{LS}} &= E\left\{\left\|\mathbf{H} - \widehat{\mathbf{H}}_{\mathrm{LS}}\right\|_F^2\right\} \\
&= E\left\{\left\|\mathbf{N}\mathbf{P}^{\dagger}\right\|_F^2\right\} \\
&= E\left\{\mathrm{Tr}\left(\mathbf{N}^{\mathrm{H}}\mathbf{N}\mathbf{P}^{\dagger\,\mathrm{H}}\mathbf{P}^{\dagger}\right)\right\} \\
&= E\left\{\mathbf{N}^{\mathrm{H}}\mathbf{N}\right\}\mathrm{Tr}\left\{\left(\mathbf{P}\mathbf{P}^{\mathrm{H}}\right)^{-1}\right\} \\
&= \sigma_n^2 M_r \mathrm{Tr}\left\{\left(\mathbf{P}\mathbf{P}^{\mathrm{H}}\right)^{-1}\right\}
\end{aligned} \tag{5.5}$$

Using (5.5) the optimization problem (5.4) can be written as

$$\min_{\mathbf{P}} \mathrm{Tr}\{(\mathbf{P}\mathbf{P}^H)^{-1}\} \quad \text{subject to} \quad \mathrm{Tr}\{\mathbf{P}\mathbf{P}^H\} = \rho \tag{5.6}$$

It is shown that any training matrix is optimal for (5.6) if it satisfies the equation

$$\mathbf{P}\mathbf{P}^H = \frac{\rho}{M_t}\mathbf{I} \tag{5.7}$$

Consequently, any training matrix with orthogonal rows of the same norm($\sqrt{\frac{\rho}{M_t}}$) is optimal. A possible choice for a training sequence fulfilling this criterion could be the standard discrete Fourier transform (DFT) matrix.

$$\mathbf{P} = \sqrt{\frac{\rho}{LM_t}}\begin{bmatrix} 1 & 1 & \cdots & 1 \\ 1 & W_L & \cdots & W_L^{L-1} \\ \vdots & \vdots & \cdots & \vdots \\ 1 & W_L^{M_t-1} & \cdots & W_L^{(M_t-1)(L-1)} \end{bmatrix} \tag{5.8}$$

where $W_L = e^{j2\pi/L}$. So, the minimum MSE is given by

$$\min_{\mathbf{P}} \sigma^2_{e_{LS}} = \frac{\sigma_n^2 M_t^2 M_r}{\rho} \tag{5.9}$$

As can be seen from (5.9) the optimal performance of the LS is influenced by the square of the number of antenna elements at the transmitter and the number of elements at the receiver. However, the channel matrix has no effect on the MSE.

5.1.2 Scaled Least Squares Channel Estimator

The scaled least squares (SLS) method further reduces the estimation error than that of the LS method. This improvement is achieved by optimally scale the LS channel estimate as introduced in [67]. Using this idea and (5.2), the channel estimation error is given by

$$\begin{aligned} E\left\{\left\|\mathbf{H}-\gamma\widehat{\mathbf{H}}_{LS}\right\|_{\mathrm{F}}^{2}\right\} &= \mathrm{Tr}\left\{E\left\{\left(\mathbf{H}-\gamma\widehat{\mathbf{H}}_{LS}\right)^{H}\left(\mathbf{H}-\gamma\widehat{\mathbf{H}}_{LS}\right)\right\}\right\} \\ &= (1-\gamma)^{2}\mathrm{Tr}\{\mathbf{R}_{H}\}+\gamma^{2}\sigma_{n}^{2}M_{r}\mathrm{Tr}\{(\mathbf{P}\mathbf{P}^{H})^{-1}\} \\ &= (1-\gamma)^{2}\mathrm{Tr}\{\mathbf{R}_{\mathbf{H}}\}+\gamma^{2}\sigma_{\mathrm{e}_{LS}}^{2} \end{aligned} \tag{5.10}$$

where γ is the scaling factor, and $\boldsymbol{R}_H = E\{\boldsymbol{H}^H\boldsymbol{H}\}$ is the matrix of channel correlations.(5.10) is minimized with

$$\gamma_{\mathrm{o}} = \frac{\mathrm{Tr}\{\mathbf{R}_{H}\}}{\sigma_{\mathrm{e}_{\mathrm{LS}}}^{2}+\mathrm{Tr}\{\mathbf{R}_{H}\}} \tag{5.11}$$

and the minimum of (5.10) with respect to γ is

$$\begin{aligned} \sigma_{\mathrm{e}_{SLS}}^{2} &= \min_{\gamma} E\{\|\boldsymbol{H}-\gamma\widehat{\boldsymbol{H}}\|_{F}^{2}\} = E\{\|\boldsymbol{H}-\gamma_{o}\widehat{\boldsymbol{H}}\|_{F}^{2}\} \\ &= \sigma_{\mathrm{e}_{LS}}^{2}\frac{\mathrm{Tr}\{\mathbf{R}_{H}\}}{\sigma_{\mathrm{e}_{LS}}^{2}+\mathrm{Tr}\{\mathbf{R}_{H}\}} < \sigma_{\mathrm{e}_{LS}}^{2} \end{aligned} \tag{5.12}$$

The optimal training matrix for the SLS channel estimation method can be found by solving the following constrained optimization problem

$$\min_{\mathbf{P}} \sigma_{\mathrm{e}_{SLS}}^{2} \quad \text{subject to} \quad \mathrm{Tr}\{\mathbf{P}\mathbf{P}^{H}\} = \rho \tag{5.13}$$

From (5.12) the $\mathrm{Tr}\{\mathbf{R}_H\}$ is not a function of $\mathbf{P}$, then, $\sigma_{\mathrm{e}_{\mathrm{LS}}}^{2}$ is the only term that depends on $\mathbf{P}$ So, the optimal choice of training matrix for the SLS channel estimator is the same as for the LS method. Under the optimal training the MSE is given by

$$\min_{\mathbf{P}} \sigma_{\mathrm{e}_{SLS}}^{2} = \left[\mathrm{Tr}\{\mathbf{R}_{H}\}^{-1}+\left(\frac{\rho}{\sigma_{n}^{2}M_{t}^{2}M_{r}}\right)\right]^{-1} \tag{5.14}$$

The SLS channel estimate is given by

$$\begin{aligned}\widehat{\mathbf{H}}_{SLS} &= \gamma_o \widehat{\mathbf{H}}_{LS} \\ &= \frac{\mathrm{Tr}\{\mathbf{R}_H\}}{\sigma_n^2 M_r \mathrm{Tr}\{(\mathbf{P}\mathbf{P}^{\mathbf{H}})^{-1}\} + \mathrm{Tr}\{\mathbf{R}_H\}} \mathbf{Y}\mathbf{P}^{\dagger}\end{aligned} \tag{5.15}$$

In practice, $\boldsymbol{R}_H$ can be obtained using the channel matrix estimated by the LS method, in this case the resulting estimator is referred to the LS-SLS. Accordingly,

$$\mathrm{Tr}\{\widehat{\mathbf{R}}_H\} = \mathrm{Tr}\{\widehat{\mathbf{H}}_{LS}^H \widehat{\mathbf{H}}_{LS}\} \tag{5.16}$$

5.1.3 Linear Minimum Mean-Square Error Channel Estimator

In the linear minimum mean square error (LMMSE), the estimated channel matrix is given as [67]

$$\widehat{\mathbf{H}}_{LMMSE} = \mathbf{Y}\boldsymbol{Q} \tag{5.17}$$

where $\boldsymbol{Q}$ has to be obtained so that the MSE is minimized

$$\boldsymbol{Q}_o = \min_{\boldsymbol{Q}} E\{\|\mathbf{H} - \widehat{\mathbf{H}}_{LMMSE}\|_F^2\} = \min_{\boldsymbol{Q}} \mathrm{E}\{\|\mathbf{H} - \mathbf{Y}\boldsymbol{Q}\|_F^2\} \tag{5.18}$$

Using (5.2), the MSE can be written as

$$\begin{aligned}\sigma_{e_{LMMSE}}^2 &= E\{\|\mathbf{H} - \mathbf{Y}\boldsymbol{Q}\|_F^2\} \\ &= \mathrm{Tr}\{\mathbf{R}_H\} - \mathrm{Tr}\{\mathbf{R}_H\mathbf{P}\boldsymbol{Q}\} - \mathrm{Tr}\{\boldsymbol{Q}^H\mathbf{P}^{\mathrm{H}}\mathbf{R}_H\} + \mathrm{Tr}\{\boldsymbol{Q}^H(\mathbf{P}^H\mathbf{R}_H\mathbf{P} + \sigma_n^2 M_r\mathbf{I})\boldsymbol{Q}\}\end{aligned} \tag{5.19}$$

The optimal $\boldsymbol{Q}$ that minimizing the MSE can be represented by

$$\boldsymbol{Q}_o = (\mathbf{P}^H\mathbf{R}_H\mathbf{P} + \sigma_n^2 M_r\mathbf{I})^{-1}\mathbf{P}^H\mathbf{R}_H \tag{5.20}$$

Therefore, the estimated channel is given by

$$\widehat{\mathbf{H}}_{LMMSE} = \mathbf{Y}(\mathbf{P}^H\mathbf{R}_H\mathbf{P} + \sigma_n^2 M_r\mathbf{I})^{-1}\mathbf{P}^H\mathbf{R}_H \tag{5.21}$$

The MSE of the LMMSE can be expressed as

$$\sigma^2_{e_{LMMSE}} = \mathrm{Tr}\{(\mathbf{R}_H{}^{-1} + \frac{\mathbf{P}\mathbf{P}^H}{\sigma_n^2 M_r})^{-1}\} \tag{5.22}$$

The eigenvalue decomposition of $\mathbf{R}_H$ can be expressed as

$$\mathbf{R}_H = \mathbf{Q}\boldsymbol{\Lambda}\mathbf{Q}^H \tag{5.23}$$

where $\boldsymbol{Q}$ is the unitary eigenvector matrix and $\boldsymbol{\Lambda}$ is the diagonal matrix with nonnegative eigenvalues. Using this form, (5.22) can be written as

$$\begin{aligned}\sigma^2_{\mathrm{e\,LMMSE}} &= \mathrm{Tr}\{(\mathbf{Q}^H\boldsymbol{\Lambda}^{-1}\mathbf{Q} + \frac{\mathbf{P}\mathbf{P}^H}{\sigma_n^2 M_r})^{-1}\} \\ &= \mathrm{Tr}\{(\boldsymbol{\Lambda}^{-1} + \frac{\mathbf{Q}^H\mathbf{P}\mathbf{P}^H\mathbf{Q}}{\sigma_n^2 M_r})^{-1}\} \\ &= \mathrm{Tr}\{(\boldsymbol{\Lambda}^{-1} + \widetilde{\mathbf{P}}\widetilde{\mathbf{P}}^H)^{-1}\}\end{aligned} \tag{5.24}$$

where

$$\widetilde{\mathbf{P}} = \frac{\mathbf{Q}^H\mathbf{P}}{\sqrt{\sigma_n^2 M_r}} \tag{5.25}$$

Using $\widetilde{\mathbf{P}}$ the transmit power (5.3) can be replaced with the following equivalent form

$$\mathrm{Tr}\{\widetilde{\mathbf{P}}\widetilde{\mathbf{P}}^H\} = \frac{\mathrm{Tr}\{\mathbf{Q}^H\mathbf{P}\mathbf{P}^H\mathbf{Q}\}}{\sigma_n^2 M_r} = \frac{\rho}{\sigma_n^2 M_r} \tag{5.26}$$

Based on properties of the unitary eigenvector matrix$\boldsymbol{Q}$, $\widetilde{\mathbf{P}}\widetilde{\mathbf{P}}^H$ has a diagonal structure as given by

$$\widetilde{\mathbf{P}}\widetilde{\mathbf{P}}^H = \begin{bmatrix} p_1^2 & & & \\ & p_2^2 & & \\ & & \ddots & \\ & & & p_{M_t}^2 \end{bmatrix} \tag{5.27}$$

where p_i^2 is the power of each combined training symbol. The optimal training matrix of the LMMSE can be derived by using the Lagrange multiplier method with considering (5.24), (5.26), and (5.27)

$$L(\widehat{\mathbf{P}},\mu) = \mathrm{Tr}\{(\boldsymbol{\Lambda}^{-1} + \widetilde{\mathbf{P}}\widetilde{\mathbf{P}}^H)^{-1}\} + \mu(\mathrm{Tr}\{\widetilde{\mathbf{P}}\widetilde{\mathbf{P}}^H\} - \frac{\rho}{\sigma_n^2 M_r})$$
$$= \sum_{i=1}^{M_t}(\lambda_i^{-1} + |\widetilde{p}_i|^2)^{-1} + \mu\sum_{i=1}^{M_t}(|\widetilde{p}_i|^2 - \frac{\rho}{\sigma_n^2 M_t M_r}) \tag{5.28}$$

where μ is the Lagrange multiplier, and λ_i is the ith eigenvalue in $\boldsymbol{\Lambda}$. The optimal $\widetilde{p}_i$ can be found by setting $\frac{\partial L(\tilde{X},\mu)}{\partial \tilde{x} i} = 0$ for i=1,..., M_t and which yields

$$\widetilde{p}_i\left[(\lambda_i^{-1} + |\widetilde{p}_i|^2)^{-2} - \mu\right] = 0, \quad i = 1, \ldots, M_t \tag{5.29}$$

From (5.29) the water-filling type solution is obtained to (5.28)

$$\widetilde{p}_i = \sqrt{(\mu_o - \lambda_i^{-1})^+} \tag{5.30}$$

where $(x)^+$=max(x,0) and the constant $\mu_o = 1/\sqrt{\mu}$ has to be adjusted to satisfy the transmitted power constraint (5.26). Then the optimal $\widetilde{\mathbf{P}}$ can be represented in the matrix form as

$$\widetilde{\mathbf{P}} = \sqrt{(\mu_o \mathbf{I} - \boldsymbol{\Lambda}^{-1})^+} \tag{5.31}$$

Finally, the optimal training matrix is given as

$$\mathbf{P} = \sqrt{\sigma_n^2 M_r}\mathbf{Q}\sqrt{(\mu_o \mathbf{I} - \boldsymbol{\Lambda}^{-1})^+} \tag{5.32}$$

5.1.4 Relaxed Minimum Mean-Square Error Channel Estimator

The LMMSE channel estimator assumes the perfect knowledge of the matrix $\mathbf{R}_H$. However, in practice this assumption is unrealistic. Thus, the LMMSE estimator is relaxed and simplified by replacing $\mathbf{R}_H$ with the matrix $\delta\mathbf{I}$, where the parameter δ has to be adjusted to minimize the MSE. Hence, (5.21) can be written as

$$\widehat{\mathbf{H}}_{RMMSE} = \delta\mathbf{Y}(\delta\mathbf{P}^H\mathbf{P} + \sigma_n^2 M_r\mathbf{I})^{-1}\mathbf{P}^H$$
$$= \frac{\delta}{\sigma_n^2 M_r}\mathbf{Y}(\mathbf{I} - \frac{\delta M_t}{\delta\rho + \sigma_n^2 M_t M_r}\mathbf{P}^H\mathbf{P})\,\mathbf{P}^H \tag{5.33}$$

Using (5.33) and assuming orthogonal training (5.7), the channel MSE can be expressed as

$$\begin{aligned}\sigma^2_{\mathrm{e}_{\mathrm{RMMSE}}} &= E\{\|\boldsymbol{H}-\widehat{\boldsymbol{H}}_{RMMSE}\|_F^2\} \\ &= \left(\frac{M_r\zeta^2\rho^2}{M_t}+\sigma_n^2M_r\rho\right)\left(\frac{\delta M_t}{\delta\rho_x+\sigma_n^2M_tM_r}-\frac{M_t\zeta^2}{\zeta^2\rho+\sigma_n^2M_t}\right)^{-2} \\ &+\frac{\zeta^2\sigma_n^2M_rM_t{}^2}{\zeta^2\rho+\sigma_n^2M_t}\end{aligned} \tag{5.34}$$

where $\zeta^2 \triangleq \mathrm{Tr}\{\mathbf{R}_H\}/M_tM_r$. (5.34) is minimized with

$$\delta_{opt} = \zeta^2M_r = \frac{\mathrm{Tr}\{\mathbf{R}_H\}}{M_t} \tag{5.35}$$

Using (5.35), the RMMSE channel estimator is given by

$$\widehat{\mathbf{H}}_{RMMSE} = \mathbf{Y}\left[\mathbf{P}^H\mathbf{P}+\frac{\sigma_n^2M_tM_r}{\mathrm{Tr}\{\mathbf{R}_H\}}\mathbf{I}\right]^{-1}\mathbf{P}^H \tag{5.36}$$

It can be seen that if the orthogonal training is used, then the RMMSE estimator of (5.36) is equivalent to the SLS estimator of (5.15). In practice, the estimate (5.16) can be used instead of the exact value of $\mathrm{Tr}\{\mathbf{R}_H\}$ in this case the resulting estimator will be referred to as the LS-RMMSE estimator. Using the orthogonal training matrix (5.7) the LS-RMMSE can be expressed as

$$\widehat{\mathbf{H}}_{\mathrm{LS}_{RMMSE}} = \frac{\mathrm{Tr}\{\mathbf{Y}\mathbf{Y}^H\}M_t}{\rho(\mathrm{Tr}\{\mathbf{Y}\mathbf{Y}^{\mathrm{H}}\}+\sigma_n^2M_tM_r)}\mathbf{Y}\mathbf{P}^H \tag{5.37}$$

In contradiction of the original RMMSE estimator (5.36), the LS-RMMSE estimator (5.37) does not require any knowledge of $\mathrm{Tr}\{\mathbf{R}_H\}$. Using (5.34) the RMMSE estimation error for an orthogonal training matrix (5.7) is given by

$$\sigma^2_{\mathrm{e}_{RMMSE}} = \left[\mathrm{Tr}\{\mathbf{R}_H\}^{-1}+\left(\frac{\rho}{\sigma_n^2M_t^2M_r}\right)\right]^{-1} \tag{5.38}$$

5.2 Numerical Results

In this section, the channel estimation error for two systems with ULA-MIMO and UCA-MIMO receivers has been studied. In both systems, the transmitter MIMO antenna is assumed to be ULA with inter-elements spacing (D_t). ULA-MIMO receiver antenna has a uniform inter-elements spacing (D_r) and placed vertically such that AOA= 0° is broadside case. UCA-MIMO receiver antenna has radius (R_r). The numerical studies are performed for MIMO systems with SSC channel model where WLAN uplink scenario is modelled with transmitter at the MT and receiver at the AP. The LS, SLS, LMMSE and RMMSE are implemented at the receiver. The following parameters are considered, $L= M_t$, D_t =0.5λ, D_r =0.5λ, R_r =0.75λ, 10000 channel realizations, and the MSE is normalized by $M_t x M_r$.

Fig. 5.1 presents the normalized MSEs of the LS, LS-SLS, and SLS channel estimators versus SNR with optimal training for M_r=4, and M_t =2,4. As expected from Section 5.1 the performance of these estimators decreases with the increase in number of transmit antennas.

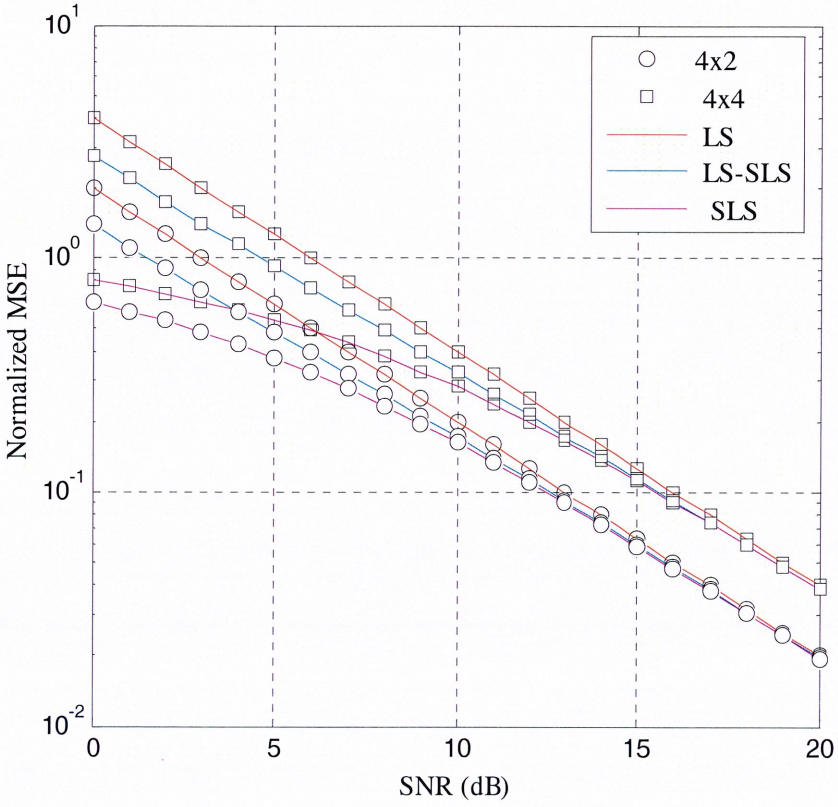


Fig. 5.1 Channel estimation MSEs of LS, LS-SLS, and SLS versus SNR in uncorrelated environment for M_r = 4 and M_t = 2,4.

Also, it can be seen that the LS is the worst estimator in view of the fact that it does not take into account the channel properties.At low SNRs, both the LS-SLS and SLS estimators has better performance than the LS estimator. In addition, the SLS estimator outperforms the LS-SLS estimator for the reason that it has perfect knowledge of $\mathrm{Tr}\{\mathbf{R}_H\}$, whereas, at high SNRs the performances of these estimators are identical.

Fig. 5.2 shows the normalized MSEs of the LMMSE estimator versus SNR with the orthogonal and optimal training for M_r=4, and M_t =2,4. It can be observed that the performance of the optimal training is better than the orthogonal training especially at low SNRs. As well, it is noticed that when M_t is small and SNR is high the orthogonal training is nearly optimal. From the presented results in Fig. 5.1 and Fig. 5.2 it is evident that the LMMSE estimator performs better than the LS and SLS techniques.

Fig. 5.3 demonstrates the normalized MSEs of the LS, SLS, LMMSE, and RMMSE channel estimators with orthogonal training versus SNR, for M_t =M_r =4. One can see that the LS estimator has the worst performance, while the LMMSE has the best performance among all techniques. However, it requires more prior knowledge about the channel than the other methods. Also the performances of the SLS and RMMSE estimators are identical and they necessitate less prior knowledge about the channel than the LMMSE estimator. So, by compromising the achieved performance these estimators provide a good tradeoff between the performance and the required channel knowledge.

Fig. 5.4 illustrates the normalized MSEs of the LMMSE channel estimator as a function of AOA (θ_r) at various SNR (0 dB, 10 dB, and 20 dB) for orthogonal training , and σ=20°. It can be seen that at high SNR the MSE is less and the spatial correlation has a less pronounced effect on improving the channel estimation error. However, at moderate and low SNR the spatial correlation reduces the channel estimation error. Moreover, the presented result reveals that the MSE in general is more affected by the AOA in the ULA unlike the UCA. In addition the performances of the ULA and UCA are identical near broadside of the array{θ_r=0° and 180°}. It is also noted that the ULA outperforms the UCA at endfire {θ_r=90°} .So, the best channel estimation error can be achieved with the ULA receiver at θ_r=90° (maximum correlation). Therefore, it is shown that ULA minimizes the MSE at moderate and low SNR and the performance is further improved with the channel spatial correlation ,i.e., for example

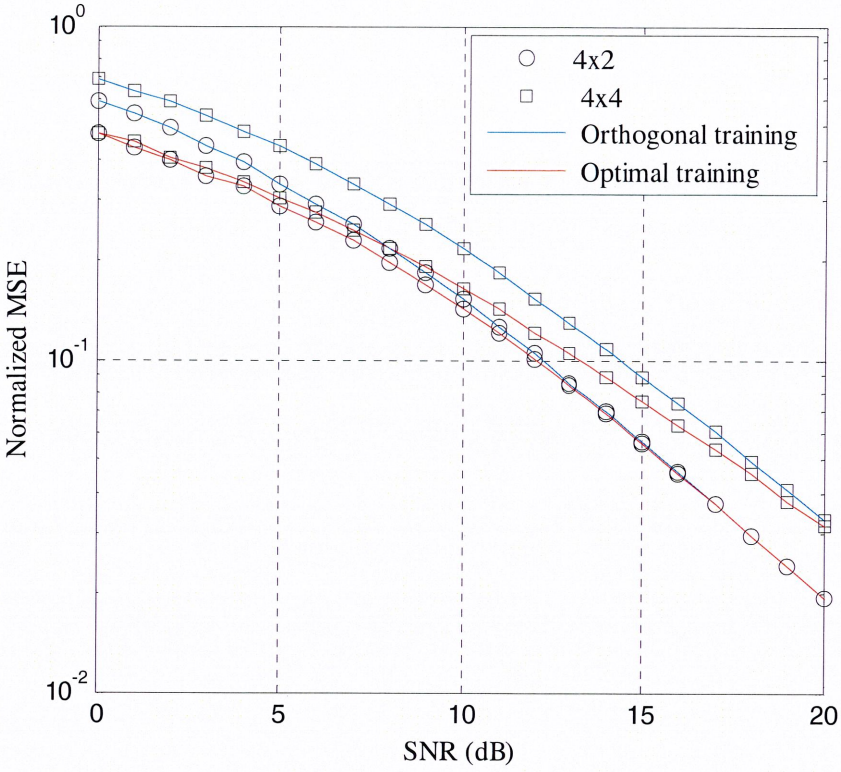


Fig. 5.2 Channel estimation MSEs of LMMSE estimator in uncorrelated environment versus SNR with orthogonal and optimal sequences for $M_r = 4$ and $M_t = 2,4$.

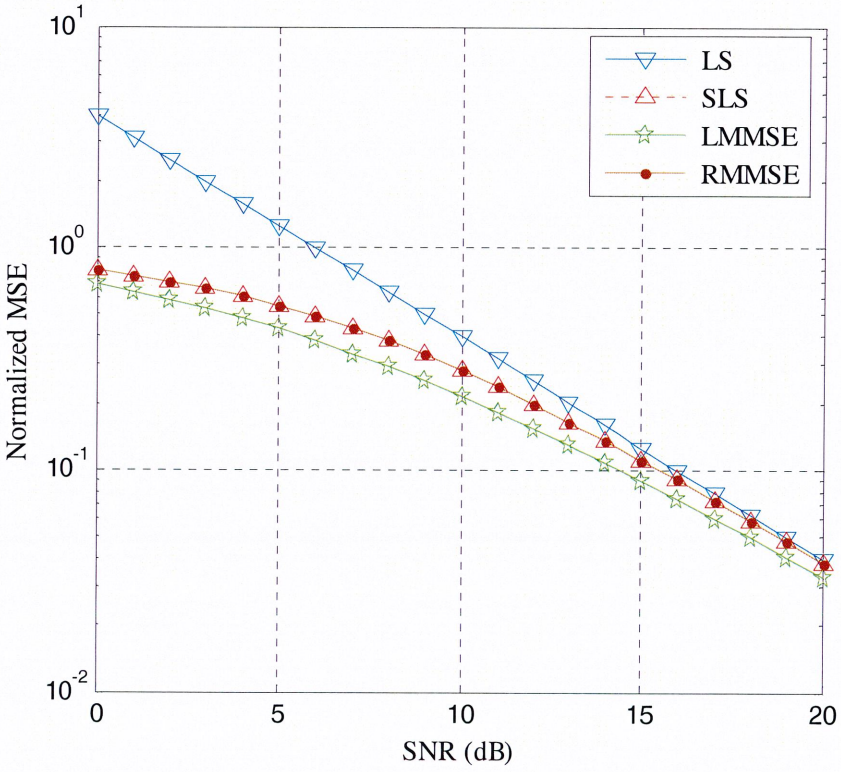


Fig. 5.3 Channel estimation MSEs of the LS, SLS, LMMSE, and RMMSE estimators in uncorrelated environment versus SNR with orthogonal training sequence.

the performance improvement from iid channel to spatial correlated channel (ULA) is approximately 15.95% at 0 dB, and 8.94% at 10 dB.

Fig. 5.5 illustrates the normalized MSEs of the SLS channel estimator as a function of AOA (θ_r) at various SNR (0 dB, 10 dB, and 20 dB) for orthogonal training, and σ=20°. As compared with the preceding figure the MSE of the SLS is higher than the MSE of LMMSE in case of '*iid*' channel and UCA receiver. However, in case of ULA receiver, the MSE is nearly the same. Thus, the SLS estimator is preferred to used in ULA since it needs less a priori knowledge about the channel on the contrary of the LMMSE estimator.

In Fig. 5.6 and Fig. 5.7, numerical analyses are presented in the form of 3-D graphs to show the relationship between the normalized MSE of the LMMSE channel estimator, AS and AOA for ULA and UCA receiver, respectively. Here the SNR is chosen to be 10 dB. It is known that larger AS results in smaller correlation, while smaller AS leads to more severe correlation. As a result, the varied values of AS reflect different levels of spatial correlation. From these Figures one can see that as AS increases, the performance of channel estimation gets worse. This means that a small spatial correlation undermines channel estimation quality. In addition, for small AS the AOA does not impinge on the MSE. In contrary, for higher AS the effects of AOA is more prominent in ULA when compared to UCA. In case of ULA, the best performance can be accomplished with θ_r = 90° and at low AS. On the other hand, in case of UCA, the minimum MSE can be attained with θ_r = 45° and 135° due to the fact that, two elements are directly behind and parallel to the other two elements (highest correlation), this can be noticed particularly at high AS. Thus, it can be demonstrated that the best performance of the LMMSE channel estimator can be realized by the ULA receiver at small AS and AOA=90°.

Furthermore investigations are done by varying the antenna element spacing or radius in both the transmitter and receiver arrays. The results are given in Fig. 5.8 and Fig. 5.9 for ULA and UCA receiver, respectively. In these Figs. the analyses are performed for 4x4 MIMO channel, AOA=90° with optimal training at SNR=10 dB and AS=20°. It is known that as antenna element spacing in ULA or radius in UCA deceases the channel spatial correlation increases, or in other words, with these conditions the accuracy of the channel estimation can be improved.

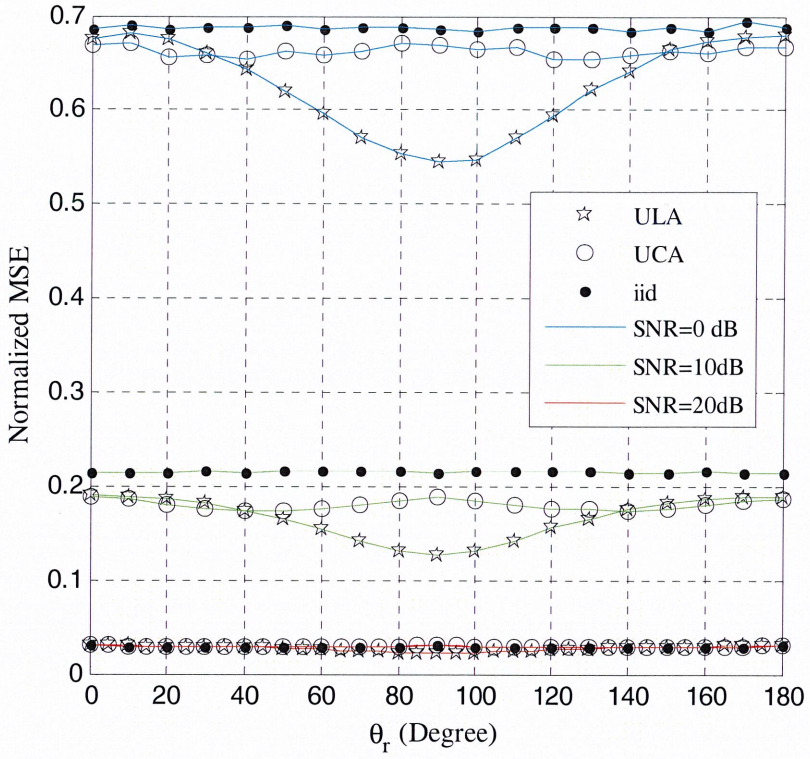


Fig. 5.4 Channel estimation MSEs of the LMMS as a function of AOA at various SNR, for orthogonal training sequence at $\sigma = 20^{o}$.

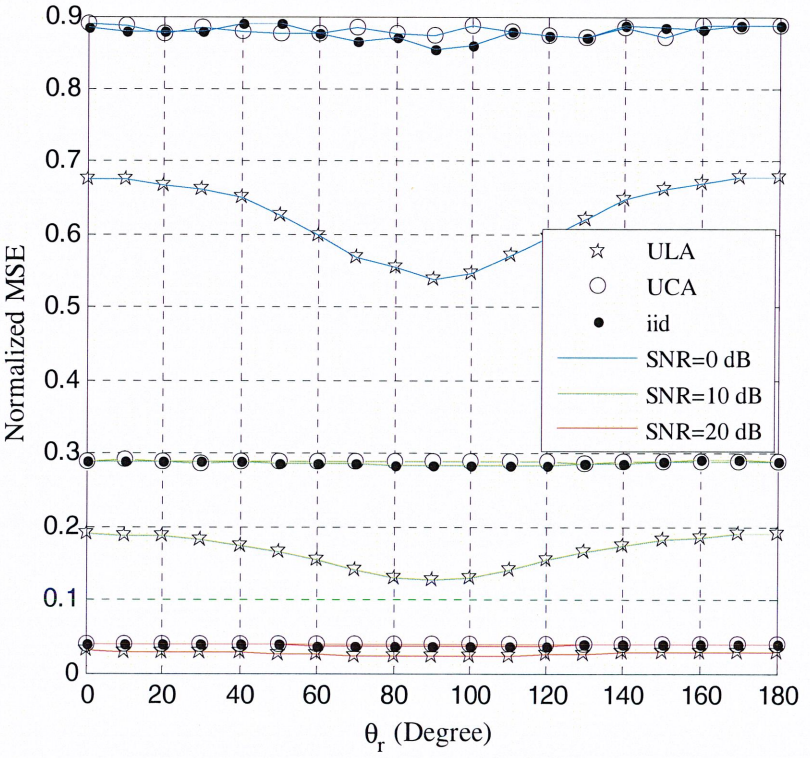


Fig. 5.5 Channel estimation MSEs of the SLS as a function of AOA at various SNR, for orthogonal training sequence at $\sigma = 20^{o}$.

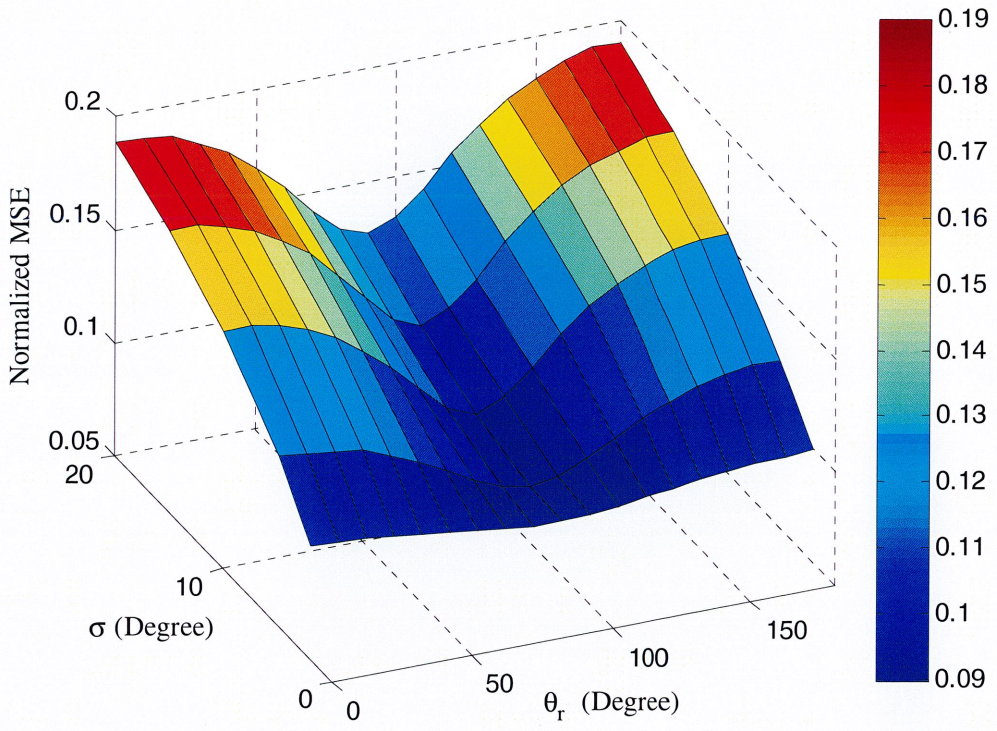


Fig. 5.6 Normalized MSE of LMMSE channel estimator versus AOA vs. AS at SNR =10 dB, in case of ULA-MIMO receiver.

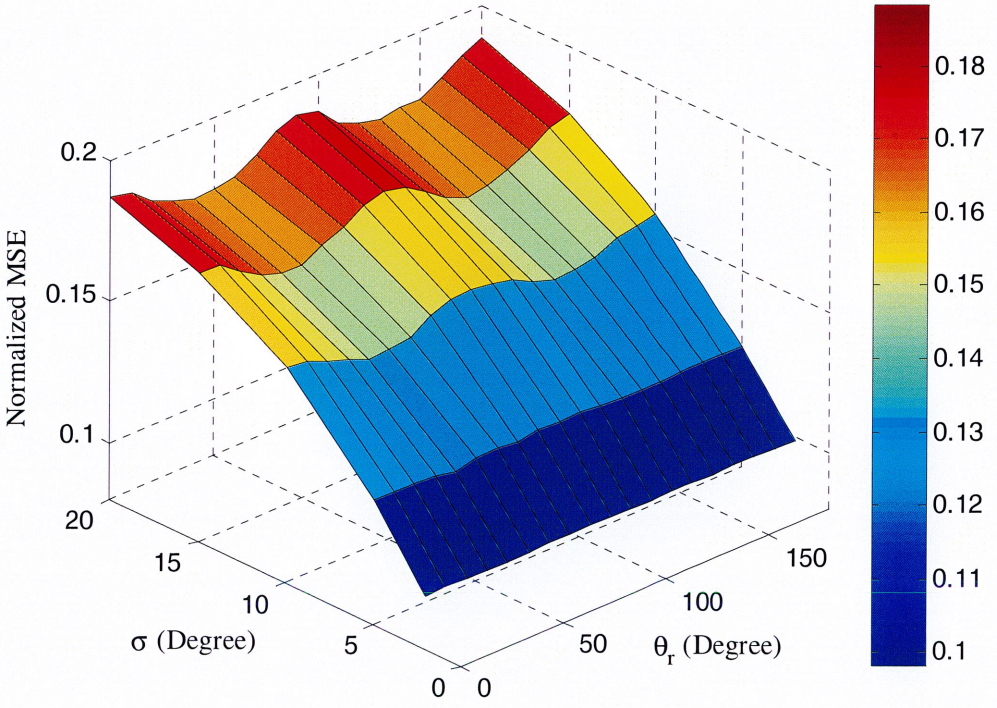


Fig. 5.7 Normalized MSE of LMMSE channel estimator versus AOA vs. AS at SNR =10dB, in case of UCA-MIMO receiver.

Hence, from these Figs the preferred antenna element spacing or radius can be acquired. Thus, in case of ULA receiver the minimum estimation error (MSE= 0.082) can be accomplished with $D_t = 0.6\lambda$ and $D_r = 0.5\lambda$. In addition, in case of UCA receiver the minimum error (MSE = 0.142) can be achieved with $D_t = 0.6\lambda$ and $R_r = 0.75\lambda$ Note that the antenna element spacing or the radius cannot be selected less than 0.5λ because of the mutual coupling effect which can be neglected for element spacing greater than 0.5λ.

The effect of channel estimation error on the capacity performance is illustrated in Fig. 5.10. Fig. 5.10 presents the channel capacity of UCA-MIMO system with LMMSE channel estimator versus SNR at $\theta_r = 90^\circ$ and different AS ($\sigma = 1^\circ, 7^\circ, 20^\circ$) values. As can be seen that at high SNR, the capacity of the estimated channel is very near to the capacity when the channel is perfectly known to the receiver. This is due to the fact that at high SNR the channel estimation error becomes very small as shown in Fig. 5.11.

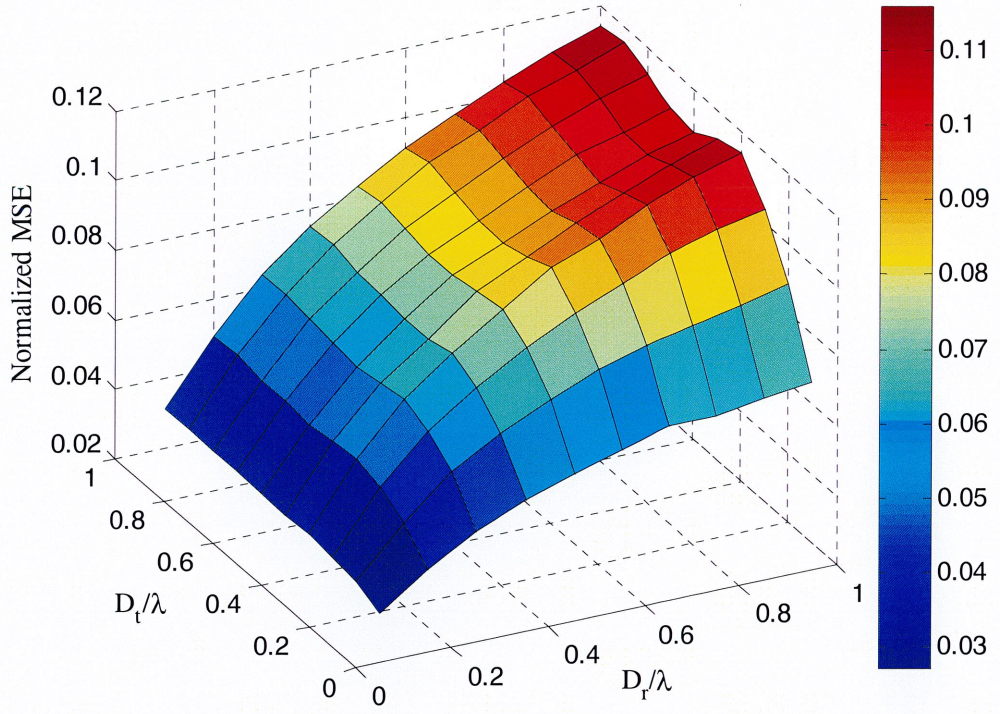


Fig. 5.8 Normalized MSE of the LMMSE channel estimator with optimal training for ULA-MIMO receiver at $\theta_r = 90^o$, SNR=10 dB and $\sigma = 20^o$.

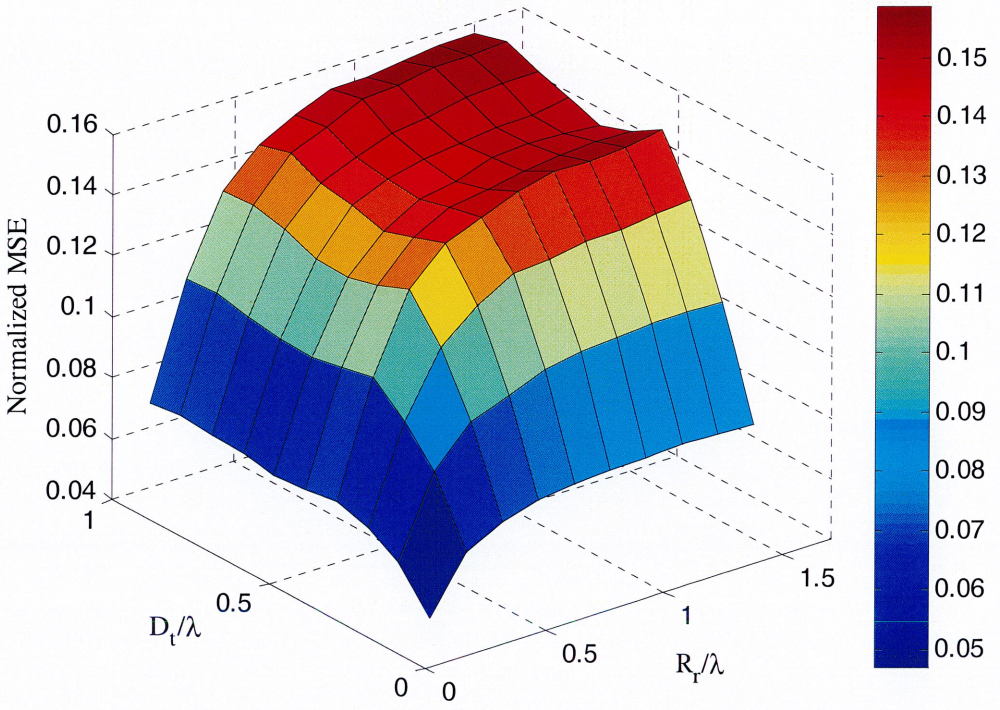


Fig. 5.9 Normalized MSE of the LMMSE channel estimator with optimal training for UCA-MIMO receiver at $\theta_r = 90^o$, SNR=10 dB and $\sigma = 20^o$.

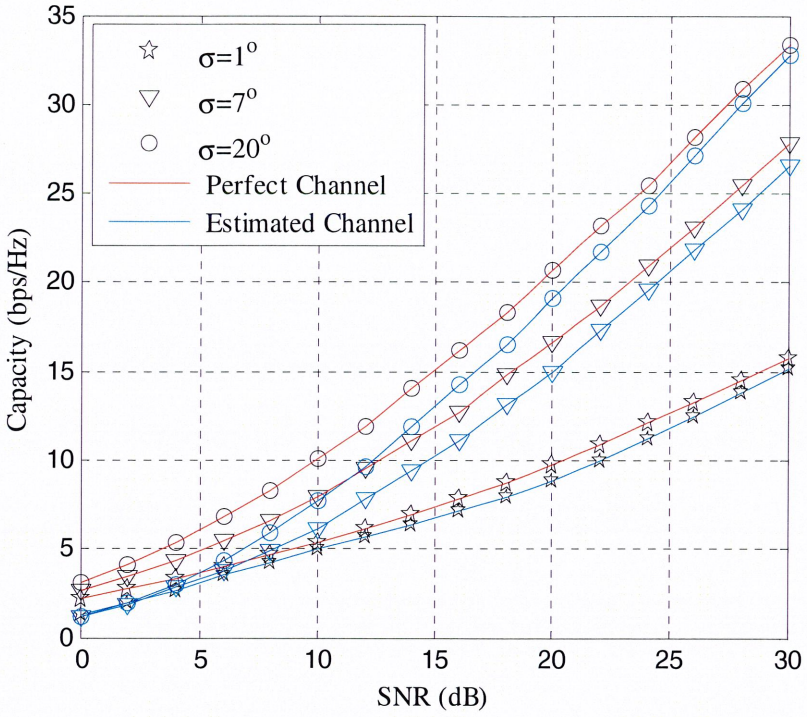


Fig. 5.10 Capacity of UCA-MIMO channel with LMMSE estimator versus SNR at θ_r=90° and different AS.

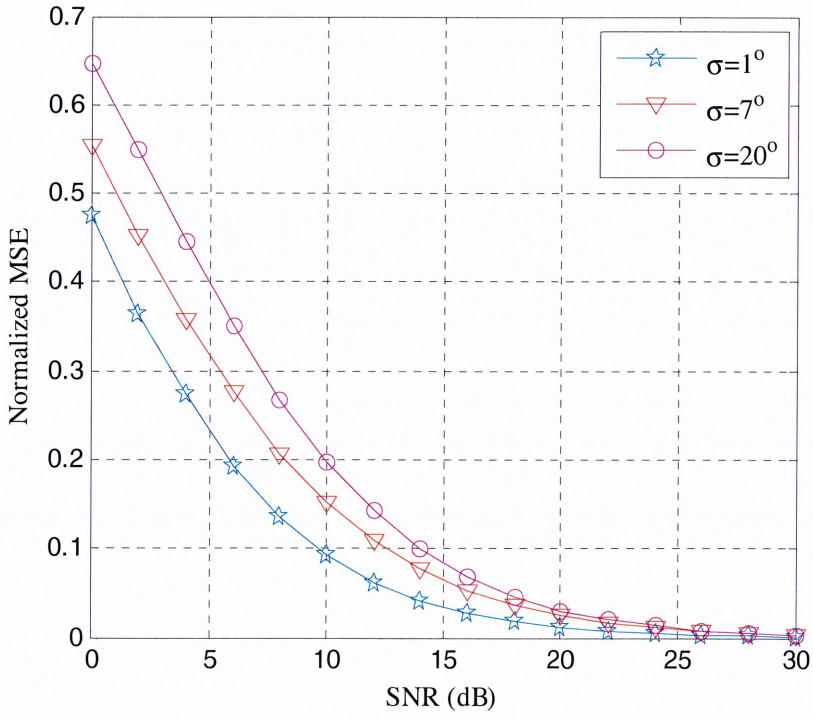


Fig. 5.11 Normalized MSE of LMMSE estimator versus SNR for UCA-MIMO receiver at θ_r=90° and different AS.

5.3 Conclusion

In this chapter, the data-aided training based channel estimation method was studied. The LS, SLS, LMMSE, and RMMSE channel estimators were demonstrated. Optimal training symbols are derived for the LS, SLS, and LMMSE. The results confirmed that the SLS, LMMSE, and RMMSE methods offer better performance than the LS. This is for the reason of utilizing the channel correlation that reduces the channel estimation error in the previous methods, while the LS method does not consider the channel properties. Moreover, the results revealed the superiority of the LMMSE over the other methods. However, it requires more *prior* knowledge about the channel than the other methods. The SLS and RMMSE necessitate less *prior* knowledge about the channel than the LMMSE estimator. So, by compromising the achieved performance these estimators provide a good tradeoff between the performance and the required channel knowledge. In addition, the presented results confirmed that the higher SNR can help to improve the channel accuracy. Also, the impact of channel spatial correlation on the accuracy of MIMO channel estimation was investigated. The undertaken analysis revealed that at low SNR the strongly correlated channel improves the channel estimation. However, at high SNR the channel spatial correlation has less effect pronounced on the accuracy of the channel estimation. Furthermore, the results showed that the performance of the channel estimation gets worse as angle spread increases, which means that a small spatial correlation undermines channel estimation quality. Moreover, the results revealed that the MSE in general is more affected by the AOA in the ULA unlike the UCA. In addition the performances of the ULA and UCA are identical near broadside of the ULA array. Also, the ULA outperforms the UCA at endfire angle .So, the best channel estimation can be achieved with the ULA system at endfire angle. Therefore, it is shown that ULA minimizes the MSE at moderate and low SNR and the performance is further improved with the channel spatial correlation.

Chapter 6

Conclusion and Future Work

This thesis examined the effects of fading correlation on the channel capacity and the performance of MIMO systems under different channel conditions. The aim was to develop a spatial temporal channel models that can be used in the simulation of different MIMO system configurations in particular for IEEE802.11*n* WLANs. In this chapter, Conclusions driven from the numerical results of this thesis are presented in Section 6.1. Some suggestions for future work are recommended in Section 6.2. The publications of this thesis are listed in Section 6.3.

6.1 Conclusions

The main focus of this thesis was to develop a realistic channel model that can fully characterize the fading correlation properties of a wireless environment. Thus, two channel models were utilized in the simulation of MIMO systems. The first channel model is a stochastic spatial clustered (SSC) channel model. The SSC channel model is a correlation-based analytical model which describes different spatial conditions about scatterers in the propagation environment and antenna geometry. In this model, the groups of scatterers are modeled as multi-clusters located around the antenna arrays. Three different Power Azimuth Spectrum (PAS) were assumed with uniform, truncated Gaussian and truncated Laplacian distributions. This model was presented in Sections 2.4 for ULA and UCA geometries. The second model is a more realistic channel model was demonstrated in Chapter 3. A modification to IEEE 802.11*n* channel model was proposed to consider the application of using the UCA configurations in MIMO WLAN systems. Realistic spatial-temporal clustered

(STC) channel model was developed and includes the fading correlation for six (A-F) different environments profiles. Each profile is distinguished by its predefined parameters such as the number of clusters, number of taps within each cluster, power delay profile of the taps, and angle of incidence of each tap. Also, the objective was to investigate the effects of fading correlation on the performance of MIMO systems. These effects were studied on the channel capacity of the IEEE 802.11*n* utilizing the developed STC channel model, the decoding performance of the spatial multiplexing MIMO system and the channel estimation accuracy. The conclusions were driven from the numerical analysis are presented as follows:

Firstly, the capacity performance of the IEEE 802.11*n* channel models was investigated in different WLAN environments utilizing the developed STC channel model. The capacity dependence on the used ULA or UCA geometry was studied. Four antenna configuration combinations were considered "ULA, ULA", "ULA, UCA", "UCA, ULA" and "UCA, UCA". For each combination "X, Y", "X" represents the antenna geometry of the transmitter and "Y" refer to the antenna configuration of the receiver. Thus, in downlink, "ULA, UCA" means that the AP transmitter uses a ULA and STA receiver uses a UCA. To have a fair comparison, configurations were assumed to have identical maximum aperture dimension in all examples. The result was shown that for models 'A', 'D' and 'F' the four antenna configurations experience almost the same capacity. For model 'B' the highest capacity can be achieved by utilizing "UCA, UCA" configuration. For model 'C' the maximum capacity can be attained from "ULA, UCA" and "UCA, UCA" configurations. For model 'E' the highest capacity can be achieved by applying "UCA, ULA" and "UCA, UCA" configurations. From these findings, it can be concluded that for each particular channel profile out of the six environments, there is an optimal configuration that maximizes the channel capacity. In addition, the capacity in models 'B', 'C' and 'E' are affected by the antenna configurations. Whereas, in models 'A', 'D' and 'F' the capacity does not affected by the antenna configurations. Furthermore, it can be seen that the "UCA, UCA" configuration can maximize the channel capacity in all environments. In addition, the channel capacity was evaluated versus receiver radius for 4×4 "UCA, UCA" MIMO system applying the six models. The result was shown that model 'A' experiences the minimum capacity since it has only one tap. While, the maximum capacity can be achieved by model 'F' due to the high number of clusters and multipath components that are included in model 'F'. Also, the capacity dependence on the azimuth rotating of the receiver configuration (orientation of STA) with

respect to different channel models was studied for "ULA, ULA" and "UCA, UCA" systems. It was found that, the variations range of capacity for "ULA, ULA" MIMO configuration over various orientations of the array geometry and with different channel conditions are higher than that for "UCA, UCA" MIMO configuration under the same assumptions. This effect gives a privilege to the use of UCA receiver. The results showed that for model 'A' ULA configuration, since the model 'A' has only one tap at angle of arrival (AOA) = 45^{o}, then by rotating the ULA by 45^{o} the signal will impinge the array from the endfire direction. In this case the correlation will be maximum and the capacity is minimum. In contrary, if the ULA was rotated by 135^{o}, the capacity is maximum because in this case the signal arrives at the broadside of the array. Also, it was observed that the capacity of model 'F' is almost constant and it has the highest values for both configurations. As well, the capacity of various models was investigated at different number of receiver antennas for 4×4 "UCA, UCA" system. The result was shown that as the number of receiver antennas increases, the capacity values are more affected by the model selection. This indicates that, the environment profile should be carefully modeled and selected whenever capacity investigations are performed in particular for higher order MIMO. Moreover, the line of sight (LOS) conditions was examined for 4×4 "UCA, UCA" system by assuming that the LOS component is included if the separation between the transmitter AP and the receiver STA is within the breakpoint distance. The LOS is configured by adding a standard Ricean K-factor reported in [11] to the first tap while all the other taps K-factor remain at $-\infty$ dB as in IEEE 802.11*n* model. The result was shown that the LOS component degrades the channel capacity in all models. It was found that in NLOS conditions, capacity improves by 20% compared to the case where LOS component included. The improvement is less pronounced for model 'F' than other models due to its many multipath taps thus the effect of the 1^{st} LOS tap will be less significant. Furthermore, both uniform and water-poring power allocation schemes were simulated for 4×4 "UCA, UCA" system and it was found that the capacity of water-pouring power allocation scheme is superior to the one achieved with uniform power strategy specifically for low SNRs. Besides, at low SNR the capacity of the models with water-pouring power allocation scheme is greater than the one achieved by the uncorrelated channel with uniform power allocation strategy.

Secondly, the V-BLAST architecture and detection algorithms were presented and compared for different antenna array geometries using various channel models. The principles of V-BLAST detection including the sub-optimal methods and maximum likelihood (ML) optimal

scheme were studied. The sub-optimal techniques that were considered in this work are linear signal detection with either zero forcing (ZF) or minimum mean square error (MMSE), successive interference cancellation (SIC) and parallel interference cancellation (PIC). Simulation results confirmed that the ordered SIC (OSIC) scheme with MMSE nulling criteria yields the best bit error rate performance over other suboptimal schemes. However, it suffers from several disadvantages such as it needs for power reordering at each stage of detection and the number of stages is required to be increased as the number of transmit antennas increases. Therefore, the PIC could be used as an alternative choice since it has a slightly less performance of OSIC. Meanwhile, it does not require any power reordering and it has reduced system delay. Moreover, the impact of channel spatial correlation on the 4×4 V-BLAST system based on the OSIC scheme with MMSE nulling criteria and QPSK modulation was investigated for both ULA and UCA geometries. SSC channel model was considered in the simulation of this spatial multiplexed MIMO system. The results was shown that the central angle of arrival (AOA) and the angular spread (AS) has a significant impact on the BER performance of both the UCA and ULA. It was found that the UCA outperforms the ULA when the AOAs are near end-fire angels. However, both geometries give nearly similar performance when AOAs are near the broadside angles of ULA. Furthermore, the worst performance for system employing ULA can be occurred when angle of arrivals are equal to the end-fire angles. Given that, all elements are in-line with the central angle of arrival that leads to high correlation between elements. However, the worst performance for UCA was found to be at angle of arrivals 45^{o} and 135^{o}. In these cases, the correlation is high because elements three and four are directly behind elements one and two. It is noted that the worst case value and the variations of BER in the UCA case is less than the ULA case, in particular for high AS. For example, the performance of UCA is higher than the performance of ULA by about one order of magnitude at AOA endfire angle and AS=20^{o} with similar aperture size. Furthermore, V-BLAST system BER performance was investigated under realistic STC channel model that applies the IEEE802.11*n* channel scenarios utilizing UCA antennas at both ends. The results showed that with a proper selection of UCA radius and number of elements the performance of uncorrelated channel can be achieved. In addition, it was shown that the best performance can be achieved by model 'F' profile of IEEE802.11*n* channel model, which is a simulation of large space indoor environment conditions.

Finally, the data-aided training based channel estimation method was studied. The LS, SLS, LMMSE, and RMMSE channel estimators were demonstrated. The Optimal training symbols

were presented for the LS, SLS, and LMMSE estimators. The results confirmed that the SLS, LMMSE, and RMMSE methods offer better performance than the LS. This is for the reason of utilizing the channel correlation that reduces the channel estimation error in the previous methods, while the LS method does not consider the channel properties. Moreover it was revealed the superiority of the LMMSE over the other methods. However, it requires more *prior* knowledge about the channel than the other methods. The SLS and RMMSE necessitate less *prior* knowledge about the channel than the LMMSE estimator. So, by compromising the achieved performance these estimators provide a good tradeoff between the performance and the required channel knowledge. Moreover, the impact of channel spatial correlation on the accuracy of LMMSE Channel estimation was investigated. The undertaken analysis was revealed that at low SNR the strongly correlated channel can improve the accuracy of the channel estimator. However, at high SNR the channel spatial correlation has less pronounced effect on the accuracy of the channel estimator. In addition, the results showed that the performance of the channel estimator for ULA (i.e., experiences higher correlation than the UCA) system is generally better than the UCA system. The mean square error (MSE) of the LMMSE channel estimator was studied as a function of AOA at various SNR (high, moderate and low) values. The results were shown that at high SNR the MSE is improved, but the spatial correlation has a less pronounced effect on improving the channel estimation error. In turn, at moderate and low SNR the spatial correlation reduces the channel estimation error. Furthermore, the results revealed that the MSE in general is more affected by the correlation in the ULA unlike the UCA. In addition the performances of the ULA and UCA are identical near broadside of the array. Also, it was shown that the ULA outperforms the UCA at end-fire angle .So, the best channel estimation error can be achieved with the ULA system at end-fire angle (maximum correlation). Therefore, the ULA minimizes the MSE at moderate and low SNR and the performance is further improved with the channel spatial correlation.

6.2 Future Work

This section describes some possible extensions to the research presented in this thesis.

- In this thesis, it was shown that the antenna array configuration has a significant effect on spatial correlation properties of MIMO wireless communications channels. The effects of antenna configuration on the performance of a MIMO system were

investigated for ULA and UCA geometries. For future work a larger angular views antenna array can be chosen like hexagonal, rectangular, cubic, and triangular.

- The work presented in this thesis only focused on the impact of fading correlation on the performance of a MIMO system. For future work the effect of antenna mutual coupling on the performance of a MIMO system could be investigated.

- In this thesis, the accuracy of different training-based channel estimation methods was investigated. Further investigations are needed to evaluate the capacity and BER performance with the impact of channel estimation errors. In addition, the blind and semi blind channel estimation techniques could be considered.

- The work presented in this thesis was based on the collocated MIMO technique, where the antennas are packed together with spacing on the order of a wavelength. As seen in this research the benefits of the collocated MIMO are limited due to the fading correlation and terminal size limitation (number of antennas). To mitigate the drawbacks in collocated MIMO system, a new technique named distributed MIMO was proposed and has attracted much attention. The major difference between the distributed and collocated MIMO is that multiple antennas at the front end of wireless systems are distributed among widely separated radio nodes. For future it is of great interest to study the distributed MIMO technique.

6.3 Publication List

The materials of this thesis have been published as listed below:

1. M. A. Mangoud, Z. Mahdi; "Link Evaluation of WLAN MIMO Systems Employing Uniform Circular Array Under Realistic Channel Conditions" Proceeding of the 12th IEEE International Conference on Communication Systems (IEEE ICCS 2010), 17-19 Nov 2010, Singapore.

2. Z. Mahdi, M. A. Mangoud; "Temporal and Spatial Realistic Clustered Channel Model for Circular Array Based Wideband WLAN MIMO Systems", Proceeding of the 6th IEEE GCC Conference & Exhibition, "For Sustainable Ubiquitous Technology", 19-22 February 2011, Dubai, UAE. **(Best student paper award)**

3. M. A. Mangoud, Z. Mahdi; "Spatial Correlation Effects on Channel Estimation of UCA-MIMO Receivers" Proceeding of the 2011 International Conference on Communication Engineering and Networks (ICCEN 2011) November 25-27, 2011, Hong Kong.

4. M. A. Mangoud, Z. Mahdi; "Effect of Fading Correlation on the VBLAST Detection of UCA-MIMO systems" Submitted for publication

5. M. A. Mangoud and Z. Mahdi "Realistic Spatio-Temporal Channel Model for Broadband MIMO WLAN Systems Employing Uniform Circular Antenna Arrays" Applied Computational Electromagnetics Society Journal (ACES), ISSN: 1054-4887, May 2011, Vol. 26, No. 5.

Appendix A

IEEE 802.11*n* Channel Models

Model 'A'

	Tap index	**1**
	Excess delay [ns]	**0**
Cluster 1	**Power [dB]**	0
AOA	**AOA [°]**	45
AS	**AS [°]**	40
AOD	**AOD [°]**	45
AS	**AS [°]**	40

Model 'B'

	Tap index	1	2	3	4	5	6	7	8	9
	Excess delay [ns]	**0**	**10**	**20**	**30**	**40**	**50**	**60**	**70**	**80**
Cluster 1	**Power [dB]**	0	-5.4	-10.8	-16.2	-21.7				
AOA	**AOA [°]**	290.3	290.3	290.3	290.3	290.3				
AS	**AS [°]**	24.6	24.6	24.6	24.6	24.6				
AOD	**AOD [°]**	13.5	13.5	13.5	13.5	13.5				
AS	**AS [°]**	24.7	24.7	24.7	24.7	24.7				
Cluster 2	**Power [dB]**			-3.2	-6.3	-9.4	-12.5	-15.6	-18.7	-21.8
AOA	**AOA [°]**			118.4	118.4	118.4	118.4	118.4	118.4	118.4
AS	**AS [°]**			25.2	25.2	25.2	25.2	25.2	25.2	25.2
AOD	**AOD [°]**			106.5	106.5	106.5	106.5	106.5	106.5	106.5
AS	**AS [°]**			25.4	25.4	25.4	25.4	25.4	25.4	25.4

Model 'C'

	Tap index	1	2	3	4	5	6	7	8	9	10	11	12	13	14
	Excess delay [ns]	0	10	20	30	40	50	60	70	80	90	110	140	170	200
Cluster 1	Power [dB]	0	-2.1	-4.3	-6.5	-8.6	-10.8	-13.0	-15.2	-17.3	-19.5				
AOA	AOA [°]	290.3	290.3	290.3	290.3	290.3	290.3	290.3	290.3	290.3	290.3				
AS	AS [°]	24.6	24.6	24.6	24.6	24.6	24.6	24.6	24.6	24.6	24.6				
AOD	AOD [°]	13.5	13.5	13.5	13.5	13.5	13.5	13.5	13.5	13.5	13.5				
AS	AS [°]	24.7	24.7	24.7	24.7	24.7	24.7	24.7	24.7	24.7	24.7				
Cluster 2	Power [dB]							-5.0	-7.2	-9.3	-11.5	-13.7	-15.8	-18.0	-20.2
AOA	AOA [°]							332.3	332.3	332.3	332.3	332.3	332.3	332.3	332.3
AS	AS [°]							22.4	22.4	22.4	22.4	22.4	22.4	22.4	22.4
AOD	AOD [°]							56.4	56.4	56.4	56.4	56.4	56.4	56.4	56.4
AS	AS [°]							22.5	22.5	22.5	22.5	22.5	22.5	22.5	22.5

Model 'D'

	Tap index	1	2	3	4	5	6	7	8	9	10	11	12	13	14	15	16	17	18
	Excess delay [ns]	0	10	20	30	40	50	60	70	80	90	110	140	170	200	240	290	340	390
Cluster 1	Power [dB]	0	-0.9	-1.7	-2.6	-3.5	-4.3	-5.2	-6.1	-6.9	-7.8	-9.0	-11.1	-13.7	-16.3	-19.3	-23.2		
AOA	AOA [°]	158.9	158.9	158.9	158.9	158.9	158.9	158.9	158.9	158.9	158.9	158.9	158.9	158.9	158.9	158.9	158.9		
AS	AS [°]	27.7	27.7	27.7	27.7	27.7	27.7	27.7	27.7	27.7	27.7	27.7	27.7	27.7	27.7	27.7	27.7		
AOD	AOD [°]	332.1	332.1	332.1	332.1	332.1	332.1	332.1	332.1	332.1	332.1	332.1	332.1	332.1	332.1	332.1	332.1		
AS	AS [°]	27.4	27.4	27.4	27.4	27.4	27.4	27.4	27.4	27.4	27.4	27.4	27.4	27.4	27.4	27.4	27.4		
Cluster 2	Power [dB]											-6.6	-9.5	-12.1	-14.7	-17.4	-21.9	-25.5	
AOA	AOA [°]											332.3	332.3	332.3	332.3	332.3	332.3	332.3	
AS	AS [°]											22.4	22.4	22.4	22.4	22.4	22.4	22.4	
AOD	AOD [°]											56.4	56.4	56.4	56.4	56.4	56.4	56.4	
AS	AS [°]											22.5	22.5	22.5	22.5	22.5	22.5	22.5	
Cluster 3	Power [dB]															-18.8	-23.3	-25.2	-26.7
AOA	AOA [°]															276.1	276.1	276.1	276.1
AS	AS [°]															37.4	37.4	37.4	37.4
AOD	AOD [°]															275.9	275.9	275.9	275.9
AS	AS [°]															36.8	36.8	36.8	36.8

Model E (1/2)

	Tap index	1	2	3	4	5	6	7	8	9	10	11	12	13	14	15	16	17	18
	Excess delay [ns]	0	10	20	30	50	80	110	140	180	230	280	330	380	430	490	560	640	730
Cluster 1	Power [dB]	-2.6	3.0	-3.5	-3.9	-4.5	-5.6	-6.9	-8.2	-9.8	-11.7	-13.9	-16.1	-18.3	-20.5	-22.9			
AOA	AOA [°]	163.7	163.7	163.7	163.7	163.7	163.7	163.7	163.7	163.7	163.7	163.7	163.7	163.7	163.7	163.7			
AS	AS [°]	35.8	35.8	35.8	35.8	35.8	35.8	35.8	35.8	35.8	35.8	35.8	35.8	35.8	35.8	35.8			
AOD	AOD [°]	105.6	105.6	105.6	105.6	105.6	105.6	105.6	105.6	105.6	105.6	105.6	105.6	105.6	105.6	105.6			
AS	AS [°]	36.1	36.1	36.1	36.1	36.1	36.1	36.1	36.1	36.1	36.1	36.1	36.1	36.1	36.1	36.1			
Cluster 2	Power [dB]					-1.8	-3.2	-4.5	-5.8	-7.1	-9.9	-10.3	-14.3	-14.7	-18.7	-19.9	-22.4		
AOA	AOA [°]					251.8	251.8	251.8	251.8	251.8	251.8	251.8	251.8	251.8	251.8	251.8	251.8		
AS	AS [°]					41.6	41.6	41.6	41.6	41.6	41.6	41.6	41.6	41.6	41.6	41.6	41.6		
AOD	AOD [°]					293.1	293.1	293.1	293.1	293.1	293.1	293.1	293.1	293.1	293.1	293.1	293.1		
AS	AS [°]					42.5	42.5	42.5	42.5	42.5	42.5	42.5	42.5	42.5	42.5	42.5	42.5		

Model E (2/2)

	Tap index	1	2	3	4	5	6	7	8	9	10	11	12	13	14	15	16	17	18
	Excess delay [ns]	0	10	20	30	50	80	110	140	180	230	280	330	380	430	490	560	640	730
Cluster 3	Power [dB]									-7.9	-9.6	-14.2	-13.8	-18.6	-18.1	-22.8			
AOA	AOA [°]									80.0	80.0	80.0	80.0	80.0	80.0	80.0			
AS	AS [°]									37.4	37.4	37.4	37.4	37.4	37.4	37.4			
AOD	AOD [°]									61.9	61.9	61.9	61.9	61.9	61.9	61.9			
AS	AS [°]									38.0	38.0	38.0	38.0	38.0	38.0	38.0			
Cluster 4	Power [dB]															-20.6	-20.6	-20.6	-20.6
AOA	AOA [°]															182.0	182.0	180.2	180.2
AS	AS [°]															40.3	40.3	40.3	40.3
AOD	AOD [°]															275.7	275.7	275.7	275.7
AS	AS [°]															38.7	38.7	38.7	38.7

Model F (1/2)

	Tap index	1	2	3	4	5	6	7	8	9	10	11	12	13	14	15	16	17	18
	Excess delay [ns]	0	10	20	30	50	80	110	140	180	230	280	330	400	490	600	730	880	1050
Cluster 1	Power [dB]	-3.3	-3.6	-3.9	-4.2	-4.6	-5.3	-6.2	-7.1	-8.2	-9.5	-11.0	-12.5	-14.3	-16.7	-19.9			
AOA	AOA [°]	315.1	315.1	315.1	315.1	315.1	315.1	315.1	315.1	315.1	315.1	315.1	315.1	315.1	315.1	315.1			
AS	AS [°]	48..0	48..0	48..0	48..0	48..0	48..0	48..0	48..0	48..0	48..0	48..0	48..0	48..0	48..0	48..0			
AOD	AOD [°]	56.2	56.2	56.2	56.2	56.2	56.2	56.2	56.2	56.2	56.2	56.2	56.2	56.2	56.2	56.2			
AS	AS [°]	41.6	41.6	41.6	41.6	41.6	41.6	41.6	41.6	41.6	41.6	41.6	41.6	41.6	41.6	41.6			
Cluster 2	Power [dB]					-1.8	-2.8	-3.5	-4.4	-5.3	-7.4	-7.0	-10.3	-10.4	-13.8	-15.7	-19.9		
AOA	AOA [°]					180.4	180.4	180.4	180.4	180.4	180.4	180.4	180.4	180.4	180.4	180.4	180.4		
AS	AS [°]					55.0	55.0	55.0	55.0	55.0	55.0	55.0	55.0	55.0	55.0	55.0	55.0		
AOD	AOD [°]					183.7	183.7	183.7	183.7	183.7	183.7	183.7	183.7	183.7	183.7	183.7	183.7		
AS	AS [°]					55.2	55.2	55.2	55.2	55.2	55.2	55.2	55.2	55.2	55.2	55.2	55.2		
Cluster 3	Power [dB]									-5.7	-6.7	-10.4	-9.6	-14.1	-12.7	-18.5			
AOA	AOA [°]									74.7	74.7	74.7	74.7	74.7	74.7	74.7			
AS	AS [°]									42.0	42.0	42.0	42.0	42.0	42.0	42.0			
AOD	AOD [°]									153.0	153.0	153.0	153.0	153.0	153.0	153.0			
AS	AS [°]									47.4	47.4	47.4	47.4	47.4	47.4	47.4			

Model F (2/2)

	Tap index	1	2	3	4	5	6	7	8	9	10	11	12	13	14	15	16	17	18
	Excess delay [ns]	0	10	20	30	50	80	110	140	180	230	280	330	400	490	600	730	880	1050
Cluster 4	Power [dB]													-8.8	-13.3	-18.7			
AOA	AOA [°]													251.5	251.5	251.5			
AS	AS [°]													28.6	28.6	28.6			
AOD	AOD [°]													112.5	112.5	112.5			
AS	AS [°]													27.2	27..2	27.2			
Cluster 5	Power [dB]															-12.9	-14.2		
AOA	AOA [°]															68.5	68.5		
AS	AS [°]															30.7	30.7		
AOD	AOD [°]															291.0	291.0		
AS	AS [°]															33.0	33.0		
Cluster 6	Power [dB]																	-16.3	-21.2
AOA	AOA [°]																	246.2	246.2
AS	AS [°]																	38.2	38.2
AOD	AOD [°]																	62.3	62.3
AS	AS [°]																	38.0	38.0

Appendix B

Numerical Examples of Ordered SIC and PIC Detection Techniques

8.1 Ordered SIC

To become conscious with the ordered SIC scheme, the V-BLAST algorithm based on ZF criteria is demonstrated numerically. Consider a MIMO channel with $(M_r, M_t) = (3,3)$ with QPSK constellation $A = \left\{\pm\frac{1}{\sqrt{2}} \pm j\frac{1}{\sqrt{2}}\right\}$. Suppose $\sigma_n^2 = 2.5$, $\sqrt{\frac{E_a}{M_t}} = 10$, The realization of channel transfer matrix is

$$\mathbf{H} = \begin{bmatrix} 0.3 - j0.6 & -0.2 + j0.2 & 0.6 - j1.2 \\ 0.7 - j2.1 & 0.2 - j0.5 & -0.8 - j0.1 \\ 0.5 + j & -0.6 + j & -0.8 - j0.2 \end{bmatrix}$$

$\boldsymbol{a} = \left[\frac{1}{\sqrt{2}} + j\frac{1}{\sqrt{2}}, \frac{1}{\sqrt{2}} - j\frac{1}{\sqrt{2}}, \frac{1}{\sqrt{2}} + j\frac{1}{\sqrt{2}}\right]^T$ and $\mathbf{n} = [0.4 - j0.03\ ,0.4 - j0.2, -1 + j0.7]^T$

The received vector $\mathbf{r}_1$ is

$$\mathbf{r}_1 = \sqrt{\frac{E_a}{M_t}}\mathbf{H}\boldsymbol{a} + \mathbf{n} = \begin{bmatrix} 6.6 - j0.8 \\ 4.2 - j6.8 \\ -2.5 + j5.4 \end{bmatrix}$$

The weight matrix of the ZF is computed as

$$\mathbf{W}_1 = \sqrt{\frac{M_t}{E_a}}\mathbf{H}^{\dagger} = \begin{bmatrix} j0.1 & 0.1+j0.1 & -0.9+j0.4 & 0.1 \\ -j0.2 & -0.1+j0.1 & 0.5+j0.3 & -0.2-j0.1 \\ 0.1+j0.1 & -0.1 & 0.5 & -0.1-j0.1 \end{bmatrix}$$

Since there are three components of $\boldsymbol{a}$, SIC algorithm completes the decision process after 3 iterations as follows:

Step 1: In the first layer, the 1^{st} sub-channel is preferred, $k_1 = 1$, since

$$\|(\mathbf{W}_1)_1\|^2 = 0.03$$
$$\|(\mathbf{W}_1)_2\|^2 = 0.12$$
$$\|(\mathbf{W}_1)_3\|^2 = 0.04$$

The first estimated component is calculated according to (4.15d) as

$$y_1 = [j0.1 \quad 0.1+j0.1 \quad -0.9+j0.4 \quad 0.1]\begin{bmatrix} 6.6-j0.8 \\ 4.2-j6.8 \\ -2.5+j5.4 \end{bmatrix} = 0.68+j0.8$$

This estimate is sliced by (4.15e); hence, the decision for the first component would be

$$\hat{a}_1 = \frac{1}{\sqrt{2}} + j\frac{1}{\sqrt{2}}$$

After symbol cancellation described in (4.15f), the modified received vector is

$$\mathbf{r}_2 = \mathbf{r}_1 - \hat{a}_1(\mathbf{H})_1 = \begin{bmatrix} 5.9-j0.7 \\ 2.3-j5.9 \\ -2.1+j4.3 \end{bmatrix}$$

The matrix $\mathbf{H}_{\bar{1}}$ equals

$$\mathbf{H}_{\bar{1}} = \begin{bmatrix} -0.2+j0.2 & 0.6-j1.2 \\ 0.2-j0.5 & -0.8-j0.1 \\ -0.6+j & -0.8-j0.2 \end{bmatrix}$$

The new weight matrix $\mathbf{W}_2$ for next iteration is computed to be

$$\mathbf{W}_2 = \sqrt{\frac{M_t}{E_a}}\mathbf{H}^{\dagger}_{\bar{1}} = \begin{bmatrix} -j0.04 & j0.1 & -0.1-j0.2 \\ 0.1+j0.1 & -0.1+j0.02 & -0.1-j0.02 \end{bmatrix}$$

Step 2: In the second layer, algorithm chooses the 3^{rd} sub-channel to process, $k_2 = 3$, since

$$\|(\mathbf{W}_2)_2\|^2 = 0.06$$
$$\|(\mathbf{W}_2)_3\|^2 = 0.03$$

Therefore, estimate y_3 is

$$y_3 = [0.1 + j0.1 \quad -0.1 + j0.02 \quad -0.1 - j0.02]\begin{bmatrix} 5.9 - j0.7 \\ 2.3 - j5.9 \\ -2.1 + j4.3 \end{bmatrix} = 0.6 + j1.1$$

and the decision $\hat{a}_3$ is

$$\hat{a}_3 = \frac{1}{\sqrt{2}} + j\frac{1}{\sqrt{2}}$$

After cancellation, the modified received vector is calculated to be

$$\mathbf{r}_3 = \mathbf{r}_2 - \hat{a}_3(\mathbf{H})_3 = \begin{bmatrix} 4.6 - j0.3 \\ 2.8 - j5.3 \\ -1.7 + j5 \end{bmatrix}$$

The matrix $\mathbf{H}_{\bar{3}}$ equals

$$\mathbf{H}_{\bar{3}} = \begin{bmatrix} -0.2 + j0.2 \\ 0.2 - j0.5 \\ -0.6 + j \end{bmatrix}$$

and the new weight matrix $\mathbf{W}_3$ is

$$\mathbf{W}_3 = \sqrt{\frac{M_t}{E_a}}\mathbf{H}^{\dagger}_{\bar{3}} = [0.04 - j0.04 \quad 0.4 + j0.1 \quad -0.1 - j0.2]$$

Step 3: In the last layer, the estimate y_2 is calculated as

$$y_2 = [0.04 - j0.04 \quad 0.4 + j0.1 \quad -0.1 - j0.2]\begin{bmatrix} 4.6 - j0.3 \\ 2.8 - j5.3 \\ -1.7 + j5 \end{bmatrix} = 1.5 - j0.3$$

and the corresponding decision $\hat{a}_2$ is

$$\hat{a}_2 = \frac{1}{\sqrt{2}} - j\frac{1}{\sqrt{2}}$$

Finally, the components of the decision vector are combined according to the order of indices (k_1, k_2, k_3), which yields

$$\hat{\boldsymbol{a}} = \begin{bmatrix} \frac{1}{\sqrt{2}} + j\frac{1}{\sqrt{2}} \\ \frac{1}{\sqrt{2}} - j\frac{1}{\sqrt{2}} \\ \frac{1}{\sqrt{2}} + j\frac{1}{\sqrt{2}} \end{bmatrix}$$

which is the correct estimate of $\boldsymbol{a}$.

8.2 PIC

To comprehend the PIC scheme, its algorithm based on ZF criteria is demonstrated numerically using the same considerations of the preceding example. The output of the first stage detection according to (4.16a) is given by

$$\tilde{\boldsymbol{a}} = (\mathbf{W}_{ZF}\mathbf{r}) = \begin{bmatrix} 0.7 + j0.8 \\ 1 - j0.7 \\ 0.8 + j0.8 \end{bmatrix} = \begin{bmatrix} \frac{1}{\sqrt{2}} + j\frac{1}{\sqrt{2}} \\ \frac{1}{\sqrt{2}} - j\frac{1}{\sqrt{2}} \\ \frac{1}{\sqrt{2}} + j\frac{1}{\sqrt{2}} \end{bmatrix}$$

Next, in accordance to (4.16b) the auxiliary symbol vectors are

$$\tilde{\boldsymbol{a}}_1 = \boldsymbol{J}_1\tilde{\boldsymbol{a}} = \begin{bmatrix} 0 & 0 & 0 \\ 0 & 1 & 0 \\ 0 & 0 & 1 \end{bmatrix} \begin{bmatrix} \frac{1}{\sqrt{2}} + j\frac{1}{\sqrt{2}} \\ \frac{1}{\sqrt{2}} - j\frac{1}{\sqrt{2}} \\ \frac{1}{\sqrt{2}} + j\frac{1}{\sqrt{2}} \end{bmatrix} = \begin{bmatrix} 0 \\ \frac{1}{\sqrt{2}} - j\frac{1}{\sqrt{2}} \\ \frac{1}{\sqrt{2}} + j\frac{1}{\sqrt{2}} \end{bmatrix}$$

$$\tilde{\boldsymbol{a}}_2 = \boldsymbol{J}_2\tilde{\boldsymbol{a}} = \begin{bmatrix} 1 & 0 & 0 \\ 0 & 0 & 0 \\ 0 & 0 & 1 \end{bmatrix} \begin{bmatrix} \frac{1}{\sqrt{2}} + j\frac{1}{\sqrt{2}} \\ \frac{1}{\sqrt{2}} - j\frac{1}{\sqrt{2}} \\ \frac{1}{\sqrt{2}} + j\frac{1}{\sqrt{2}} \end{bmatrix} = \begin{bmatrix} \frac{1}{\sqrt{2}} + j\frac{1}{\sqrt{2}} \\ 0 \\ \frac{1}{\sqrt{2}} + j\frac{1}{\sqrt{2}} \end{bmatrix}$$

$$\tilde{\boldsymbol{a}}_3 = \boldsymbol{J}_3\tilde{\boldsymbol{a}} = \begin{bmatrix}1 & 0 & 0\\ 0 & 1 & 0\\ 0 & 0 & 0\end{bmatrix}\begin{bmatrix}\frac{1}{\sqrt{2}}+j\frac{1}{\sqrt{2}}\\ \frac{1}{\sqrt{2}}-j\frac{1}{\sqrt{2}}\\ \frac{1}{\sqrt{2}}+j\frac{1}{\sqrt{2}}\end{bmatrix} = \begin{bmatrix}\frac{1}{\sqrt{2}}+j\frac{1}{\sqrt{2}}\\ \frac{1}{\sqrt{2}}+j\frac{1}{\sqrt{2}}\\ 0\end{bmatrix}$$

Then, the auxiliary receive vectors are formed from the auxiliary symbol vectors

$$\tilde{\mathbf{r}}_1 = \mathbf{r} - \mathbf{H}\tilde{\boldsymbol{a}}_1 = \begin{bmatrix}5.2-j0.8\\ 5-j5.7\\ -2.4+j5\end{bmatrix}$$

$$\tilde{\mathbf{r}}_2 = \mathbf{r} - \mathbf{H}\tilde{\boldsymbol{a}}_2 = \begin{bmatrix}4.6-j0.3\\ 2.8-j5.3\\ -1.7+j5\end{bmatrix}$$

$$\tilde{\mathbf{r}}_3 = \mathbf{r} - \mathbf{H}\tilde{\boldsymbol{a}}_3 = \begin{bmatrix}5.9-j\\ 2.5-j5.4\\ -2.4+j3.3\end{bmatrix}$$

Finally, the transmitted symbols are estimated in compliance to (4.16d)

$$\hat{a}_1 = (\mathbf{H}^+{}_1\tilde{\mathbf{r}}_1)$$

$$\hat{a}_1 = \left([0.05+j0.1 \quad 0.1+j0.3 \quad 0.1-j0.2]\begin{bmatrix}5.2-j0.8\\ 5-j5.7\\ -2.4+j5\end{bmatrix}\right)$$

$$\hat{a}_1 = (3.3+j2.1) \quad = \frac{1}{\sqrt{2}}+j\frac{1}{\sqrt{2}}$$

$$\hat{a}_2 = (\mathbf{H}^+{}_2\tilde{\mathbf{r}}_2)$$

$$\hat{a}_2 = \left([-0.1-j0.1 \quad 0.1+j0.3 \quad -0.3-j0.6]\begin{bmatrix}4.6-j0.3\\ 2.8-j5.3\\ -1.7+j5\end{bmatrix}\right)$$

$$\hat{a}_2 = (4.8-j) = \frac{1}{\sqrt{2}}-j\frac{1}{\sqrt{2}}$$

$$\hat{a}_3 = (\mathbf{H}^+{}_3\tilde{\mathbf{r}}_3)$$

$$\hat{a}_3 = \left([0.2+j0.4 \quad -0.3+j0.02 \quad -0.2+j0.05]\begin{bmatrix}5.9-j\\ 2.5-j5.4\\ -2.4+j3.3\end{bmatrix}\right)$$

$$\hat{a}_3 = (1.4+j2.6) = \frac{1}{\sqrt{2}}+j\frac{1}{\sqrt{2}}$$

Bibliography

[1] A. Paulraj, R. Nabar and D. Gore, *Introduction to Space-Time Wireless Communications*, 1st ed. Cambridge, United Kingdom: Cambridge University Press, 2003.

[2] B. Vucetic and J. Yuan, *Space-Time Coding*, 1st ed. Chichester, England: John Wiley & Sons Ltd, 2003.

[3] M. Jankirman, *Space-Time Codes and MIMO Systems*, 1st ed. Boston, London: Artech House, 2004.

[4] V. Tarokh, H. Jafarkhani and A. R. Calderbank, "Space-Time Block Coding for Wireless Communications: Performance Results," *IEEE Journal on Selected Areas in Communications*, vol. 17, no. 3, pp. 451-460, March 1999.

[5] V. Tarokh, N. Seshadri and A.R. Calderbank, "Space-Time Codes for Higher Data Rate Wireless Communications: Performance Criterion and Code Construction," *IEEE Transactions on Information Theory*, vol. 44, no. 2, pp. 744-765, March 1998.

[6] G. J. Foschini, "Layered Space-Time Architecture for Wireless Communications in a Fading Environment When Using Multi-Element Antennas," *Bell Labs Technical Journal*, vol. 1, no. 2, pp. 41-59, 1996.

[7] G. J. Foschini and M. J. Gans, "On Limits of Wireless Communications in a Fading Environments when Using Multiple Antennas," *Wireless Personal Communications*, vol. 6, no. 3, pp. 311-335, 1998.

[8] Da-S. Shiu, G. J. Foschini, M. J. Gans and J. M. Kahn, "Fading Correlation and Its Effect on the Capacity of Multielement Antenna Systems," *IEEE Transactions on Communications*, vol. 48, no. 3, pp. 502-513, March 2000.

[9] J. Salz and J. H. Winters, "Effect of fading correlation on adaptive arrays in digital wireless communications," in *IEEE Conference*, Geneva, 1993, pp. 1768-1774.

[10] A. W. Umrani and D. V. Kishore, "Deterministic simulations of spatial fading correlation for MIMO communication channels," in *IEEE Conference*, Singapore, 2003, pp. 78-83.

[11] IEEE 802.11-03/940r4, "IEEE P802.11 Wireless LANs, TGn Channel Models," May 2004.

[12] M. Biguesh and A. B. Gershman, "Training-Based Channel Estimator: a Study of Estimator Tradeoffs and Optimal Training Signals," *IEEE Transactions on Signal Processing*, vol. 54, no. 3, pp. 884-893, March 2006.

[13] I. E. Telater, "Capacity of Multi-Antenna Gaussian Channels," *European Transactions on Telecommunications*, vol. 10, pp. 585-595, December 1999.

[14] C. C. Martin, J. H. Winters, H. H. Zeng, N. R. Sollenberger and A. Dixit, "Multiple-Input Multiple-Output (MIMO) Radio Channel Measurement and Experimental Implementation for EDGE ," in *Thirty-Fourth Asilomar Conference on Signals, Systems and Computers*, 2000, pp. 738-742.

[15] T. S. Rappaport, *Wireless Communications, Principles and Practice*, 2nd ed.: Prentice Hall PTR, 2002.

[16] Y. S. Cho, J. Kim, W. Y. Yang and C. Kang, *MIMO-OFDM Wireless Communications with MATLAB*, 1st ed. Chichester, United Kingdom: John Wiley & Sons (Asia) Pte Ltd, 2010.

[17] N. Costa and S. Haykin, *Multiple-Input Multiple Output Channel Models, Theory and Practice*, 1st ed. New York: John Wiley & Sons, 2010.

[18] P. Almers, E. Bonek, A. Burr, N. Czink, M. Debbah, V. Degli-Esposti, H. Hofstetter, P. Kyosti, D. Laurenson, G. Matz, A. F. Molisch, C. Oestges and H. Ozcelik, "Survey of Channel and Radio Propagation Models for Wireless MIMO Systems," *Eurasip Journal on Wireless Communications and Networking*, vol. 2007, Artical ID 19070.

[19] R. Verma, S. Mahajan and V. Rohila, "Classification of MIMO Channel Models," in *16th IEEE International Conference on Networks*, 2008, pp. 1-4.

[20] K. shlager and J. Schneider, "A Selective Survey of the finite-difference time-domine literature," *IEEE Antennas Propagation Magazine*, vol. 37, no. 4, pp. 33-56, Aug. 1995.

[21] H. R. Anderson, "A Ray-Tracing Propagation Model for Digital Broadcast System in Urban Areas," *IEEE Transactions on Broadcasing*, vol. 39, no. 3, pp. 309-317, Sep. 1993.

[22] G. J. Byers and F. Takawira, "The Influence of Spatial and Temporal Correlation on the Capacity of MIMO Channels," in *IEEE conference, Wireless Communications and Networking*, New Orleans, LA, 2003, pp. 359-364.

[23] A. Abdi and M. Kaveh, "A Versatile Spatio-Temporal Correlation Function for Mobile Fading Channels with Non-Isotropic Scattering," in *IEEE Workshop Statistical Signal Array Processing*, Pocono Manor, 2000, pp. 58-62.

[24] A. A. M. Saleh and R. A. Valenzuela, "A Statistical Model for Indoor Multipath Propagation," *IEEE Journal on Selected Areas in Communications*, vol. 5, no. 2, pp. 128-137, Feb. 1987.

[25] Q. Spencer, B. Jeffers, M. Jensen and A. Swindlehurst, "Modeling the Statistical Time and angle of aarival characteristiccs of an indoor multipath channel," *IEEE Journal on Selected Areas in Communications*, vol. 18, no. 3, pp. 347-360, Mar. 2000.

[26] J. W. Wallace and M. A. Jensen, "Statistical Characteristics of Measured MIMO Wireless Channel Data and Comparison to Conventional Models," in *IEEE 54th Vehicular Technology*, 2001, pp. 1078-1082.

[27] 3GPP TR 25.996, "Spatial Channel Model for Multiple Input Multiple Output (MIMO) simulations (Rel. 6)," 2003.

[28] A. F. Molisch, H. Asplund, R. Heddergott, M. Steinbauer and T. Zwick, "The COST 259 Directional Channel Model-I: Overview and Methodology," *IEEE Transactions on Wireless Communications*, vol. 5, no. 12, pp. 3421-3433, Dec. 2006.

[29] T. Zwick, C. Fischer and W. Wiesbeck, "A Stochastic Multipath Channel Model Including Path Directions for Indoor Environments," *IEEE Journal on Selected Areas in Communications*, vol. 20, no. 6, pp. 1178-1192, Aug. 2002.

[30] F. R. Farrokhi, A. Lozano, G. Foschini and R. Valenzuela, "Spectral Efficiency of Wireless Systems with Multiple Transmit and Receive Antennas," in *Sep.*, London, 2000, pp. 373-377.

[31] M. Ozcelik, N. Czink and E. Bonek, "What Makes a Good MIMO Channel Model?," in *IEEE 61st Vehicular Technology Conference*, Dec. 2005, pp. 156-160.

[32] N. Costa and S. Haykin, "A Novel Wideband MIMO Channel Model and Experimental Validation," *IEEE Transactions on Antennas and propagation*, vol. 56, no. 2, pp. 550-

562, Feb. 2008.

[33] A. G. Burr, "Capacity Bounds and Estimates for the Finite-Scatters MIMO Wireless Channel," *IEEE Journal on Selected Areas in Communications*, vol. 21, no. 5, pp. 812-818, June 2003.

[34] M. Debbah and R. R. Muller, "MIMO Channel Modeling and the Principle of Maximum Entropy," *IEEE Transactions on Information Theory*, vol. 51, no. 5, pp. 1667-1690, May 2005.

[35] A. M. Sayeed, "Deconstructing Multiantenna Fading Channels ," *IEEE Transactions on Signal Processing*, vol. 50, no. 10, pp. 2563-2579, Oct. 2002.

[36] D. Gesbert, H. Bolcskei, D. Gore and A. Paulraj, "MIMO Wireless Channels: Capacity and Performance Prediction," in *IEEE Global Telecommunications Conference*, Nov. 2000, pp. 1083-1088.

[37] L. Schumacher, J. P. Kermoal, F. Frederiksen, K. I. Pedersen, A. Algans, P. E. Mogensen, "MIMO Channel Charaterization," D2, version 1.1, IST-1999-11729 METRA, Feb. 2001.

[38] J. P. Kermoal, L. Schumacher and P. Mogenson, "Channel Characterization," IST Project IST-2000-30148 I-METRA, Deliverable 2, Oct. 2002.

[39] I. D. Sirkova, "Overview of COST 273 Part I: Propagation Modeling and Channel Characterization," in *XLI International Scientific Conference on Information, Communications and Energy Systems and Technologies (ICEST)*, Sofia, Bulgaria, 2006, pp. 29-32.

[40] V. Erceg, K. V. Hari, M. S. Smith and et al., "Channel Models for Fixed Wireless Applications," IEEE 802.16 Broadband Wireless Access Working Group, Jan. 2001.

[41] A. W. Umrani, Y. L. Guan and F. A. Umrani, "Transmit Diversity versus Beamforminng System in Correlated Faading Channel," *International Journal of Communication, Network and System Sciences*, vol. 3, no. 8, pp. 668-673, Aug. 2010.

[42] L. Schumacher, K. I. Pedersen, P. E. Mogensen, "From Antenna Spacing to Theoretical Capacities-Guidelines for Simulating MIMO Systems," in *13th IEEE International Symposium on Personal, Indoor and Mobile Radio Communications*, Portugal, 2002, pp. 587-592.

[43] J. Salz and J. H. Winters, "Effect of Fading Correlation on the Adaptive Arrays in Digital Mobile Radio," *IEEE Transactions on Vehicular Technologies*, vol. 43, no. 4, pp. 1049-1057, Nov. 1994.

[44] J. Tsai and B. D. Woerner, "The Fading Correlation of a Circular Antenna Array in Mobile Radio Environment," in *IEEE Global Telecommunications Conferencce*, San Antonio, United State of America, Nov. 2001, pp. 3232-3236.

[45] S. Yan and Z. Yerong, "Maximum MIMO Capacity of Rice Channel," in *IEEE International Conference on Wireless Communications & Signal Processing*, Nanjinj, China, Nov. 2009, pp. 1-5.

[46] J. P. Kermol, L. Schmacher, P. E. Mogensen and K. I. Pederson, "Experimental Investigation of correlation properties of MIMO Radio Channels for Indoor Picocell Scenarios," in *IEEE Vehicular Technology Conference*, Boston, United state of America, Sep. 2000, pp. 14-21.

[47] J. Tsai, R. M. Buehrer and B. D. Woerner, "Spatial Fading Correlation Function of Circular Antenna Arrays with Laplacian Energy Distribution," *IEEE Communications Letters*, vol. 6, no. 5, pp. 178-180, May 2002.

[48] Xin Liu and Z. P. Nie, "Spatial Fading Correlation Antenna Arrays with Laplacian PAS in MIMO Channels," in *IEEE Internation Symposium on Antennas and Propagation*, Sep. 2004, pp. 3697-3700.

[49] A. Forenza, D. J. Love and R. W. Heath, "Simplified Spatial Correlation Models for Clustered MIMO Channels," *IEEE Transactions on Vehicular Technology*, vol. 56, no. 4, pp. 1924-1934, July 2007.

[50] V. Dantona, R. T. Schwarz, A. Knopp and B. Lankl , "Uniform Circular Arrays: The Key to Optimum Channel Capacity in Mobile MIMO Satellite Links," in *5th IEEE Advanced Satellite Multimedia Systems Conference*, Sep. 2010, pp. 421-428.

[51] M. A. Mangoud, "Capacity Investigations of MIMO Systems in Correlated Rician Fading Channel Using Statistical Multi-Clustered Modeling," in *IEEE Conference, ITS Telecommunications*, Phuket, 2008, pp. 352-356.

[52] Xin Liu and M. E. Bialkowski, "Effective Degree of Freedom and Channel Capacity of a MIMO System Employing Circular and Linear Array antennas," in *IEEE International Conference on Wireless Communications, Networking and Mobile Computing*, Sep. 2009, pp. 1-4.

[53] A. Forenza and R. W. Jr. Heath, "Impact of Antenna Geometry on MIMO Communication in Indoor Clustered Channels," in *IEEE International Symposium om Antennas and Propagation*, June 2004, pp. 1700-1703.

[54] L. Dong, J. Ma, J. Zhou and H. Kikuchi, "Performance of MIMO with UCA and Laplacian Angular distribution Using Correlation Matrix," in *IEEE International Conference on Wireless Communications,Networking and Mobile Computing*, Sep. 2007, pp. 53-56.

[55] T. K. Paul and T. Ogunfunmi, "Wireless LAN Comes of Age: Understanding the IEEE 802.11n Amendment," *IEEE Circuits and Systems Magazine*, vol. 8, no. 1, pp. 28-54, First Quarter 2008.

[56] L. Schumacher and B. Dijkstra, "Description of a MATLAB implementation of the Indoor MIMO WLAN Channel Model Proposed by IEEE 802.11 TGn Channel Model Special Committee," Implementation note version May 2004.

[57] P. W. Wolniansky, G. J. Foschini, G. D. Golden and R. V. Valenzuela, "V-BLAST: an Architecture for Realizing Very High Data Rates Over the Rich-Scattering Wireless Channel ," in *URSI International Symposium on Signals, Systems and Electronics*, Pisa, Italy, Sep. 1998, pp. 295-300.

[58] A. J. Paulraj, D. A. Gore, R. U. Nabar and H. Bolcskei, "An Overview of MIMO Communications - a Key Gigabit Wireless," *Proceedings of the IEEE*, vol. 92, no. 2, pp. 198-218, Feb. 2004.

[59] G. D. Golden, G. J. Foschini, R. A. Valenzuela and P. W. Wolniansky, "Detection Algorithm and Initial Laboratory Results Using V-BLAST Space-Time Communication Architecture," *IEEE Electtronic Letters*, vol. 35, no. 1, pp. 14-16, Jan. 1999.

[60] G. J. Foschini, G. D. Golden, R. A. Valenzuela and P. W. Wolniansky, "Simplified Processing for High Spectral Efficiency Wireless Communication Employing Multi-Antenna Arrays," *IEEE Journal on Selected Areas in Communications*, vol. 17, no. 11, pp. 1841-1852, Nov. 1999.

[61] W. H. Chin, A. G. Constantinides and D. B. Ward, "Parallel Multistage Detection for Multiple Antenna Wireless Systtems," *IEEE Electronics Letters*, vol. 38, no. 12, pp. 597-599, Jun. 2002.

[62] Z. Wang, "Iterative Detection and Decoding with PIC Algorithm for MIMO-OFDM Systems," *International Journal on Communications, Network and Systems Sciences*, vol. 2, no. 5, pp. 351-356, Aug. 2009.

[63] L. Tong, B. M. Salder and M. Dong, "Pilot-Assisted Wireless Transmissions: General Model, Design Criteria and Signal Processing," *IEEE Signal Processing Magazine*, vol. 21, no. 6, pp. 12-25, Nov. 2004.

[64] C. Fragouli, N. A-Dhahir and W. Turin, "Training-Based Channel Estimation for Multiple-Antenna Broadband Transmission," *IEEE Transactions on Wireless Communications*, vol. 2, no. 2, pp. 384-391, March 2003.

[65] S. Zhou and G. B. Giannakis, "Finite Alphabet Based Channel Estimation for OFDM and Related Multicarrier Systems," *IEEE Transactions on Communications*, vol. 49, no. 8, pp. 1402-1414, Aug. 2001.

[66] H. Bolcskei, R. W. Heath, Jr. and A. J. Paulraj, "Blind Channel Identification and Equalization in OFDM-Based Multi-Antenna Systtems," *IEEE Transactions on Signal Processing*, vol. 50, no. 1, pp. 96-109, Jan. 2002.

[67] M. Biguesh and A. B. Gershman, "MIMO Channel Estimation: Optimal Training and Tradeoffs Between Estimation Techniques," in *IEEE International Conference on Communications*, Paris, France, Jun. 2004, pp. 2658-2662.

[68] J. H. Kotecha and A. M. Sayeed, "Transmit Signal Design for Optimal Estimation of Correlated MIMO Channels," *IEEE Transactions on Signal Processing*, vol. 52, no. 2, pp. 546-557, Feb. 2004.

[69] Xia Liu, M. E. Bialkowski and Shiyangn Lu, "Investigations into Training-Based MIMO Channel Estimation for Spatial Correlated Channels," in *IEEE Internationa Symposium on Antennas and Propagation Society*, Hawaii, USA, Jun. 2007, pp. 205-208.

[70] M. Kiessling, J. Speidel and Y Chen, "MIMO Channel Estimation in Correlated Fading Environments," in *IEEE Vechicular Technology Conference*, Orlando, USA, Oct. 2003, pp. 1187-1191.

[71] Xia Liu, M. E. Bialkowski, Shiyangn Lu and Hon Tat Hui, "MMSE Channel Estimator for MIMO System with Receiver Equipped with a Circular Array Antenna," in *Asia-Pacific Microwave Conference (APMC)*, Thailand, Dec. 2007, pp. 1-4.

ملخص الرسالة

أداء أنظمة الاتصالات متعددة المدخلات والمخرجات الزمنية و المكانية التي تستخدم مصفوفة الهوائيات الدائرية باستخدام نماذج واقعية لقناة الاتصال

تم مؤخراً وعلى نطاق واسع استخدام تقنية تعدد المداخل وتعدد المخارج (MIMO) لتحسين نوعية إشارة البث والتغطية وسعة القناة في أنظمة الاتصالات اللاسلكية الحديثة. إن أداء هذه الأنظمة التي توظف مجموعة من هوائيات المرسلات ومجموعة من هوائيات المستقبلات تعتمد على خصائص الروابط لقنوات البث الإذاعية و التي بدورها تعتمد على ترتيب الهوائيات، انتشار ظاهرة دوبلر،و توزيع الأجسام المتناثرة بين المرسل والمستقبل. لذلك فإن الغرض من هذه الدراسة هو تطوير وتحليل نموذج لقناة حقيقية واقعية تتضمن خصائص الارتباط. لذلك سوف يتم دراسة قدرة وأداء النظام اللاسلكي لشبكة المنطقة المحلية (LAN) في وجود القناة الواقعية. ومن الأهداف أيضا دراسة أداء الواي فاي (Wi-Fi) الحديث المقترح من قبل IEEE 802.11*n* كقياس ناشئ لتطبيق هذه التقنية.

تبدأ الرسالة بمسح شامل لأنظمة القنوات المختلفة الموجودة حالياً والتي تقدم تصنيفاً فيزيائياً، تحليلياً ونموذجاً قياسياً. تعطي هذه الدراسة مقارنة تلقى الضوء على الفروق النظرية والنواقص الموجودة في كل منها. كما توفر الدراسة أيضا نموذجاً إحصائياً مكانياً عنقودياً (SSC) ويتبع ذلك نموذجاً أكثر واقعية وهو العنقودي الزمكاني (الزماني المكاني) (STC). وهذا النموذج الأخير يتعامل مع المسارات المنعكسة كإشعاعات عنقودية. ويحتوي كل عنقود على طاقة ذات تأخير مختلف متعلق بارتدادات ذات معاملات مختلفة في أوقات مستقطعة. هذا النموذج يأخذ في الحسبان ستة سيناريوهات حقيقية ومختلفة لانتشار الموجات التي تمثل مجموعة متنوعة من البيئات المغلقة.

لقد تم تطوير نموذج القناة العنقودي الزمكاني لتعديل النموذج القياسي الموجود حالياً IEEE 802.11*n* باعتماد مصفوفة التوزيع الدائري (UCA) للأنظمة متعددة المداخل والمخارج. تأثير اختيار نموذج القناة على أداء الأنظمة تم التحقق منه باستخدام مصفوفة التوزيع الخطي (ULA) ومصفوفة التوزيع الدائري كما تم دراسة تأثير تغيير فراغات عناصر المصفوفة و هندستها وتوجيهها من كلا الجانبين.تم تقدير سعة القناة نظرياً وروابط القنوات عندما تكون معلومات حالة القناة (CS1) متوافرة لدى جهاز الإرسال. كذلك تم دراسة تحقق تأثير مستوى النظر (LOS) من عدمه.

أيضا تم دراسة أداء نظام مختبرات بيل الأفقية الزمكانية (V-BLAST) للتحقق من كيفية استرداده للإشارة المرسلة بما في ذلك تأثير خصائص الارتباط عليه. وتم ذلك بتوظيف نظام القناة الإحصائي المكاني العنقودي لكل من مصفوفة التوزيع الخطي ومصفوفة التوزيع الدائري الهندسية عند المستقبل. طبقت مجموعة من مختلف تقنيات الاستقبال والتي تحتوي على صفر الإجبار الخطي (ZF)، الخطأ المربعي ذو متوسط الحد الأدنى الخطي (MMSE)، إلغاء التداخل المتتابع (SIC)، إلغاء التداخل المتوازي (PIC)، و احتمال الحد الأدنى (ML). كما تم التحقق من تأثير الارتباط المكاني على أداء النظام المختلف النسب بين الإشارة والضوضاء (SNR). وكذلك زاوية الوصول (AOA) والانتشار الزاوي (AS) والمسافات البينية لمختلف عناصر المصفوفة.بالإضافة إلى ذلك فإن النتائج الرقمية قارنت بين مختبرات بيل الأفقية الزمكانية للاستقبال بهوائيات مصفوفة التوزيع الخطي وتلك التي تستخدم مصفوفة التوزيع الدائري الخطي. و من الجدير بالذكر أن تأثير حالات القناة على أداء الاستقبال تم تقيمه أيضاً باستخدام القناة الواقعية الزمكانية (STC).

معلومات حالة القناة يجب أن تكون متوافرة بدقة لدى جهاز الاستقبال ليكتمل تحليل أداء الأنظمة متعددة المداخل والمخارج. تمت دراسة عدد من أساليب التدريب القائمة بما في ذلك: المربعات الأقل (LS)، المربعات الأقل المدرجة (SLS)، الخطأ المربعي ذو متوسط الحد الأدنى الخطي (LMMSE)، والخطأ المربعي ذو متوسط الحد الأدنى المنبسط (RMMSE). تم اشتقاق التدريب الأمثل لهذه الطرق و استخدامها في المحاكاة العددية. في هذه الدراسة الطرق المختلفة لتقدير القنوات يمكن تطبيقها في محاكاة الأنظمة متعددة المداخل والمخارج والتي تأخذ نموذج القناة الإحصائي المكاني العنقودي. تأثير الرابط المكاني للقناة على الخطأ التقديري للقناة تم تقييمه في هوائيات مصفوفة التوزيع الخطي ومصفوفة التوزيع الدائري.كما تم التأكيد بأن حضور الرابط المكاني يساعد في خفض الخطأ التقديري للقناة عندما تكون النسبة بين الإشارة والضوضاء صغيرة . أداء مقيم القناة هو الأخر تمت دراسته عند التطبيق الأمثل للتسلسلات التدريبية و التسلسلات المتعامدة. تم أيضا مقارنة الأخطاء المقدرة للقناة وسعتها في حالة مصفوفة التوزيع الدائري و الخطي تحت عدة قيم لزاوية الوصول والانتشار الزاوي.